ACTIVE CONTROL OF CENTRIFUGAL COMPRESSOR SURGE

by

Judith Ellen Pinsley

B.S., Cornell University (1986)

SUBMITTED IN PARTIAL FULFILLMENT
OF THE REQUIREMENTS FOR THE
DEGREE OF

MASTER OF SCIENCE IN
AERONAUTICS AND ASTRONAUTICS

at the

MASSACHUSETTS INSTITUTE OF TECHNOLOGY

October 28, 1988

Signature of Author _____
utics and Astronautics
October 28, 1988

Certified by ___
Prof. Edward M. Greitzer
Thesis Supervisor

Accepted by ___
rof. H.Y. Wachman
Graduate Committee

ACTIVE CONTROL OF CENTRIFUGAL COMPRESSOR SURGE

by

Judith Ellen Pinsley

Submitted to the Department of Aeronautics and Astronautics on October 28, 1988 in partial fulfillment of the requirements for the Degree of Master of Science in Aeronautics and Astronautics.

ABSTRACT

A new method for actively suppressing compressor surge in a centrifugal compressor has been investigated through experiments supported by theory. The controller is a real-time feedback of the plenum pressure rise perturbations to a servo-actuated plenum exit throttle. Small perturbations of this control valve provide increased damping of incipient oscillations and this allows the compressor to operate stably past the normal surge line.

The controller used was based on a simple proportional control law. The theory predicts that the effectiveness of this controller is a strong function of the stability parameter $B = (U/2a)\sqrt{V_p/(L_c A_{in})}$, with lower values of B leading to a higher degree of stability. The theory also determined the proportionality constant (gain) of the controller. For maximum increase in stable flow range, a controller phase of zero degrees was found to hold for all operating conditions with the gain set within limits determined by the system parameters. The model predicts, and the experiments confirm, that with control the compression system resonant frequency and perturbation growth rate are changed.

Based upon the success of preliminary low speed tests, a high speed facility was constructed for operating a small turbocharger at realistic pressure ratios. The experimental results showed that active throttle control is a viable means to suppress surge and operate within a previous inaccessible region. A reduction of 25% in the surge point mass flow was achieved over a range of operating conditions. Surge line extension was found to be strongly B dependent. Time-resolved measurements showed that suppression of surge oscillations was achieved with relatively little power input to the control valve. The throttle controller was also able to eliminate existing large amplitude surge oscillations even though the surge phenomenon is nonlinear. Comparison of experimental measurements with theoretical predictions showed that the simple model used gives adequate representation of the behavior of the compression system with a throttle controller.

Thesis Supervisor: Dr. Edward M. Greitzer

Title: Professor of Aeronautics and Astronautics

ACKNOWLEDGEMENTS

There are numerous people whom I wish to thank for their contribution to this project:

Professor Edward M. Greitzer for guidance, encouragement, and confidence in this "Smart Engines" concept.

Professor Alan H. Epstein for his practical advice on all matters of the experimental investigation.

Dr. Gerald Guenette for the long hours that he devoted to the intricacies of instrumentation and the fine points of the analysis. Thanks also for sharing the secrets of vacationing in Maine.

Holly Rathbun for her talent in handling the finances and enduring my continual questions.

Robert Haimes and David Dvore for taming the MicroVax "beast", while providing many entertaining moments along the way.

Viktor Dubrowski for his expert craftsmanship in the machine shop and his political observations.

Jim Nash and Roy Andrew for patiently teaching me all manner of laboratory procedures and helping construct the test rig.

Karen Hemmick, Nancy Martin, and Diana Park for their help on all the details.

Maj. John Craig Seymour, who preceded me to the degree list, for his keen sense of humor and for refraining from excessive conversation during the morning newspaper ritual. Also thanks to his wife Sherri and daughter Stephanie for wonderful visits to their home.

Petros Kotidis for sharing inside information on everything from file backups to Campus House of Pizza.

Gwo-Tung Chen and David Fink for the extensive groundwork they provided in the analytical and experimental world, respectively.

George Haldeman for building the first test rig and the design of the control valve.

Jim Paduano and John Simon for their perspectives from the control world and for the motor controller.

My parents, Edward and Jane Pinsley, for their love and support throughout my life. Special thanks to my father for having an excitement about science which happily rubbed off on me.

Finally, enormous thanks to my husband-to-be, Mark Reich, for his inestimable contribution. Without his pep talks, well-placed criticism, and love this thesis would never have been possible.

The project was conducted under grants from the Army Aeropropulsion Laboratory and the Air Force Research in Aero Propulsion Technology (AFRAPT) program, and the author gratefully acknowledges this support. The author also acknowledges the support of Mr. Harold Weber from Cummins Engine Company.

TABLE OF CONTENTS

LIST OF FIGURES

Test Setup Schematic

4.19(b) Overall Control Loop Transfer Function Including Pressure Transducer, Measured Magnitude

4.19(c) Overall Control Loop Transfer Function Including Pressure Transducer, Measured Phase

4.20 Schematic of Data Acquisition Inputs and Outputs to the Controller

5.1(a) Measured Compressor Map in Small B Configuration, Pressure Ratio vs. SCFM

5.1(b) Measured Compressor Map in Small B Configuration, Psi vs. Phi

5.1(c) Measured Compressor Map in Small B Configuration, Head Coefficient vs. Phi

5.2 Surge Line Shift with Controller, Small B Configuration

5.3 Control Effect at 90,000 RPM on Nondimensional Pressure Rise vs. Mass Flow

5.4 Compressor Adiabatic Efficiency Under Control at 90,000 RPM

5.5 Measured Compressor Map in Large B Configuration Showing Control Range

5.6 Control Effect at the Same B Parameter, Different Speed

5.7(a) Nondimensional Compressor Characteristic at 90,000 RPM Showing Measured Points

5.7(b) Nondimensional Perturbations at 90,000 RPM

5.8 Uncontrolled Mild Surge Cycles

5.9 Uncontrolled Deep Surge Cycles

5.10(a) Nondimensional Compressor Characteristic at 90,000 RPM Showing Measured Control Points

5.10(b) Nondimensional Perturbations at 90,000 RPM Under Control

5.11 Power Spectral Density of Valve Motion Under Control at Point A'

5.12 Controlled Nondimensional Pressure Rise and Mass Flow Perturbations

5.13 Nondimensional Valve Area, Plenum Pressure, and Mass Flow Perturbations with Control in Deep Surge

5.14 Deep Surge Cycles with Control

5.15 RMS and Peak Amplitudes of Plenum Pressure Perturbations

NOMENCLATURE

Symbols

a -- speed of sound
-- coefficients of cubic compressor characteristic
-- coefficient of system characteristic equation

A -- cross-sectional area
-- system matrix

A_{exit} -- cross-sectional area of compressor exit duct

A_{in} -- annular impeller inlet area

A_{open} -- wide open control valve area

A_T -- throttle area

A_v -- control valve area

b -- coefficient of parabolic valve characteristic
-- coefficient of system characteristic equation

b' -- "total" discharge coefficient: pressure drop in psid/(flow rate in SCFM)^2

B -- stability parameter

c -- coefficient of system characteristic equation

c_d -- discharge coefficient

C -- slope of valve pressure drop vs. mean valve area

C_x -- axial velocity

f -- frequency

H -- Hodgson number

L -- characteristic length

L_c -- effective compressor duct length

m -- mass flow

M -- Mach number

N_{corr} -- corrected rotational speed

N_{mech}-- mechanical rotational speed

P -- pressure

R -- radius
-- gas constant

Re_x -- flat plate Reynolds number based on distance from leading edge

s -- roots of system characteristic equation

t -- time

T -- slope of pressure rise (or drop) vs. mean mass flow
-- temperature

U -- rotor tip speed

V_c -- compressor volume: $A_{in}L_c$

V_p -- plenum volume

x -- distance from leading edge in flat plate theory

z_A -- complex constant for throttle control

z_ξ -- complex constant for volume control

α -- ratio of valve area to wide open valve area

β -- perturbation growth rate

γ -- specific heat ratio

δ_d -- boundary layer displacement thickness from flat plate theory

η -- adiabatic compressor efficiency

ξ -- nondimensional plenum volume

π -- compressor total-to-static pressure ratio

ρ -- density

τ -- total temperature ratio

ϕ -- nondimensional mass flow

ψ -- nondimensional pressure rise

ψ_h -- isentropic head rise coefficient

ω -- Helmholtz frequency

ω_f -- forcing frequency

ω_n -- natural frequency

Subscripts

c -- compressor

ref -- reference conditions, sea-level static

t -- total

v -- control valve

0 -- ambient
-- control at zero gain

1 -- plenum

2 -- exit

Operators

$\delta( )$ -- perturbation quantity

$\Delta( )$ -- differential

$\frac{d( )}{dt}$ -- derivative

$\frac{\partial( )}{dt}$ -- partial derivative

(^) -- nondimensional quantity

(~) -- reduced quantity

CHAPTER 1

Introduction and Background

1.1 Introduction

Surge in a compression system is a self-excited instability involving an interaction between the compressor and its associated ducting. It can be characterized by large amplitude oscillations of annulus averaged mass flow and plenum pressure rise. For the type of centrifugal compressors under study these essentially one-dimensional surge cycles may take one of two forms.[1] In mild surge the mass flow and plenum pressure fluctuate near the system Helmholtz frequency but the mass flow never reverses. In deep surge the annulus averaged mass flow does reverse and the frequency is lower. The frequency in this mode is associated with the repeated blowdown and repressurization of the plenum. The stresses created by these violent oscillations can cause structural damage to a gas turbine engine [11], as well as severely degrade performance, so the compressor is generally operated in a manner to avoid surge.

In the past, avoiding surge has meant defining a margin of safety between the so-called surge line and the closest allowable operating point. For centrifugal compressors, however, the maximum efficiency can occur near the peak of the pressure rise vs. mass flow characteristic near the surge line. In addition, the

[1] Both forms of surge should be distinguished from rotating stall, a local instability in which disturbances propagate around the circumference of the compressor while the annulus averaged mass flow remains constant.

stable range of a compressor performance map must be sufficiently large that surge is not encountered during engine operation over expected throttle positions and wheel speed ranges. The active control techniques described in this thesis can extend this range of stable operation above the natural surge line (Figure (1.1)). The new "controlled" surge line could thus open up the usable operating region, allowing greater freedom in compressor operation and design.

The essential components of the compression system consist of a compressor which supplies energy to the system, a plenum which acts as a capacitance, and a throttle which dissipates energy. In the most basic model the compressor is treated as an actuator disk, with the kinetic energy of the system considered to occur in the compressor and throttle ducts and all the potential energy contained in the "springiness" of the fluid in the plenum. This mass-spring-damper analogy of the system is shown in Figure (1.2). While it does not consider the detailed fluid mechanics within the compressor that lead to surge, this lumped parameter model does show the global features of the surge cycle behavior [7,19].

By linearizing the equations of this model for small perturbations around a mean operating point, one can determine the stability of the system [14]. Many such analyses have been carried out, including [1,4,5,7,19,20], and one central conclusion is that while either static or dynamic criteria may be violated to drive the system to instability, it is usually the dynamic criterion which is the more critical. Violation of the dynamic criterion corresponds to negative damping. In terms of the compressor pressure rise vs. mass flow characteristic, this condition can only occur when the characteristic is positively sloped (Figure (1.3)). In such a situation, if the system experiences a small perturbation, the compressor can supply more energy than the throttle dissipates so that these perturbations

grow. The balance between the energy supplied and dissipated is set by the system dynamic behavior. Growth of the perturbations is terminated by nonlinearities, producing a surge limit cycle (Figure (1.4)).

The dynamic behavior of the system depends on geometrical parameters as well as fluid properties. A non-dimensional stability parameter has been defined in reference [7] as:

$$B = \frac{U}{2\omega L_c} = \frac{\frac{\rho U^2}{2}}{\rho U \omega L_c} \tag{1.1}$$

where ω is the system Helmholtz frequency defined as:

$$\omega = a\sqrt{\frac{A_{in}}{V_p L_c}} \tag{1.2}$$

A_{in} is the impeller inlet area, L_c is the compressor duct length, V_p is the plenum volume, and a is the sonic speed in the plenum. As implied by Eq. (1.1), B can be viewed as a ratio of pressure forces acting on the fluid in the compressor duct to inertial forces in the duct. As B increases, the pressure difference across the compressor duct will have greater capability to drive the fluid and therefore greater ability to induce surge. Consequently systems with high B factors are less stable. Because transient behavior scales with this parameter, systems with the same B but different geometrical parameters, assuming the same compressor characteristic, should exhibit the same dynamic response.

Surge behavior of a given system at different B parameters can vary dramatically. In this context Emmons, et al. [4] found that the onset of surge in a centrifugal compressor was speed dependent. At low speed the compressor entered a period of mild surge. As throttling continued, the compressor resumed stable operation. Further throttling produced the flow reversal and plenum blowdown associated with deep surge. At increasing speeds the stable region separating the two surge regimes gradually diminished until finally the onset of mild surge immediately triggered deep surge. Although the change in surge behavior with speed might be attributed to either tip Mach number or B parameter variation, the experiments described below indicated that the surge characteristics are directly related to the B parameter [6]. The B parameter is thus, as will be seen, the dominant influence on system stability. In particular with reference to the objectives of this thesis, compressibility effects per se do not place a limit on the controllability of a given system.

1.2 Overall Approach to Surge Control

1.2.1 Previous Approaches to Surge Control

With the obvious impetus for increasing the operating range and maximizing the compressor efficiency, many efforts have been made to delay the onset of surge through modifications in the components thought to trigger instability. Configurations have included such modifications as impeller and vaned diffuser wall treatments [10], close coupled resistances [3], improved diffuser geometry [16,18], among many others. These have shown some extension of stable operating range, but extension is often accompanied by an undesirable reduction in compressor total pressure rise and adiabatic efficiency. Attempts have also been made to broaden the range of safe operation by narrowing the

surge margin while keeping the same surge line. Toyama, et al. [21] studied the time-resolved behavior of a centrifugal compression system operating close to surge and revealed that oscillations in mass flow exist even in this so-called stable region. If these perturbations grow past a certain threshold amplitude, even for a single oscillation, surge will be triggered [2].

Many open-loop control schemes have also been devised to detect imminent surge and to take corrective action to back off from that operating point. The actuator would be an external device, such as bleed ports or a throttle, with minimum complexity and computational requirements. However, large actuator forces are required, and by backing off from surge these control strategies trade performance for stability.

1.2.2 Active Surge Control

The control approach taken here is fundamentally different than previous surge suppression schemes. This control philosophy seeks to effect changes in the system dynamic behavior in applying the principles of feedback control to a compression system. The basic theoretical model was given by Epstein, et. al. [5]. They discussed a scheme for surge control in which either (or both) the plenum wall and the exit throttle would be driven in response to sensed perturbations in the plenum pressure (Figure (1.5)). The control laws were taken as:

$$\xi = z_{\xi}\, \delta\psi \tag{1.3}$$

$$\frac{\delta A_T}{A_T} = z_A \, \delta\psi \tag{1.4}$$

where ξ is the nondimensional wall position (proportional to plenum volume), A_T is the throttle valve area, and $d\psi$ is the nondimensional pressure perturbation. The complex constants z_ξ and z_A give the gain and phase of the plenum wall and throttle area perturbations, respectively, to the plenum pressure perturbations. Calculations carried out using this model predicted not only that significant shifts in the surge point could be effected but also that controller power requirements scaled with the square of the disturbance amplitude and were thus much less than steady state machine power [1].[2]

In a complementary effort to this work (also based on the treatment in [5]), active control, using Eq. (1.3) as the feedback loop has recently been demonstrated on a turbocharger similar to the one used in the present investigation [9]. A loudspeaker mounted as one wall of the plenum acted as the movable control element. Steady state pressures on either side of the loudspeaker were equalized in order to expose it only to pressure transients. With proportional feedback, the compression system was made to operate stably beyond the natural surge boundary (Figure (1.6)). Suppression of existing surge cycles was also found, and the controlled system operating in a normally stable region was determined to withstand larger pressure impulses without triggering surge.

1.3 Scope of Present Active Control Experiment

[2] Strictly speaking, the controller power is also a function of the B parameter, which in turn depends on the compressor's operating point.

The goal of the present experiment was to demonstrate active surge suppression of a centrifugal compressor using throttle control at realistic pressure ratios. For simplicity the control law was taken to be simple proportional feedback as in Eq. (1.4). Initial calculations by Chen [1] predicted substantial surge suppression with this type of controller. Parametric studies were carried out using a lumped-parameter system model, and the results served both to guide the experimental investigations and to interpret the results. Two modes of active throttle control were considered in the model:

1) Control valve located at the plenum exit
2) Control valve close-coupled to the compressor exit

In case 1, which will be referred to as the plenum exit mode, the throttle would dissipate the entire compressor pressure rise through the mean valve area.[3] Small perturbations about this equilibrium position would provide the control action. The plenum pressure would then equal the compressor output. This is the situation that will be described in detail in this thesis.

Case 2, called the compressor exit mode, inserts the control valve between the compressor exit and the plenum. A fixed valve at the plenum exit dissipates the mean energy input from the compressor/control valve combination. For the control valve area to fluctuate about a mean, a certain pressure drop across the controller would have to be tolerated. This loss in usable pressure rise is offset by the possibility for greater stabilization since the controller would more directly

[3] Here, the "throttle" may actually be a combination of the control valve in series with a standard valve whose area is fixed. See Section 2.2 for a more thorough discussion of the plenum exit mode throttling.

influence the inertance of the system. Adaptation of this type of throttle control to an aircraft engine would require placing the control element in the compressor's diffuser.

Using the lumped-parameter model, analytical studies were carried out to predict the expected shift in the surge point with various control inputs at any desired operating point. The results for the compressor exit mode, although encouraging, suggested that further analysis would have to be carried out to fully exploit this configuration and thus was beyond the scope of the present effort. For the plenum exit mode, however, the controller effect could be readily quantified by the theory; thus the experiments and analysis reported herein are based on the use of plenum exit control. Low speed tests were first performed on a small turbocharger as a proof-of-concept. Success of the control scheme with this apparatus led to the construction and use of a high speed test facility. Both steady-state and time-resolved data were taken to characterize system performance under control. The control scheme was tested over a range of B parameters to assess the dependence of control effectiveness on B and to distinguish B effects from tip Mach number effects.

The following questions were examined during the course of the experiments:

- Does this type of active throttle control successfully suppress system surge oscillations?
- What will the system performance be in a controlled region of operation?
- Will the controller adversely affect operation in normally stable regions?

- Does the linear model accurately represent the system and the controller?
- Is the B parameter the dominant influence on system controllability?
- Can the results obtained in this experiment be generalized for other similar systems?

CHAPTER 2

Active Throttle Control Modelling

2.1 Introduction

The schematic illustration given in Figure (2.1) shows the pumping system with the throttle controller in the plenum exit configuration. The dynamics of the system may be characterized using a lumped parameter representation to produce a set of coupled system equations linking unsteady mass flow and pressure rise. Linearization about a mean operating point produces the system matrix which characterizes the overall stability. The following assumptions are made in deriving the system equations:

1) Quasi-steady compressor behavior
2) Uniform pressure throughout the plenum
3) Isentropic fluid behavior in the plenum
4) Incompressible flow in the ducts
5) Negligible inertance in the throttle
6) Quasi-steady flow through the throttle
7) Constant ambient conditions at the inlet and exit of the system

Steps leading to the system equations are well known. For reference they are outlined in Section 2.2 and given in more detail in Appendix A. The compressor mass flow and the plenum pressure rise are the two state variables. This characteristic equation for the system is second order, as the simple

proportional control law contained no added dynamics which would create a higher order system.

This second order model was used to perform parametric studies of the controlled compression system. Control was evaluated over various operating points from the following information: the steady-state mass flow and pressure rise, the compressor and throttle characteristic slopes, the mean control valve area, the B parameter, and the controller complex gain. Stability under control was first investigated using root locus plots for a constant phase of the complex controller gain. Preliminary requirements for control effort for surge suppression were determined this way as a function of the steady-state operating point and the value of B. Next the stable operating region in the controller gain-phase plane was delineated for a given operating point, and the dependence of this region on B and compressor slope were examined. Since the compressor slope was found to influence stability, an investigation was carried out to quantify this effect as a function of the controller gain and system B parameter at a set operating point. Finally, the system behavior was examined over a range of control gain and phase to predict the effect of the controller in both stable and unstable operating regimes.

2.2 Model of the Compression System

The following equations show how the conservation equations applied to the lumped-parameter model result in a second order characteristic equation for the system. A more detailed derivation is given in Appendix A. Referring to Figure (2.1), conservation of momentum in the compressor duct gives:

$$P_0 - P_1 = \frac{L_c}{A_{in}} \frac{d\dot{m}_1}{dt} - \Delta P_{t,c} \tag{2.1}$$

where L_c is the effective length of the compressor duct, including blade passages and volute, and A_{in} in the annular impeller inlet area. $\Delta P_{t,c}$ is the total pressure rise across the compressor. Similarly, conservation of momentum in the exit duct, assuming negligible throttle inertance, leads to:

$$P_1 - P_0 = \Delta P_{t,v} \tag{2.2}$$

where $\Delta P_{t,v}$ is the total pressure drop across the control valve. It is assumed that $P_2 = P_0$. Mass conservation in the plenum, utilizing the isentropic relation, requires that:

$$\dot{m}_2 = \dot{m}_1 - \frac{V_p}{a_1^2} \frac{dP_1}{dt} \tag{2.3}$$

V_p is the plenum volume and a_1 is the speed of sound in the plenum. Eqs. (2.1) to (2.3) are linearized about a mean operating point and combined to give:

$$\frac{L_c}{A_{in}} \frac{d\delta\dot{m}_1}{dt} = T_c \delta\dot{m}_1 - \delta P_1 \tag{2.4}$$

$$\frac{V_p}{a_1^2} \frac{d\delta P_1}{dt} = \delta\dot{m}_1 - \frac{1}{T_v} \delta P_1 + C_v \delta A_v \tag{2.5}$$

with δ representing perturbation quantities and A_v representing the control valve area. All slopes are calculated at the mean operating conditions:

T_C = slope of compressor pressure rise vs. mass flow characteristic

T_V = slope of control valve pressure drop vs. mass flow characteristic

C_V = slope of control valve pressure drop vs. mean valve area characteristic

A_V = mean valve area

Each term in Eqs. (2.4) and (2.5) is then nondimensionalized by geometrical dimensions and flow properties. The two state variables, pressure rise and mass flow, become:

$$\psi = \frac{\Delta P}{\frac{1}{2}\rho_0 U^2} \quad \text{-- pressure rise} \tag{2.6}$$

$$\phi = \frac{\dot{m}}{\rho_0 U A_{in}} \quad \text{-- mass flow} \tag{2.7}$$

where ρ_0 is the ambient density and U is the impeller tip speed. The time scale in the derivative terms becomes:

$$\hat{t} = \omega t \quad \text{-- time} \tag{2.8}$$

Thus time is normalized by the system Helmholtz frequency. In addition to these variables, the nondimensional system parameters are:

$$\hat{T}_c = T_c\left(\frac{2A_{in}}{U}\right) = \frac{d\psi_c}{d\phi} \tag{2.9}$$

$$\hat{T}_v = T_v\left(\frac{2A_{in}}{U}\right) = \frac{\partial\psi_v}{\partial\phi}_{A_v=\text{constant}} \tag{2.10}$$

$$\hat{C}_v = C_v\left(\frac{2A_{in}}{\rho_0 U^2}\right) = \frac{\partial\psi_v}{\partial\hat{A}_v}_{\phi=\text{constant}} \tag{2.11}$$

$$\hat{A}_v = \frac{A_v}{A_{in}} \tag{2.12}$$

With the definition of the B parameter:

$$B = \frac{U}{2a}\sqrt{\frac{V_p}{L_c A_{in}}} = \frac{U}{2\omega L_c} \tag{2.13}$$

Eqs. (2.4) and (2.5) can be written in nondimensional form as:

$$\frac{d\delta\phi}{d\hat{t}} = \frac{\hat{T}_c B}{2}\delta\phi - \frac{B}{2}\delta\psi \tag{2.14}$$

$$\frac{d\delta\psi}{d\hat{t}} = \frac{1}{2B}\delta\phi - \frac{1}{2B\hat{T}_v}\delta\psi + \frac{\hat{C}_v}{2B\hat{T}_v}\delta\hat{A}_v \tag{2.15}$$

The system described by Eqs. (2.14) and (2.15) is still open loop. Thus a control law for the valve area perturbations must be included. In this case, the control law is taken as proportional:

$$\frac{\delta\hat{A}_v}{\hat{A}_v} = z_A\,\delta\psi \tag{2.16}$$

The constant z_A is complex, and described the gain and phase relations between the pressure perturbations and the valve motion. Inserting this control law into Eq. (2.15), the closed loop equations are thus:

$$\frac{d\delta\phi}{d\hat{t}} = \frac{\hat{T}_c B}{2}\delta\phi - \frac{B}{2}\delta\psi \tag{2.17}$$

$$\frac{d\delta\psi}{d\hat{t}} = \frac{1}{2B}\delta\phi - \frac{1}{2B}\left[\frac{1 - \hat{C}_v \hat{A}_v z_A}{\hat{T}_v}\right]\delta\psi \tag{2.18}$$

In matrix form Eqs. (2.17) and (2.18) become:

$$\begin{bmatrix} \delta\dot{\psi} \\ \delta\dot{\phi} \end{bmatrix} = [A]\begin{bmatrix} \delta\psi \\ \delta\phi \end{bmatrix} \tag{2.19}$$

where A is the system matrix. Setting the determinant of [A-sI] equal to zero, where s is the complex system frequency, produces the characteristic equation for the two system poles:

$$s^2 - \left[\frac{\hat{T}_c B}{2} - \frac{1}{2B}\left(\frac{1 - \hat{C}_v \hat{A}_v z_A}{\hat{T}_v}\right)\right]s - \frac{\hat{T}_c}{4}\left(\frac{1 - \hat{C}_v \hat{A}_v z_A}{\hat{T}_v}\right) + 1 = 0 \tag{2.20}$$

Each of the nondimensional slopes must now be calculated. In steady-state the pressure rise from the compressor must equal the pressure drop through the control valve, so that $\psi_C = \psi_V$. If the compressor characteristic is assumed to be a cubic in mass flow and the throttle valve is taken to be parabolic, then:

$$a_3\phi^3 + a_2\phi^2 + a_1\phi + a_0 = b(\hat{A}_v)\phi^2 \tag{2.21}$$

Thus the $\hat{T}_c$ is also readily calculated. The coefficients of the cubic were taken from Fink's experimental curve fit [6] and are assumed to be representative of a general class of centrifugal compressors:

$$a_3 = -13.5$$

$$a_2 = .98$$

$$a_1 = 1.59$$

$$a_0 = 1.38$$

Assuming that the control valve behavior is quasi-steady, the constant b is determined for any valve setting. The static pressure drop across the control valve, using the equation for incompressible flow through a sharp-edged orifice for simplicity, is:

$$\Delta P_v = \frac{\dot{m}^2\left[1 - \left(\frac{A_v}{A_{exit}}\right)^2\right]}{2\rho\, c_d^2 A_v^2} \tag{2.22}$$

Since near surge there is negligible difference between the static and total pressure upstream of the valve, the static pressure in the valve duct is thus taken equal to the plenum pressure. The discharge coefficient, c_d, is the ratio of the actual valve area to the throat area, and for calculations using the model it is assumed to be .6. In nondimensional terms:

$$\psi_v = \frac{1}{4}\left[\frac{1-\left(\frac{\hat{A}_v}{\hat{A}_{exit}}\right)^2}{c_d^2 \hat{A}_v^2}\right]\phi^2 = b(\hat{A}_v)\,\phi^2 \tag{2.23}$$

The slopes of the valve characteristics are then:

$$\hat{T}_v = 2\,b(\hat{A}_v)\,\phi \tag{2.24}$$

$$\hat{C}_v = \frac{-\phi^2}{2\,c_d^2 \hat{A}_v^3} \tag{2.25}$$

Selecting either the mass flow or the pressure rise for a steady-state operating point, Eqs. (2.21) to (2.25) can be used to calculate all slopes. The values of B and z_A then determine the stability of the system from Eq. (2.20).

2.3 System Stability Analysis

2.3.1 Positioning of System Poles

The poles obtained from Eq. (2.20) with $z_A = 0$ show the uncontrolled stability of the system at the selected mass flow. Uncontrolled poles located in the right half plane indicate an exponential growth rate of disturbances and thus instability. The use of the controller can shift both unstable poles to the left half plane, with the imaginary axis being the boundary of neutral stability.

To shift these poles the proper magnitude and phase of the controller must be selected. Chen [1] showed that the phase which produced the lowest stable mass flow was near zero degrees, independent of B. This result can be seen in Figure

(2.2), taken from [1]. Zero phase shift between the input and output signals implies that as the plenum pressure increases, the valve area opens so that the dissipation across the valve is increased. The required excursions of the valve area are set by the magnitude of z_A.

Figure (2.3) shows a typical root locus plot for the system as the magnitude of z_A is increased from 0 (no control) to maximum gain at zero phase. At mildly unstable flow rates, increasing the gain initially stabilizes the system. However, the presence of a positive zero eventually drives one of the poles back across to the right half plane on the real axis to destabilize the system. There is thus a distinct range of gains which may achieve stabilization. This range varies as a function of the B parameter and the equilibrium positioning of the two throttle valves. It is desirable to achieve control with a small value of z_A while maintaining a margin of safety before destabilization can occur.

As the desired stable mass flow is reduced, the stable range for the magnitude of z_A decreases and the magnitude of z_A required to reach neutral stability increases. Thus for this particular control law there is a minimum mass flow below which no amount of gain can produce stability. The reason for this will be discussed later. This minimum flow can be plotted as a function of the B parameter as in Figure (2.4).

2.3.2 Stability Boundary in the Gain-Phase Plane

Although zero degree phase difference between control input (pressure perturbations) and output (valve motion) is optimum for the greatest range of controllability, control may also be achieved to some degree at other phase

differences. The stable operating region in the gain-phase plane for ϕ = .12 is shown in Figure (2.5). The inner cross-hatched region, where both poles are located in the left half plane, is the area of stable operation. Outside this region the system is unstable. It can be seen that there exists a minimum and maximum gain for stability.

The shape of this stability boundary depends on the system parameters. As B decreases for the same operating point, the system becomes more stable and the inner region encompasses a greater range of gain-phase combinations. As B increases the stable region shrinks and approaches a single point and at larger values of B there is no stable region (Figure (2.6)).

The slope of the compressor characteristic at the operating point also strongly influences the controllability. For this calculation, the compressor slope as well as the mass flow and pressure rise could be arbitrarily selected, allowing a parametric study of the effect of compressor slope on stability. The slope in Figure (2.6) corresponds to $\hat{T}_c$ = 1, the approximate value just into surge. A steeper compressor characteristic at the operating point creates more difficulty for control as will be seen in Section 2.3.3, so the stable region shrinks. Conversely, if the slope is made small enough, the system will become stable without control (zero gain), and the stable region can become essentially a function of the phase only, as in Figure (2.7) with $\hat{T}_c$ = .1.

2.3.3 Effect of Compressor Characteristic Slope

While the compressor characteristic has been fit to a third order polynomial, in practice the actual characteristic is more complex than this and

has local deviations in slope which affect stability. Thus it is useful to determine the maximum slope that the controller can tolerate before the system can no longer be stabilized. This tolerable slope will be a function of the steady-state mass flow, compressor pressure rise, B factor, and controller gain. The stability threshold is defined as the conditions in which the complex conjugate roots can just be brought to the imaginary axis at the origin for the selected gain, producing neutral stability. At any larger slope, that gain will not be able to bring the poles far enough left to a neutral stability point (Figure (2.8)). This stability condition occurs when both the real and imaginary parts of the roots are identically zero. For the real part to be zero:

$$\hat{T}_c = \frac{1}{B^2}\left[\frac{1 - \hat{C}_v \hat{A}_v z_A}{\hat{T}_v}\right] \tag{2.26}$$

In the characteristic equation $as^2 + bs + c = 0$ (Eq. (2.20)), this corresponds to setting b to zero. Note, though, that the slope must also satisfy $4ac = 0$ in order to have zero imaginary components of the poles. This imposes the second condition which defines the maximum tolerable compressor slope, with b set to zero:

$$\hat{T}_c\left[\frac{1 - \hat{C}_v \hat{A}_v z_A}{\hat{T}_v}\right] = 4 \tag{2.27}$$

Choosing a ψ and ϕ for a typical operating point near surge gives the nondimensional valve slopes with respect to flow coefficient and mean area. For a given B factor, the gain can be increased from zero to determine the threshold slope under those conditions at any value of z_A. A sensitivity analysis is first performed to define the deviation in the calculated slopes resulting from changes

in ψ or ϕ. Figure (2.9) shows the results for ψ varying from 1.74 to 1.93 at a fixed value of ϕ = .12. Two values for the B factor are examined: .61 and 1.65. These correspond to the experimental conditions to be discussed. The plot shows that the slope calculations are relatively insensitive to variations in the specified pressure rise. Similarly, a second plot (Figure (2.10)) shows the same analysis performed for fixed ψ = 1.87 with ϕ varying from .08 to .14. Again, mass flow variations have little effect on the tolerable slopes. Therefore the results for the selected representative point (ψ = 1.87 and ϕ = .12) can be considered applicable to all speedlines since all surge points fall in this range. This will be seen in the data of Chapter 5.

From both Figures (2.9) and (2.10), for a given B parameter, there exists a maximum compressor slope beyond which no amount of control gain can stabilize the system. Both this maximum slope and the corresponding z_A to achieve stability under these conditions can be plotted as a function of B parameter.

Figure (2.11) is the curve of maximum compressor slope for stability vs. B. From this plot, it becomes apparent that the controlled system (with the proper gain) can tolerate much steeper compressor characteristics at low B. The control is thus predicted to be more effective in the smaller B configurations. Figure (2.12) is the graph of required controller gain vs. B for the maximum tolerated slope. The gain is smaller at small B's, even though the system can tolerate steeper slopes than for high B parameters. This calculation highlights the B dependence of the system behavior with control.

2.3.4 Variation of Damping and Natural Frequency with Controller Phase

For a general complex controller gain z_A, the coefficients in the characteristic equation (Eq. (2.20)) have both real and imaginary parts. The roots of this equation in general are of the form:

$$s = \beta \pm i\omega_n \tag{2.28}$$

The real part of the poles, β, is the growth rate of disturbances. For positive β any introduced perturbations will grow exponentially at $e^{\beta t}$. For negative growth rates, the perturbations are damped out exponentially. The imaginary part of the roots, ω_n, corresponds to the natural frequency of the oscillations, which may or may not be damped out. At zero gain this frequency is the Helmholtz resonant frequency. If the real part of s is zero, the oscillations will be purely sinusoidal and neutrally stable.

For a given magnitude of the controller gain, the pole positions will change as the phase of z_A is varied, corresponding to a time lag between pressure perturbations and the valve motion. Plots may be obtained for the growth rate and natural frequency of the system at a constant gain magnitude as the phase is swept from 0° to 360°. Figure (2.13) shows the variation in growth rate with phase, normalized by the growth rate at zero magnitude (no control). Since the selected operating point of ϕ = .12 and ψ = 1.87 at B = .61 for this calculation is unstable without control, β_0 is positive. Therefore, any portions of the curve below the horizontal axis reflect a stabilization of the system by reduction in the growth rate. Controller phases between zero and approximately 70° and between 260° and 360° are stabilizing. Maximum destabilization occurs near 200°.

Increasing gain at zero phase moves the poles down to the real axis, where they remain at even higher gains. Thus at zero controller phase shift the natural frequency corresponding to the imaginary part of the poles is always reduced until $(\beta - \beta_0)/\beta_0 = -1$ corresponding to the poles lying on the real axis (Figure (2.14)). At approximately 200° and 340° the resonant frequency remains virtually constant for any gain. Thus the poles are moved horizontally in the direction indicated by β in Figure (2.13). At 200° phase shift the poles are pushed to the right for increasing gain, while at 340° increasing gains tend to stabilize the poles. Finally, note that near 270° the frequency grows at larger gains while the growth rate remains the same. The poles are therefore moved vertically indicating no change in the stability of the system, only a change in the frequency of oscillation. These plots are analagous to those shown by Huang [9], even though the control law is different.

2.4 Summary of Control Modelling

The central conclusions from the linearized compression system model are:

- The control scheme can stabilize the system in a nominally unstable region.

- Both the gain and the phase of the controller must be properly selected for the system parameters at a given operating point.

- There is both a minimum and maximum gain at any controllable operating point which will ensure stability.

- A controller phase of zero degrees is optimum. Some control may be achieved with nonzero phase, but the stable range of control gain is limited. A phase of 180° can drive the system unstable even at nominally stable operating points.

- The B parameter and the slope of the compressor characteristic are the dominant influences on system stability.

- Implementing the controller affects both the perturbation growth rate and the resonant frequency of the system.

CHAPTER 3

Preliminary Results Using the Low Speed Test Facility

3.1 Low Speed Test Rig

The following section gives a brief outline of the low speed results with control. More detailed descriptions of the facility, instrumentation, and methodology will be presented in subsequent chapters which describe the high speed test rig.

The initial low speed data was obtained on a table-top test rig, consisting of a small diesel truck turbocharger manufactured by Holset and a plenum constructed from PVC plastic pipe. This main plenum, in conjunction with the compressor and its inlet ducting, resonated at its Helmholtz frequency of 22 Hz during mild surge.

A gate valve at the plenum exit controlled the steady state throttling of the system. Downstream of this "fixed" valve was the controller: a gate mounted to the center cone of a Radio Shack 5 inch diameter loudspeaker. As a sinusoidal signal was sent to the loudspeaker, the moving coil drove the gate in an up and down motion to change the control throttle area. Air from the plenum exhausted through these valves into a second PVC pipe plenum which served as a mean mass flow measuring device. An orifice was located at the exit of this second plenum, and the pressure drop across the orifice to ambient provided the flow measurement. The volume of this plenum was calculated so that the second plenum would be away from resonance at surge.

The main plenum was instrumented with a high response Setra pressure transducer connected to a static pressure tap. A static pressure tap was also located upstream of the second plenum orifice and connected to a 20 inch inclined alcohol manometer. A third static pressure tap was located approximately one pipe diameter from the bellmouth of the compressor inlet. This pressure drop, an auxiliary measure of the mass flow, was measured using a 20 inch Meriam manometer filled with .855 specific gravity fluid. A magnetic pickup at the impeller face provided a once per rev pulse to measure the turbocharger's rotational speed. Figure (3.1) shows a schematic of the low speed test setup and its associated instrumentation.

A closed-loop oiling system supplied 30W oil to the turbocharger bearings at 30 psig. The compressor was driven by using a steam ejector at the turbine exit with the turbine inlet open to ambient. Limitations of this drive system and the relatively low pressure and temperature ratings of the PVC restricted the maximum operating speed. A typical run was conducted at 30,000 RPM and the maximum speed at which data was taken was 60,000 RPM. 45,000 RPM was the minimum speedline on the map published by Holset for this turbocharger (Figure (3.2)).

The signal from the high response transducer was fed through a phase shifter and pre-amplifier, circuits for which are shown in Appendix B, and into a Harmon/Kardon model hk ultrawideband monophonic DC amplifier. The output of this amplifier drove the speaker to complete the control loop. The phase shifter has switchable ranges from 0° to 180° and from 180° to 360° phase difference between input and output signals. The phase shifter also contains a high pass

filter to remove the pressure transducer DC signal, and it attenuates the incoming signal by a factor of 10. The pre-amplifier allowed the gain to be adjusted continuously from zero to approximately 100. The Harmon/Kardon amplifier boosted the signal to power levels adequate to drive the speaker.

3.2 Low Speed Test Results

To test the controller, the fixed valve was slowly closed down while maintaining a constant compressor rotational speed. The natural surge point was defined as the last observable operating point before flow reversal occurred. When surge was induced, the gain of the controller was increased from zero until the pressure fluctuations were suppressed. It was necessary to keep the controller on throughout the run because, if the controller were switched on or off, a spike in the gate motion resulted which was sufficiently energetic to induce surge. Therefore the controller was left on at zero gain during the entire run until it was needed.

Linear theory predicts that the optimum phase difference between the plenum pressure fluctuations and the area fluctuations produced by the gate motion was near zero. The phase shifter was (empirically) adjusted to provide this phase under surge conditions. It was also noted that if the phase was adjusted to 180° the controller would amplify small perturbations rather than suppress them. Surge could thus be induced in a normally stable region of operation as well as intensified if the system was already in surge. The controller phase could be swept from 0° to 180° and back again to alternately stabilize and destabilize the system.

Data taken at 30,000 RPM indicated that with simple proportional feedback, stabilization of the compressor could be achieved both at and below the natural surge point. The controller set at 0° phase shift allowed the compressor to be stably operated down to a flow coefficient of 50% of the flow coefficient at uncontrolled surge, as shown in Figure (3.3). It was demonstrated that the pressure rise vs. mass flow characteristic did not fall off to the left of the surge line, but rather followed a smooth contour. Thus the linear model could be used in the positively sloped region to predict the behavior of the system under control.

3.3 Conclusions

The preliminary data taken at low speed indicated that the proportional throttle control was a viable scheme, and the added stable operating region provided by this method could be substantial. The success of the controller at the low speeds suggested that control at realistic speeds would be feasible. To run at high speed, however, a new facility would have to be constructed which could withstand the higher temperatures and pressures. In addition a new control valve would have to be designed because the speaker/moving gate could not overcome friction forces under high speed loading.

It was therefore proposed to build an new high speed facility which would incorporate a fast response servomotor-actuated control valve. Sizing of the system was done to achieve a range of realistic values for the B parameter at 110,000 RPM. A maximum B = 1.9 was selected to match the properties of an existing aircraft engine centrifugal compressor at its design point [17]: V_p = 580 in^3, $V_c = L_c A_{in}$ = 91.7 in^3, and $M_{tip} = U/a_{tip}$ = 1.5. The system geometry was designed to have a Helmholtz frequency of 10-20 Hz at all B parameters, both to

simulate realistic conditions and to facilitate the sensing and actuation of the controller.

CHAPTER 4

High Speed Test Facility and Experimental Methods

4.1 Introduction

The test facility was designed to run the turbocharger at speeds near its peak efficiency region, with 110,000 RPM selected as the design speed for the controller. The high temperature and pressure rises associated with this speed were roughly 300°F and 15 psig. The facility was instrumented for both transient and steady state measurements, and all data acquisition was through a personal computer analog to digital interface. A throttle controller was specially designed for this application, including a rotary gate valve with its own position control loop as well as an outer system control loop. The next section gives an overall description of the facility; subsequent sections will describe the different components in more detail.

4.2 General Facility Description

The high speed facility consists primarily of four components, along with their associated support systems and instrumentation. A schematic is shown in Figure (4.1). First, the turbocharger, which is further described in Section (4.3), is driven on the turbine side by the lab oil-free compressed air line at the inlet and the steam ejector at the exit. Both lines are connected by flexible hose couplings. The compressed air system is capable of delivering 700 SCFM at 100

psig, and the line is provided with a gate valve to regulate flow along with pressure gauges on either side of the valve to monitor the delivery. The steam ejector line has a ball valve to regulate its outflow, but this is normally left wide open for maximum capacity. A bypass is provided to vent the compressed air to atmosphere in case the vacuum is lost in the steam ejector line. This avoids overpressurizing the turbine housing.

Air enters the compressor side of the turbocharger through a bellmouth inlet, and exhausts through an exit duct to the second major component: the main plenum. The plenum is constructed of stainless steel and has two outlets. The first is through a ball valve at the bottom of the plenum. The second is through a flange mounted on the side of the plenum directly opposite the inlet tube. Only one exit is used at a time, depending on the control valve configuration. The duct from the compressor exit to the plenum extends through the inner diameter of the plenum to within several inches of the exhaust flange on the opposite side. The control valve was designed to mount either directly onto the end of this duct pipe or on the outside of the exhaust flange. In the first configuration (the compressor exit mode), the air delivered from the compressor must pass through the control valve before expanding into the plenum. The exhaust flange is capped off so that the outflow from the plenum is entirely through the ball valve at the bottom of the plenum. In the second configuration (the plenum exit mode), the air empties directly from the compressor exit duct into the plenum before passing out through the exhaust flange and subsequently the control valve. In this configuration the ball valve at the bottom is shut off so that all outflow is through the control valve. Another ball valve downstream of the control valve in the plenum exit mode allows steady state throttling in series with the control valve, if desired.

Both main plenum exit ducts connect to the final major component: the second plenum. Also constructed from stainless steel pipe, this plenum serves as a steady state mass flow measuring device. It contains flow straighteners to assure a uniform exit profile and an orifice plate at the exit across which to measure the pressure drop associated with the given flow rate. The flow exits the second plenum through this orifice to atmosphere. These components are mounted in a Unistrut stand, and the turbocharger is shielded in the radial direction by both a .375 inch thick aluminum plate and a layer of chain mail.

4.3 Turbocharger and Connecting Systems

4.3.1 Turbocharger Description

The turbocharger used in these experiments is a Holset model H1D developed for diesel engines between 80 and 180 horsepower. The compressor has an inlet duct inner diameter of 2.047 inches (5.2 cm). The impeller has an annular inlet area of 1.938 inches^2 (12.5 cm^2) with a hub to tip radius ratio of .37, and an exit tip diameter of 2.165 inches (5.5 cm). There are 6 blades, 6 splitter blades, no inlet guide vanes, and a vaneless diffuser. The compressor exit duct is 1.732 inches (4.4 cm) inner diameter. A detailed exterior drawing and exploded assembly drawing of the turbocharger are given in Figures (4.2) to (4.4).

The compressor is designed to operate up to a maximum total pressure ratio of 3.1 at 140,000 RPM. At the selected design speed of 110,000 RPM for this experiment, the maximum expected pressure ratio is 2.2. The reader is referred again to Figure (3.2) for the compressor performance map supplied by Holset for the H1D. The compressor rotational speed is measured with a magnetic pickup at

the impeller face; the output pulses are converted to Hertz by an HP 5316A Universal Counter.

4.3.2 Inlet Duct and Instrumentation

4.3.2.1 Short Inlet Duct (Large B Configuration)

Two inlet ducts of different lengths were used to vary the B parameter as desired. The shorter duct was used for the large B configuration. This short inlet duct is constructed from PVC plastic and consists of a bellmouth inlet and an 8.9 inch (22.6 cm) long pipe of 2.04 inches (5.2 cm) inner diameter. The duct is instrumented with a two static pressure taps located at 0° and 270° measured clockwise from the top when viewing the duct from the bellmouth. Both taps are located 4.9 inches (12.4 cm) from the bellmouth inlet face and 4.0 inches (10.2 cm) upstream of the impeller face. A Type K unshielded thermocouple is inserted to the center axis of the duct at 0° approximately .5 inches (1.3 cm) upstream from the pressure taps to measure the inlet flow total temperature.

Inlet flow measurements with the short duct were obtained using a pressure signal from a transducer connected to one of the static pressure taps. The transducer is a Druck model PDCR 811 silicon strain gauge bridge transducer. Its operating pressure range is 0 to 2.5 psig with a full scale output of 25 millivolts at 10 volts excitation. The transducer output was amplified to approximately 10 volts full scale by an Analog Devices model 2B31L high performance strain gauge signal conditioner. This signal conditioning module provided programmable signal amplification and three-pole filtering as well as transducer excitation. The low-pass filter cutoff frequency was set at 500 Hz. The transducer and signal

conditioner were calibrated over the range of 0 to 2 psig against a Baratron reference pressure gauge. A typical calibration curve is shown in Figure (4.5).

The mass flow was calculated from the static pressure drop by assuming incompressible flow through an inlet throughflow area equal to the duct cross-sectional area minus boundary layer blockage. The boundary layer displacement thickness was estimated from laminar flow over a flat plate as:

$$\delta_d = \frac{1.72\ x}{\sqrt{Re_x}} \tag{4.1}$$

where x is the distance from the bellmouth face plane to the inlet static pressure tap. Assuming inviscid, incompressible fluid flow with no swirl, the velocity is measured from the observed inlet static pressure drop by using the Bernoulli equation. The mass flow may then be calculated from the throughflow area:

$$\dot{m} = \rho\,(A_{pipe} - 2\pi R_{pipe}\,\delta_d)\sqrt{\frac{2\Delta P}{\rho}} \tag{4.2}$$

The uncertainty in this mass flow measurement was primarily due to the error band of the pressure transducer. From calibrations of the low pressure range transducers, the combined hysteresis and nonlinearity error was estimated to be ±.005 psi. Near surge at 90,000 RPM, this uncertainty would lead to an uncertainty in flow measurement of ±8%. Therefore this mass flow measurement was found to be useful only for measurements far from surge. In addition, near surge compressor flow disturbances propagated upstream to cause local flow reversal in the inlet duct, although the overall compressor throughflow did not reverse until deep surge occurred. Once surge was approached, the orifice in the

second plenum was used to measure the time-averaged mass flow and the instantaneous inlet flow was calculated by the method in the next section.

4.3.2.2 Long Inlet Duct (Small B Configuration)

The long inlet duct is formed by inserting an extra length of PVC pipe between the short duct and the compressor inlet. The total duct length from the bellmouth face to the impeller face is now 81 inches (206 cm). Because the short inlet duct is still used, the same inlet instrumentation is utilized for both lengths. Note that the added pipe between the static pressure tap and the compressor introduces extra friction losses, so the overall compressor (plus inlet) pressure rise vs. mass flow characteristics must be remeasured. In addition, the acoustic and structural resonant frequencies associated with this long duct rendered the inlet pressure measurement unusable due to a very low signal to noise ratio. Instantaneous compressor mass flow measurements were thus obtained using a plenum mass balance. If all mass storage is assumed to be in the plenum:

$$\dot{m}_1 = \dot{m}_2 + V_p \frac{d\rho}{dt} \tag{4.3}$$

From the isentropic relation:

$$p^{\frac{-1}{\gamma}} \rho = \text{constant} \tag{4.4}$$

$$\frac{d\rho}{dt} = \frac{dp}{dt} \cdot \frac{d\rho}{dp} = \frac{1}{a^2} \frac{d\rho}{dp} \tag{4.5}$$

The mass flow out of the plenum, $\dot{m}_2$, must pass through the control valve. Thus for a given throttle area, a unique mass flow corresponds to the ΔP across the valve. Once the valve has been calibrated at varying throttle areas, the mass flow may be calculated assuming quasi-steady behavior. From the time-resolved plenum pressure a trace of the pressure rise slope could be calculated using discrete time-step differentiation. The slope of the pressure in the time domain was then smoothed using an FFT algorithm [15], and the slope and exit mass flow at every time point were summed to generate the time trace of compressor mass flow.

The uncertainty in instantaneous flow measurement arose from the error band of the plenum pressure transducer and the uncertainty in valve position. From calibrations of the plenum transducer, the combined hysteresis and nonlinearities resulted in an uncertainty of ±.05 psi. An estimated uncertainty in valve position of ±1% near surge at 90,000 RPM leads to an uncertainty of ±1.5% in $\dot{m}_2$. The uncertainty in the pressure time derivative, though, is not easily determined. From a qualitative comparison of the smoothed pressure signal to a pure sine wave, as shown in Appendix E, the error due to the signal differentiation is estimated to be on the order of 1%. With the uncertainty from the pressure transducer included, the uncertainty in the plenum mass storage is estimated to be ±1.5%. Since the mass storage and $\dot{m}_2$ are on the same order, and the amplitude of their sum is approximately 50% of either component, the total uncertainty for $\dot{m}_1$ is estimated to be ±6% in surge. In mild surge the error introduced by differentiating the pressure is substantially smaller (shown in Appendix E), so the total uncertainty is approximately ±4%.

4.3.3 Exit Duct and Instrumentation

At the compressor exit, a short length of high temperature silicone hose connects the turbocharger to the compressor exit duct. The exit duct is 12.3 inches (31.2 cm) long with a 1.6 inch (4.06 cm) inner diameter. It is made from stainless steel in order to withstand the operating conditions in the main plenum. The first several inches of the exit duct lie outside the plenum, providing access for the instrumentation for the compressor exit conditions. Two taps are located approximately 1.5 pipe diameters downstream of the compressor exit plane and can be adapted to accommodate thermocouples, static pressure taps, or total pressure probes. These taps are positioned at 0° and 270° from vertical when viewing the exit duct facing towards the compressor. A manual linear traverser with .001 inch resolution was constructed with the capability to mount on either instrument tap. For these tests, the traverser held a type K unshielded thermocouple to measure the total temperature profile in the duct. A sample temperature profile is shown in Figure (4.6). This profile shows radial variation of exit total temperature near surge on the order of ±3 percent of the average temperature rise. Therefore, only a single point temperature measurement is taken at every desired operating point with the thermocouple junction inserted to the center axis of the duct.

4.3.4 Oiling System

The Holset specifications require an oil supply to the turbocharger bearings of .6 GPM at a supply pressure of 30-60 psig. A recirculating oiling system was set up to provide this lubrication with the following features: 1) unpressurized oil sump, 2) heat exchanger, and 3) positive displacement pump. 30W oil from the sump is drawn first through the heat exchanger where it is

cooled by a water jacket. A positive displacement vane pump then boosts pressure and supplies it to the bearing inlet. A pressure gauge upstream of the inlet monitors supply pressure, and a bypass valve may be used to shunt excess oil flow back to the sump. An adhesive type K surface thermocouple is mounted on the bearing housing to measure bearing temperature.

4.4 Plenum Description and Instrumentation

4.4.1 Main Plenum

The main plenum is constructed of stainless steel 10 inch diameter Schedule 40 pipe. An end cap has been welded to one end, and a flange has been welded at the other to provide access to the plenum interior. In operation, this top end is closed off with a blind flange. The sizing of this plenum was calculated to produce realistic B factors at high speed. With the addition of a movable piston and aluminum inserts to change the volume (along the two available inlet duct lengths), the B factor may be varied from approximately .5 at 60,000 RPM to roughly 2 at 110,000 RPM. The large B case is run with the plenum volume at 1660 $inches^3$ (.0272 m^3). Small B corresponds to a volume of 479 $inches^3$ (.00785 m^3). The large volume has a Helmholtz frequency of 12.5 Hz, with an effective length L_c equal to 34.5 inches (.876 m), while the small volume Helmholtz frequency is 15.5 Hz with L_c equal to 77.2 inches (1.96 m). Appendix C shows the derivation of the effective length. A cutaway view of the main plenum, compressor exit duct, and volume adjustor is shown in Figure (4.7).

Instrumentation in the main plenum consists of a static pressure tap and a type K unshielded thermocouple. The static pressure tap is used to measure the total pressure ratio of the compressor. The pressure transducer used to measure

the plenum pressure is a Druck model PDCR 820 gauge transducer with a 0-50 psig nominal range. The output signal from this transducer is amplified and filtered by an Analog Devices 2B31L signal conditioner, which also provided the 10 VDC excitation. The filter cutoff frequency is set at 500 Hz, and the gain and offset are adjustable. Output was kept close to -5 to +5 volts in the 0-50 psig range. Because early calibrations showed the transducer output to be linear, a two point calibration was routinely performed. The back pressure was switched between ambient and vacuum to measure the voltage output at 0 and 1 atmosphere pressure differential. A typical calibration in shown in Figure (4.8). This transducer could also be connected to the compressor exit duct static pressure tap in order to measure the compressor output when the valve was mounted close-coupled to the compressor.

4.4.2 Secondary Plenum

Like the main plenum, the secondary plenum is constructed from Schedule 40 stainless steel pipe with an end cap at one end and a flange at the other. However, the pipe used is 4 inch nominal diameter. Flow from the main plenum enters this plenum near the cap end and discharges to ambient through an ASME standard sharp-edged orifice plate mounted on the flange. Perforated plates inserted at 1, 2, and 3 pipe diameters downstream of the closest inlet insure a uniform flow profile at the orifice. The diameter of the orifice was sized to 1.75 inches (4.4 cm) to provide adequate resolution of the pressure drop across it at low (~50 SCFM) flow rates yet not too high a pressure drop at the maximum encountered flow rate of 300 SCFM.

The length of the pipe was calculated by setting a requirement on the maximum allowable pressure perturbations at the orifice under oscillating flow conditions. This would decouple the second plenum from the compression system, effecting a steady state mass flow measurement even during the surge cycles. The criterion used to determine the second plenum volume is the Hodgson number, defined as:

$$H = \frac{V_p f \Delta p \rho}{\dot{m} p} \tag{4.4}$$

where f is the frequency of flow oscillation and all other variables are evaluated at the time averaged conditions in the second plenum [12]. The second plenum volume is 528 inches^3 (.00865 m^3) with a straight run length of 42 inches (107 cm). In surge at 90,000 RPM, with the surge frequency conservatively estimated as 10 Hz, H = .1 (Figure (4.9)). For q_{max}/q_{min} = 5 (a measure of the mass flow fluctuations coming into the second plenum), this introduces a 2.5% metering error in the mean mass flow measurements during surge.

The entire second plenum assembly including the orifice plate was calibrated to determine the actual c_d versus Reynolds number based on the orifice diameter, as shown by Figure (4.10)(a). This calibration determined that the assumption of c_d = .6 is valid to within several percent over the range of Reynolds number from $5x10^4$ to $3x10^5$. Figure (4.10)(b) verifies that for any ratio of orifice area to pipe cross-sectional area the discharge coefficient approaches .6 for any Reynolds number above $1x10^4$ [12]. Since a Reynolds number of $5x10^4$ corresponds to a flow rate of about 35 SCFM, a linear approximation to the discharge coefficient will be used to calculate the mass flow.

4.4.3 Plenum Pressure Transducer Frequency Response

To obtain time-resolved measurements and to calculate accurate time-averaged operating points, the pressure transducers were required to respond to frequencies up to at least 30 Hz, a frequency associated with the controller dynamics. It was necessary to calibrate both the high and low range Druck transducers against a pressure signal with a known high frequency response, and a Kulite semiconductor transducer was used for this purpose. The Kulite was mounted in a static pressure tap adjacent to the Druck transducer being tested. The output signals from both transducers were simultaneously displayed on an oscilloscope to observe any attenuation or phase shift of the Druck transducer.

Three characteristic frequencies were seen in the system: deep surge (8-9 Hz), mild surge (12-14 Hz), and controller instability (30-80 Hz). The latter frequency was a function of the controller dynamics, and will be discussed further in Chapter 5. At the frequencies associated with mild surge and lower (8-14 Hz), there was no observable phase shift or attenuation. At 60 Hz, there was an approximately 20° phase lag with no noticeable attenuation. Since this frequency was above the range of the primary surge phenomena, both the high and low pressure range Druck transducers were deemed adequate for unsteady measurements and for the control input signal.

4.5 Control Valve

4.5.1 Valve Description

The original sliding gate valve of the low speed test rig had large friction forces when loaded up at high speed. Therefore, a new design for the control valve was necessary which would incorporate relatively low losses while maintaining a high enough frequency response with reasonable actuation power. The chosen design was a rotary gate valve. The pressure drop was taken across six equally spaced ports on the valve outer diameter. Thus the pressure loading on the valve was equalized around the circumference and the actuation force would only have to be applied normal to the flow.

Figure (4.11) shows an exploded view of the control valve. Air enters the valve through a short straight duct (with the same inner diameter as the compressor exit duct) and is then turned to the radial direction by a curving conical diffuser. The diffuser profile was calculated to keep the annular area constant throughout the turning process and equal to the valve inlet area. The outer cylinder of the valve body contains six rectangular windows, .48 inches (1.22 cm) X .75 inches (1.91 cm)., through which the flow passes after turning radially. A thin cylindrical sleeve fits over the valve body and is machined with six ports identical to those on the body. It is this sleeve which is the rotating member that provides variable area throttling. As the sleeve is turned, the windows are either progressively aligned or misaligned to change the control valve area.

Preliminary difficulties in implementing the controller suggested that with all six ports used for throttling, the angular distance from the full closed position to the equilibrium position at surge was so small that perturbations around this position were unattainable with the resolution of the control system. An inner fixed sleeve was subsequently fabricated to block off all but two

opposing windows in order to gain greater angular travel for the same required area changes.

In calculations using the system model, the coefficient of discharge of the control valve was always assumed to be .6 as for a sharp-edged orifice. For accurate measurements a calibration was performed to determine the actual c_d as a function of valve position. Figure (4.12) gives the pressure drop across the valve versus the mass flow for varying throttle area. The variable $A_{valve}/A_{open} = \alpha$ is the ratio of the actual valve area to the total area of the two ports. It should be noted that even when the valve is entirely shut, there is still some leakage flow. This leakage flow will become a dominant factor for the controller at low mass flows. The discharge coefficients based on the actual valve throughflow area are shown in Figure (4.13)(a). It can be seen that the calculated c_d becomes very large at small α, indicating that the window area is not the only flowpath. Thus the assumption is made that the leakage area consists of the annular gap at both ends between the valve body and rotating sleeve. Modelling this leakage path as another valve in parallel with the ports leads to the discharge coefficients shown in Figure (4.13)(b). Because the values for c_d fall near .6 even with this gross assumption for the leakage and because no other information is known about the leakage flow characteristics, it is concluded that the assumption of a constant discharge coefficient of .6 is adequate for the system model. It should be emphasized that the actual control valve calibration is used for the experimental data, without assuming a discharge coefficient.

For flow calculations from the experimental data, it is only desirable to know how the pressure drop varies with the mass flow. Thus a "total discharge coefficient" may be defined as:

$$b'(\alpha) = \frac{\Delta P \text{ in psig}}{(SCFM)^2} \tag{4.5}$$

Fitting parabolas to the curves in Figure (4.12), a plot can be made of the total discharge coefficient vs. throttle area (Figure (4.14)). For $\alpha < .3$, the following curve fit was used:

$$b' = .038\, e^{(-16.3\alpha)} + .00115 \tag{4.6}$$

For larger area ratios, linear interpolation was used between measured points to obtain the total discharge coefficient. This curve is assumed to hold in unsteady as well as steady flow. In order to validate this assumption, a conservative value for the reduced frequency of the valve unsteadiness is calculated under the severe conditions of approximately 100 SCFM with the valve wide open, and a control signal with a 30 Hz frequency. The characteristic length from the valve opening to the throat, L, is approximately .48 inches, so the reduced frequency defined as:

$$\tilde{f} = \frac{\rho_0 A_{in} \omega L}{\dot{m}} \tag{4.7}$$

is approximately .02. For the quasi-steady assumption to hold, the reduced frequency must be << 1 and this condition is met.

4.5.2 Controller Actuation

4.5.2.1 Control Loop Components

The control valve is actuated by a low inertia DC servomotor, Pacific Scientific model 4VM81-220-1 with a rated torque of 152 oz-in and a torque constant of 9.1 oz-in/amp. For the highest possible frequency response, the motor rotor inertia, as well as the valve rotor inertia, was desired to be as small as possible. This servomotor has a rotor with a 1×10^{-3} oz-in-sec^2 inertia. In comparison, careful design and the use of aluminum kept the valve rotor inertia to 1×10^{-4} oz-in-sec^2. With an inertial load of this order mounted on the motor shaft, the valve can meet the design goal of 100 Hz frequency response.

The servomotor is powered by a Servo Dynamics Corporation model SD2245 pulse width modulated servo amplifier. This amplifier can provide a peak output of 100 VDC at 45 amps. The input power requirements of the amplifier are large enough that a transformer is required to step down from 220 VAC to 100 VAC for bus power. An external inductor is used to protect the amplifier output transistors from overheating in the case of motor failure. The amplifier also contains motor to chassis grounding protection circuitry to provide immediate shutdown. The input signals to the amplifier consist of the position signal, the differentiated position (velocity) signal, and the integrated position signal. The three command signals are combined at a summing junction, and the resulting error signal is amplified and conditioned. The signal is scaled by a current limiter and summed with a current feedback signal. This current difference is amplified and conditioned and sent to the motor to drive the valve. The circuit diagram for the amplifier is given in Appendix B.

The motor shaft angular position, and thus the valve angular position from which throttle area is calculated, is measured with a rotary variable differential transformer (RVDT) angular displacement transducer (Schaevitz model R30D ±15

VDC input/DC output). It is mounted on the opposite end of the motor shaft as the valve sleeve, and since its rotor inertia is only 8.48×10^{-6} oz-in-sec^2 it contributes negligibly to the total inertia. The -3 dB frequency of the transducer is 500 Hz. Its linear output range is ±30° displacement.

The motor position loop is completed when the signal from the RVDT is fed back to the motor controller box which provides the three command signals to the amplifier. This box contains a proportional plus integral plus derivative (PID) controller, along with a limiter to keep the valve command voltage to within ±2 volts which corresponds to a valve position of full open to full closed (30° full scale). The valve cannot be allowed to rotate further in either direction because the next set of sleeve windows would then encroach on the valve body windows. The input signals to the motor controller box consist of the feedback command signal from the RVDT and a trimpot-adjustable DC signal to set the equilibrium position of the valve. Note that the command signal can be shorted to operate the valve as solely a steady-state throttle. The block diagram for the motor position control loop is given in Figure (4.15) and the circuit diagram for the PID controller is shown in Appendix B [13].

The outer control loop performs the proportional feedback law proposed by the theory. In this overall loop the plenum pressure signal is sent real time first to a phase shifter and then to a pre-amplifier before reaching the motor controller box and inner position loop. The phase shifter contains a high pass filter to remove the DC component of the pressure signal, and it also attenuates the signal by a factor of 10. The phase shift is switchable between two ranges: nominally 0° to 180° and 180° to 360°. Since an additional lag is introduced by the motor, however, the overall phase shift must be empirically adjusted to the

desired value during the test run. The circuit diagram for this component is shown in Appendix B [8]. The pre-amplifier is a simple op-amp circuit, as shown also in Appendix B. The variable resistor can be adjusted for gains from 0 to 100. The pre-amplifier also introduces an offset which tends to open the valve with increasing gain. This offset, however, can be counteracted with the DC level trimpot on the motor controller box. Because the motor controller also amplifies the incoming position signal by a factor of 10 before sending it to the motor amplifier, the overall loop gain can be varied from 0 to approximately 100.

4.5.2.2 Controller Dynamics

The transfer functions of each component in the outer control loop were measured over the range of 2-1000 Hz. An input sinusoidal signal was generated at discrete frequencies by a Wavetek model 143 20 MHz Function Generator and the magnitude and phase shift of the transfer function was observed on a Tektronix 2230 100 MHz digital storage oscilloscope. The components tested were the phase shifter, the pre-amplifier, and the motor position control loop, where the input was the signal to the motor controller box and the output was the RVDT valve position signal.

The results are shown in Figures (4.16)-(4.17). It can be seen that both the phase shifter and the pre-amplifier dynamics do not include any unexpected poles or zeros in the frequency range of interest so that rolloff does not occur until much higher frequencies. The phase of the phase shifter transfer function stays constant at the desired setting over the range of frequencies tested. The phase of the pre-amplifier remains close to 180° for all frequencies so that the assumed sinusoidal signal is inverted. In contrast, the motor controller exhibits

some frequency dependence in the range containing the characteristic system frequencies, as well as input signal amplitude dependence. Figure (4.17)(a) shows the results for a low level input signal consistent with the pressure transducer perturbations in mild surge, while Figure (4.17)(b) is the same plot for a high level signal on the order of the oscillations during deep surge. The frequency dependence necessitates some, although not much, empirical adjustment of the phase shifter during the test run to obtain a desired phase shift at the encountered frequencies. The dynamics of the controller can also affect the compression system stability, and this phenomenon will be discussed with the time-resolved measurements of Chapter 5.

The transfer function of the control loop from the phase shifter to the RVDT output was subsequently measured by the same point-by-point method to verify the linearity of the individual components. This transfer function in shown in Figure (4.18), where the attainable phase shifts and gains are bracketed by the minimum and maximum settings of the phase shifter in both range settings.

The overall transfer function of the control loop from plenum pressure signal to valve motion, including the dynamics of the pressure transducer, was tested by injecting white noise pressure disturbances and observing the resulting RVDT signals. A small plenum was constructed with a 5 inch diameter Radio Shack loudspeaker as one wall, and the Druck 50 psig plenum pressure transducer was connected to this chamber at a static pressure tap. The speaker was driven with a white noise signal by a Tektronix Model 2630 Fourier Analyzer signal processor/signal generator. The inputs to the signal processor consisted of the plenum pressure signal on Channel A and the RVDT signal on Channel B. A

diagram of the setup for measuring the transfer function is shown in Figure (4.19)(a). Figures (4.19)(b) and (c) give the phase and magnitude of the measured transfer function. The spikes in phase seen at low frequencies are an artifice of the plotting algorithm when there is a noisy signal near ± 180°. This test was run with an inverting amplifier, so that the phase near 180° in the frequency range of interest is approximately 0° during the actual experiments without the inverter.

It can be seen that although the controller adds dynamics that are not modelled by the proportional control law, these added dynamics are fast enough that they will not affect the compression system behavior in the surge frequency range of 8-15 Hz.

4.6 Data Acquisition

All data acquisition is performed with the aid of an IBM AT personal computer. Analog signals are input through an internal Data Translation DT2801 analog to digital converter card. This board is provided with a DT707 screw terminal panel for the external signal connections, and data acquisition routines are constructed using the Data Translation's PCLAB software. The external screw terminal panel provides space for 8 differential signals, and the following signals are sampled:

1) Plenum Pressure
2) Orifice Pressure Drop
3) Inlet Pressure Drop
4) Valve Position
5) Phase-Shifter Output
6) Pre-Amplifier Output
7) Motor Controller Signal Output

The sampling rate for each channel is 1 kHz, with an overall sampling rate of 8 kHz. With the 1 kHz sampling frequency the Nyquist frequency is 500 Hz, well above the 10-20 Hz frequency range of interest. Both this sampling rate and the input signal range are software selectable. An input range of ±5 volts is selected. Since the A/D board has 12-bit resolution, the input signals are resolvable to 2.4 millivolts. During data acquisition, the AT's direct memory access (DMA) channel is used for the highest throughput rates. Also, since DMA routines are asynchronous other operations may be concurrently performed. In this case, temperature measurements are obtained during the voltage measurements.

The temperature measurements are all obtained from the various type K thermocouples through an Analog Devices μMAC-4000 thermocouple multiplexer. This multiplexer can accommodate up to 12 thermocouple inputs, and it interfaces with the AT through an RS232C serial port. A thermocouple measuring ambient cell temperature is scanned along with the thermocouples located on the test rig.

For this experiment, the AT was used solely for data acquisition. The analog-to-digital converter card, though, has a digital-to-analog converter which will allow command signals to be generated and sent directly to the motor controller. This will enable future digital control schemes to be implemented, with the advantages of flexibility and repeatability not realized by analog control loops.

A schematic representation of the data acquisition setup is given in Figure (4.20). Time-averaged steady-state operating conditions are monitored during the

test runs by the AT. Both time-averaged and time-resolved data may be stored on the AT for any desired operating point.

CHAPTER 5

Experimental Data and Analyses

5.1 Introduction

The effect of the controller on the compressor system was evaluated using time-averaged and time-resolved measurements. The former, in which the compressor is operating steadily after any initial transients have died away, will be considered as steady-state measurements. The compressor may be operating in surge for these measurements provided the surge cycles are periodic. The time-resolved measurements are taken both at steady-state operating conditions and during transients to capture the unsteady features of the system.

The steady-state measurements are presented first to show the shift in surge line with control compared to that without control. This stable operating range extension, though, will be undesirable in practice if the surge suppression is achieved at the cost of compressor efficiency, so the controller must be shown to maintain compressor efficiency in the newly accessible region.

Steady-state data will also show whether the predicted trends in B dependence are correct. The compressor duct effective length, the main plenum volume, and the compressor rotational speed can all be varied to change the B parameter. Increasing the volume and decreasing the inlet length allowed investigations at higher B factors for a given compressor speed, while holding the Helmholtz frequency nearly constant. This avoided frequencies above 20 Hz

associated with unmodelled dynamics. In addition, both the plenum volume and the inlet length could be adjusted to produce the same value of B as in the first configuration at a different compressor speed. The table below summarizes the conditions under which the controller was tested:

	Case 1	Case 2	Case 3
V_p in m^3	.0079	.027	.012
L_c in m	1.96	.88	1.96
Compressor Speed in RPM x 1000	60-110	60-110	70
B parameter	.45-.72	1.26-1.93	.61
Frequency in Hz	15.5	12.5	12.8

Time-resolved measurements were taken to examine the dynamics of the controlled compression system. The unsteady behavior of the uncontrolled compression system was first measured as a baseline for the subsequent control implementation, and the measurements were then repeated, in both stable and unstable regimes, with the controller on. The qualitative surge characteristics are examined at various values of B to determine the B dependence.

With the time-resolved measurements, the dynamics of the controller itself are revealed and prove to be significant for the success of this control scheme. While the system model assumes a simple proportional controller, the dynamics of the real analog system influence the stability of the entire compression system.

In addition to determining that the controller does indeed stabilize the system, measurements were made to validate the linearized model of both the

uncontrolled and controlled systems. These comparisons provided assurance that active control works (reasonably) as predicted and determined that the realized control was not associated primarily with unmodelled compressor dynamics.

5.2 Steady-State (Time-Averaged) Measurements

5.2.1 Motivation and Procedures

The initial experiments were aimed at investigating whether the active throttle valve can successfully suppress surge. Steady-state data was taken first in the small B configuration, Case 1, since the theory predicts greater controllability at lower values of B. Measurements with no control were taken to serve as a baseline for comparison with the controlled measurements. The performance of the compression system both with and without control was assessed through the extension of the surge line and the compressor adiabatic efficiency.

The effect of the B parameter was then explored by changing the system configuration to Case 2 to achieve higher values of B over the same range of speeds as in Case 1. The uncontrolled and controlled measurements were repeated as before. Finally, the effect of B was separated from the effect of speed by taking the same data with the system configured as for Case 3. This data is compared between Case 1 and Case 3 at different compressor speeds but the same B.

5.2.2 Uncontrolled Steady-State Compressor Performance

Case 1, the small volume/large duct length, was the configuration used to initially verify control. Data were taken along constant corrected speedlines

ranging from N_{corr} = 60,000 to 110,000 RPM in 10,000 RPM increments, where corrected speed is defined as:

$$N_{corr} = \sqrt{\frac{T_{ref}}{T_0}} N_{mech} \tag{5.1}$$

The reference temperature was taken as the sea level standard value of 59°F (15°C), and the actual ambient temperature T_0 was measured at each operating point to allow correct adjustment of the mechanical speed, N_{mech}. For the uncontrolled baseline measurements, the control loop was disconnected from the motor controller and the command input to the motor controller was grounded so that only a DC signal was sent to the valve. This signal corresponds to a stationary position of the control valve. The fraction that the valve was open is regulated by the trimpot on the motor controller and can be calculated from the calibrated RVDT voltage.

Steady-state operating points were measured along each speedline with increasing throttling until the surge point is reached. Corrected speed is held constant during these tests by regulating the compressed air supply to the drive turbine. The surge point was defined in this experiment as the last steady-state operating point after which any further valve throttling will induce surge. The compressor was then brought into deep surge and data points taken with increased throttling. While in surge, the time-averaged plenum pressure rise and the compressor adiabatic efficiency drop substantially.

The compressor performance is presented in several ways: 1) total-to-static pressure ratio vs. corrected flow in ft^3/min corrected to 59°F (15°C) and one

standard atmosphere, 2) nondimensional pressure rise vs. nondimensional flow coefficient, and 3) isentropic head coefficient vs. nondimensional flow coefficient. The compressor total-to-static pressure ratio is defined as:

$$\pi = \frac{P_{plenum}}{P_0} \tag{5.2}$$

The static pressure measured in the plenum (which is also taken to be the plenum total pressure) is different from the total pressure at the compressor exit. This difference in total pressure in the plenum and at the compressor exit corresponds to the dynamic pressure in the exit duct, which is, near surge at N_{corr} = 90,000 RPM, approximately 3% of the total pressure at the compressor exit.

The mass flow is measured by the downstream orifice in the second plenum and the dimensional units are ft^3/min corrected to standard conditions. Each of the variables is also nondimensionalized. The compressor pressure rise may be nondimensionalized as either:

$$\psi = \frac{P_{plenum} - P_0}{\frac{1}{2}\rho_0 U^2} \tag{5.3}$$

or

$$\psi_h = \frac{\pi^{\frac{\gamma-1}{\gamma}} - 1}{(\gamma - 1) M_{t0}^2} \tag{5.4}$$

This latter (Eq. (5.4)) is an isentropic headrise coefficient, from Fink [6], which takes into account the flow compressibility. The ratio of specific heats, γ, is taken as 1.4, and the Mach index, $M_{t,0}$, is defined as:

$$M_{t,0} = \frac{U}{\sqrt{\gamma R T_0}} \tag{5.5}$$

The mass flow is nondimensionalized as the flow coefficient:

$$\phi = \frac{C_x}{U} = \frac{\dot{m}}{\rho_0 U A_{in}} \tag{5.6}$$

where C_x is the axial velocity at the impeller inlet annulus. Adiabatic compressor efficiency is defined as the ratio of the isentropic compressor temperature rise to the actual temperature rise, where τ is the actual total temperature ratio:

$$\eta = \frac{\pi^{\frac{\gamma-1}{\gamma}} - 1}{\tau - 1} \tag{5.7}$$

Compressor total pressure ratio vs. mass flow is shown in a conventional compressor map for Case 1 in Figure (5.1)(a), with the surge line indicated. All speeds referred to hereafter are corrected. The pressure ratio at surge ranges from approximately 1.3 at 60,000 RPM to 2.15 at 110,000 RPM. At each speed, surge occurs slightly to the left of the peak, at locations where the characteristic is positively sloped. At low speeds, the slope to the left of the peak is very shallow and the pressure rise actually increases again slightly until surge occurs at a much lower mass flow. This slight "dip" in the characteristic was observed at the 60,000 and 70,000 RPM speedlines. At higher mass flows the slope just to the left of the peak is steeper and surge occurred there. A "knee" in the speedline thus results between the 70,000 and 80,000 RPM speedlines. Figures (5.1)(b) and (c) show the compressor characteristics plotted in the form of pressure rise and head

coefficient, respectively. The head coefficient curves collapse more closely, at least to the right of the peaks, than do the pressure rise curves. Similar comparisons of the head coefficient and pressure rise curves were found by Fink [6].

5.2.3 Controlled Steady-State Compressor Performance

To examine the influence of the control, the compressor was brought close to surge on a given speedline, and the controller was turned on. The control valve was then closed down, with the controller gain set at a fixed magnitude. The lowest attainable flow rate before deep surge, reversal defining the surge, was then measured. The throttle was then opened, the gain was increased, and the process was repeated to reach another controlled operating point at the lowest stable mass flow. In these experiments the phase of the controller was set to 0° since attempts made with the controller at other phases did not reach as low mass flows as with 0°.

Figure (5.2) shows the same pressure ratio vs. mass flow map (Figure (5.1)(a)) with the shifted surge line due to the controller. At 80,000 and 90,000 RPM there was a 20-25% decrease in the mass flow from the uncontrolled surge point. At 100,000 RPM there was a slight extension of the stable region, while at 60-70,000 and 110,000 RPM the extension was negligible. From the plot, it can be seen that below the "knee" of the surge line the controller has little effect on the surge point. In addition the control effect decreases at higher compressor speeds. Since B increases proportionally with speed, this decrease in controllability is expected. B at 90,000 RPM is .61 while at 110,000 RPM the value of B is .72.

On a ψ vs. ϕ plot for the selected representative speed of 90,000 RPM (Figure (5.3)), the extension of the stable operating region is clearly shown. The flow coefficient at the surge point is shifted from .142 to .112 under control, a decrease of 21%. With control the compressor pressure rise is stabilized near the same level as prior to surge. Once the controller loses its effectiveness and the system surges with the controller still on, the compressor operates along the same characteristic as in normal surge. The compressor efficiency at this speed does indeed drop off in the newly accessible controlled region (Figure (5.4)), but the decrease in efficiency follows the trend in the normally stable region, so does not fall off as far as in (uncontrolled) surge.

5.2.4 B Parameter Dependence of Controllability

To test the dependence of the controller on the B parameter, the test rig was configured for Case 2, the large volume/small duct length case. Since B scales as $\sqrt{V_p/L_c}$ and the Helmholtz frequency scales as $\sqrt{V_p L_c}$, the B parameter was increased by a factor of 2.7 at a given speed while keeping the actual frequencies of interest of the same order.

The compressor map that was measured for Case 2 is shown in Figure (5.5). The surge line with no control has changed very little from the uncontrolled surge line of Case 1 -- the B dependence for natural surge is weak in this range of B values. The main feature to note is the shift in the "knee" of the surge line from between 70-80,000 RPM in Case 1 to between 60-70,000 RPM. From the analysis of the maximum tolerable compressor slope, it is expected that at smaller values of B a steeper slope is necessary for instability. Experimental data shows that the speedlines have a small dip near the peak. At high B values this locally steep

region produces surge, but at smaller B the compressor will not surge until much lower mass flow. Since the dip is larger at higher speeds, the "knee" shifts upward as B decreases.

Figure (5.5) also shows the controlled region for the larger B case. As expected, the largest extension of the stable operating range occurred at the lower speeds, with control falling off at higher speeds and therefore higher B values. Again there was negligible control below the surge line "knee". Comparing the larger B Case 2 (Figure (5.5)) to the smaller B Case 1 (Figure (5.2)), the effect of varying B with constant speed can be seen. In the regions where control was accomplished at both B values, i.e. 80-100,000 RPM, the surge line extension was at least 50% larger in terms of mass flow at the lower B values than at the higher B on a given speedline.

The larger B configuration did produce a controlled stable region at 70,000 RPM that was a 25% reduction in mass flow compared to the uncontrolled surge point, whereas no control was observed in the small B case. However, in the small B configuration the compressor naturally surged at the same point to which the large B case could control, since the "knee" had shifted above 70,000 RPM. Therefore in neither configuration could control be achieved below a mass flow of ϕ = .09. It should also be noted that neither controller was able to achieve control at 110,000 RPM. In Case 1 this corresponded to B = .72 and in Case 2 to B = 1.95. At speeds where control was effective, the trend of B dependence showed that smaller B does produce greater control. In physical terms the small B case has less capacitance between the energy input (compressor) and the controller, so the controller can more directly affect the compressor to ensure stability.

Comparing controllability at the same speeds with different B parameters shows the B dependence of the control scheme effectiveness. However, the decreasing controllability in a particular system configuration at increasing speeds might be attributed either to an increase in B factor or to an increase in impeller tip Mach number, both of which scale with rotor speed. Thus an experiment was conducted to separate the effects by changing the configuration to match B parameters at different speeds. The compressor was run in the configuration of Case 3 at 70,000 RPM to match B = .61 of Case 1 at 90,000 RPM. The measured shift in surge point for this case was from ϕ = .121 to ϕ = .092 (Figure (5.6)), a difference of .029 as compared to a similar shift in ϕ of .030 for Case 1 at 90,000 RPM. In Case 1 at 70,000 RPM no control was achieved. Therefore speed (or Mach number) per se does not limit controllability.

5.2.5 Summary of Steady-State Uncontrolled and Controlled Measurements

The conclusions from the time-averaged measurements of the system are:

- Active throttle control stabilizes the system below the natural surge point.
- In controlled operation the compressor pressure rise remains near the pre-surge level.
- Compressor efficiency is maintained during control.
- Control ability is a function of the B parameter.
- Control ability decreases as B increases.
- The positioning of the uncontrolled surge line "knee" is a function of B, and the controller is ineffective below it.

5.3 Time-Resolved Measurements

5.3.1 Motivation and Procedures

From the time-averaged results it may be concluded that this method of active throttle control can provide significant stabilization of the system under a variety of operating conditions. There are still questions which need to be investigated through time-resolved measurements. Among these are: How does the controller affect the oscillatory behavior of the system both under control and after the controlled system surges? Can the controller eliminate existing surge? What happens to the system if the controller is shut off in a normally unstable region? What dynamics does the controller introduce to the system? What controller gain and phase will produce the most control? The next section addresses these issues through the examination of system parameters in the time domain.

The unsteady behavior of the system with and without control provides insight into how the controller suppresses surge. Time-resolved measurements are taken of the following parameters: compressor pressure rise, inlet mass flow, orifice mass flow, and control valve area. Data is sampled at 1 kHz for 1 second when the compressor is operating in steady or oscillatory behavior. When the transient system behavior is of interest, the sampling time is increased to 4 seconds. The results are plotted as perturbations in the time domain and/or oscillations in the pressure rise-mass flow plane.

5.3.2 Unsteady Behavior of the System Without Control

With the system configured in the small B (Case 1) configuration, time-resolved measurements of the perturbations in nondimensionalized pressure rise $\delta\psi$, inlet mass flow ϕ_1, and orifice mass flow ϕ_2 were taken at successive points along the constant 90,000 RPM corrected speedline without the controller. The points recorded extended from the right of the peak of the characteristic to well into surge. Figure (5.7)(a) shows the time-averaged nondimensional characteristic with the measured points (A-E) indicated. Figure (5.7)(b) shows the perturbations in nondimensional plenum pressure rise ψ at successively smaller flow rates, while Figure (5.7)(c) shows the perturbations in nondimensional compressor mass flow at the same operating points.

Point A, where the mean flow coefficient is .183, lies to the right of the characteristic peak and the compressor is operating stably. The perturbations in pressure rise and mass flow are on the order of the noise in the system. Point B lies just to the left of the peak. Here the system shows oscillations at a frequency of 13.5 Hz, compared to the predicted Helmholtz frequency of 15.5 Hz. The slope of the compressor characteristic is very shallow and the compressor is operating in mild surge. Point C is the last stable operating point before deep surge. The compressor again is in mild surge, but the amplitude of the perturbations has increased and the frequency has decreased slightly to 13 Hz. Finally, points D and E show the system behavior in deep surge. The oscillations in plenum pressure are much larger and the frequency of about 9 Hz has some association to plenum blowdown and repressurization [6]. The mass flow also fluctuates strongly, reversing for a portion of the cycle. Figure (5.8) shows the mild surge cycles at point C in the pressure rise-mass flow plane, plotted over the time-averaged characteristic. Figure (5.9) is a similar plot in deep surge at point D. The surge cycles are traced out in a counterclockwise direction.

5.3.3 Unsteady Behavior of the System With Control

At controlled points A'-D' (Figure (5.10)(a)), the perturbations in nondimensional pressure rise and mass flow are substantially suppressed, as shown in Figures (5.10)(b) and (c). The perturbations in nondimensional valve area, $\delta\hat{A}_V/\hat{A}_V$, are shown for the same operating points in Figure (5.10)(d). Surge has been successfully suppressed, but a higher frequency is now seen. All perturbations contain a strong frequency component at 60 Hz which is well above any frequency that the author can associate with the geometry of the compression system. It is therefore postulated that this frequency stems from the controller dynamics. The frequency will later be determined to be a function of the system geometry, though, as it will vary for different configurations. This "controller instability" mode will be examined in more detail later. A power spectral density plot of the valve motion under control reveals that even during the controller instability the valve is still responding to a lower frequency associated with deep surge (Figure (5.11)). The suppression of system oscillations is clearly seen in Figure (5.12), which shows the pressure rise vs. mass flow perturbations at point D' along the compressor characteristic with the controller on.

Fink has pointed out that compressor dynamics themselves provide some measure of stabilization through variations of rotational speed during an instability [6]. This stabilization becomes more effective at lower surge frequencies where the compressor speed can closely follow the instability. Because the controller can affect the resonant frequency of the system, as discussed in Section (2.3.4), it is possible that the mechanism of surge suppression

may involve this lowering of the surge frequency which allows the compressor more time to vary in speed. A power spectral density calculation was thus carried out on all controlled surge points, as well as the uncontrolled deep surge points in the same flow coefficient range. The PSD of the plenum pressure fluctuations with no control determined the deep surge frequency to be 8.8 Hz. Similar computations performed at controlled points A'-D' showed that the resonant frequency was reduced from 8.8 Hz to 5.9 Hz at point B', but increased to 8.8 Hz at C' and to 10.7 Hz at D'. The compressor speed variations, therefore, are not the reason for surge suppression.

When the throttle was closed enough that the controller could no longer maintain stability, the surge had much the same features as without control. In the time intervals between blowdown and repressurization, while the compressor was operating along its characteristic, the "controller instability" produced higher frequency perturbations in pressure rise and mass flow. The nondimensionalized valve area, plenum pressure, and compressor mass flow perturbations in surge with the control on are shown in Figure (5.13). It can be seen that the fundamental frequency in deep surge has been reduced by the introduction of the controller. A plot of the surge cycle on the compressor map with the controller on is shown in Figure (5.14).

The pressure perturbations of the system both with and without control are shown as RMS and peak amplitudes in Figure (5.15). Without control the RMS value for the pressure perturbations approaches a maximum level as the surge frequency increases, while the peak amplitude is reached immediately after surge is initiated. It is seen that below the flow coefficient at natural surge, the controller suppresses the pressure fluctuations to a level below that of mild surge.

Once surge can no longer be controlled, both the peak level and RMS amplitude of perturbations are still lower than those with no control.

The previous time-resolved measurements under control were all taken during stable or steady-state oscillatory operation. The transient behavior of the system when the control is turned on or off is also a measure of the control effectiveness. Figure (5.16)(a) shows the nondimensional perturbations in valve area, pressure rise, and mass flow for the system in deep surge with the controller off. At t = 1.03 seconds, the controller is switched on at a previously set controller gain and phase. It can be seen that the controller captures the surge and suppresses the fluctuations within one surge cycle. In the pressure rise-mass flow plane, the surge cycles are shown to be suppressed as soon as the compressor reaches the time-averaged operating point on its characteristic (Figure (5.16)(b)). The controller can thus capture the instabilities even though the system is operating in a highly nonlinear surge regime. It should be noted that the implementation of the controller increases the time-averaged flow coefficient slightly from ϕ = .083 to .092 because the pressure increases (this is basically motion along a constant throttle line). Even though the flow coefficient, however, increases it still remains well within the no control surge region.

Another view of the transient behavior is given by switching off the controller. This is shown in Figure (5.17), at t = 1.16 seconds. The absence of control action allows small perturbations to grow within several surge periods, to the large amplitude deep surge cycles.

5.3.4 B Parameter Dependence of the Unsteady System Behavior

The system unsteady behavior in surge both with and without control is strongly a function of the B parameter. With no control, the amplitude of the plenum pressure fluctuations remains virtually constant but the behavior in between each surge cycle is quite different. At small B factors, when the compressor reaches the last stable point of operation, any further throttling triggers deep surge, with each plenum blowdown and repressurization followed immediately by another blowdown/repressurization. Further throttling does not change the surge behavior other than to slightly increase the surge frequency. At higher B factors, though, the compressor operating just to the left of the surge line can experience a single surge cycle and then recover for a period of quasi-steady operation before another surge cycle occurs. The compressor sounds as though it is "barking" during this mode. As the throttle is closed down, the "barks" become more frequent until the system does not recover stable operation between surge cycles (Figure (5.18)). Similar behavior was found by Fink [6] for a system with a much larger B parameter.

The dynamics of the controller also appear to be dependent on the B parameter of the system. Figure (5.19) shows the nondimensional valve area perturbations at 90,000 RPM for both the small B and the large B cases. In both configurations, it can be seen that a frequency much higher than the surge phenomenon is present. In the small B (B=.61) case the frequency is 60 Hz, and at large B (B=1.65) the frequency has increased to 83 Hz. Both the pressure rise and valve motion still contain the deep surge frequency, but the pressure rise and mass flow oscillations at this frequency have been greatly reduced compared to no control. The high frequency "controller instability" does not appear to limit the controller effectiveness, at least in the configurations tested, but it did appear at gains near the maximum allowable magnitude for control. At smaller gains no

controller instability was found. The oscillations during controller instability were small so they did not preclude surge suppression. However the presence of unmodelled dynamics highlights the importance of proper design for future controllers and suggests that a more detailed model be constructed for a more sophisticated implementation of active throttle control.

5.3.5 Summary of Time-Resolved Measurements

The main features of the time-resolved behavior of the compression system both with and without control are summarized below:

- The compression system without the controller exhibits different modes of instability as a function of mass flow. To the right of the peak, the compressor operates stably. Just to the left of the peak mild surge develops with oscillations in pressure rise and mass flow occurring near the system's Helmholtz frequency. Further to the left the compressor goes into deep surge with large amplitude oscillations and flow reversal. The frequency decreases from 12-15 Hz in mild surge to 8-9 Hz in deep surge.

- In deep surge, the plenum experiences blowdown and repressurization. The compressor appears to follow its forward flow characteristic during the repressurization portion of the cycle.

- The controller can successfully suppress the surge oscillations to an amplitude below that of mild surge.

- The controller adds unmodelled dynamics to the system which may affect the system stability.

- The controller does not stabilize the system merely by reducing the surge frequency to allow the compressor more time to adjust its speed to increase stabilization.

- Deep surge with the controller on is less severe than normal surge.

- The controller can suppress existing surge even though the surge phenomenon is highly nonlinear.

- The B parameter affects the ability of the compressor to recover between surge cycles. At lower B the compressor goes into full surge as soon as the surge line is crossed. At high B the compressor may recover between surge cycles until further throttling produces full deep surge.

- The B parameter also influences the controller instability modes. As B increases the frequency of the controller instability increases.

5.4 Comparison of Experimental Measurements to Model Predictions

As a test of the validity of the linearized model, comparisons may be made between the system behavior predicted by the model and the observed behavior. These comparisons include both those without control, to validate the lumped

parameter model of the compression system, and those with control to verify the proportional controller model in the compression system.

5.4.1 Compressor Transfer Function

The compressor transfer function was briefly studied to compare with theoretical predictions. The transfer function between the plenum pressure rise as the input and the compressor mass flow as the output was measured in the large B configuration at 90,000 RPM near the peak of the characteristic. The amplitude and phase of the transfer function were measured point-by-point for frequencies in the 2-40 Hz range. The plenum pressure rise was oscillated by driving the control valve at the desired frequency with a sinusoidal signal. The compressor mass flow was calculated from the plenum pressure and valve motion by the mass continuity method. The results are shown in Figure (5.20).

The results of the transfer function measurement were not conclusive. It is thought that the mass flow measurements are not precise enough due to the technique used (measuring the mass flow indirectly from the plenum pressure and the valve area). Time limitations prevented an independent measure of the mass flow with a hot-wire anemometer, and these measurements are considered a priority for future active control investigations.

5.4.2 Control Action Required for Surge Line Extension

The theory predicts that a certain gain and phase will produce the optimum reduction in stable mass flow with given system parameters. In addition, the model predicts the most extreme conditions the controller can handle, i.e. the

maximum compressor characteristic slope before losing ability to suppress surge. To estimate what the actual characteristic slopes were at a controlled operating point, a compressor map was needed which would extend the constant speedlines to the left of the surge line under control. This was accomplished by close-coupling the control valve to the compressor exit duct. The volume was then essentially reduced to the exit duct volume, resulting in a B small enough to avoid surge until very low flow rates. The control could not be tested here because the system frequency was increased to well above the control valve frequency response.

The compressor map in the close-coupled configuration is shown in Figure (5.21)(a)-(c) in terms of π vs. SCFM, ψ vs. ϕ, and head coefficient vs. ϕ. From these characteristics, the nondimensional slope could be estimated, although a precise value cannot be obtained due to the local variations. Therefore the slope could only be bracketed and used to show whether the model predictions were reasonable or not.

The controlled points on the 90,000 RPM speedline in the small B configuration (B = .61) were compared to the theoretical predictions. The gain and phase of the controller at each point was measured from the time-resolved data, and the slope of the characteristic at each time-averaged operating point was estimated. At each controlled point, the phase of the controller was zero degrees, as this was found to produce the most control. The theory predicted that a phase of approximately 340° was optimum. The results for the controller gain are shown in Figure (5.22) for points (A'-D'), with the gain multiplied by the nondimensional mean valve area. An estimation of the uncertainty in the compressor slope is shown on the plot as error bars. It can be seen that since the

compressor slope for a given gain is lower than the maximum predicted tolerable slope, the controller has some theoretical margin for improvement. This indicates that the controller could suppress surge even though its performance was not optimized. Note also that one controlled point lies on a negative slope where the uncontrolled compressor recovers slightly from mild surge before developing into deep surge.

5.4.3 Measured Stability Boundary

The stability boundary was discussed in Section 2.3.2, and it shows the region in the controller gain-phase plane where stable operation may be achieved. In general, the maximum range of gains for stable operation occurs at 0° phase shift between the plenum pressure perturbations and the valve motion, and the stable gain range decreases as the phase is shifted either positively or negatively. At some magnitude of controller phase, no gain will stabilize the system. This leads to a closed region in the gain-phase plane where compressor stability is ensured. The size and shape of this region is B dependent. A comparison between the measured stability boundary and the theoretical prediction is made at 90,000 RPM for the small B configuration and the results are shown in Figure (5.23). The compressor slope for the calculation was set to match the maximum gain at zero degrees phase, and the values for ϕ and ψ were taken from the steady-state measurements. The qualitative theory and experiment comparison is fairly good, although there are specific quantitative differences. The measured stable region is somewhat larger than that predicted by the model, smaller minimum gain is needed for stability than predicted, and stability is achieved over a larger range of controller phase.

5.4.4 Shift in Measured System Resonant Frequency

The frequency shift predicted in Section 2.3.4 considered the change in frequency of small perturbations as the controller phase was varied from 0° to 360°. In practice, the frequency shift could only be measured while the system was in deep surge with the controller on. If the measurements were attempted either in stable controlled operation or in mild surge, the controller would induce deep surge when the phase difference between valve and pressure perturbations became appreciable. Thus the comparison had to be made between the linearized model and the nonlinear compressor instability. The results are shown in Figure (5.24). The comparison of the theoretical frequency shift to the actual data shows that even though the surge phenomenon is nonlinear, the model does capture essential features. The frequency shift at 0° phase shift is shown to be about 20%, and by driving the controller out of phase with the pressure perturbations the frequency is driven higher than in normal surge.

Chapter 6

Conclusions

6.1 Discussion of Conclusions From This Experiment

The active throttle control scheme has been demonstrated as a viable method of surge suppression for a centrifugal compressor. With the control valve in place in the compression system, the minimum mass flow for stable operation was reduced by 20-25% from the uncontrolled surge point. This control was achieved without degrading system performance in terms of compressor adiabatic efficiency.

The time-resolved behavior of the system with the controller revealed the substantial suppression of pressure and mass flow oscillations at controlled steady-state operating points. Both the shift in the surge line and the decrease in the surge margin with control open up the accessible operating region on the compressor map.

The linearized model of the compression system has been shown to be adequate to predict the features of surge behavior and the effect of the throttle control. Although the model only considers a linearized system for small perturbations around a mean operating point, the controller has been demonstrated to suppress surge even when the system behavior is in a highly nonlinear regime. Therefore the control scheme may be used to suppress deep surge as well as to prevent surge from occurring in the first place.

The linearized model predicts the strong dependence of the controller performance on system parameters. In particular, the B parameter has been shown to strongly influence the ability of the control valve to affect the compressor. With larger B values, the valve becomes more decoupled from the compressor and more control effort is required for stabilization. Eventually at high enough values of B, the capacitance of the plenum is large enough so that the valve is effectively too remote to influence the compressor. The control effort required at a given B factor is also highly dependent on the slope of the compressor characteristic at the time-averaged operating point. A steep compressor slope means a larger energy input of the compressor for small perturbations and thus more energy dissipation required by the controller.

Overall, this experiment is seen as providing a useful test bed for active throttle control and proven that the control scheme can provide substantial stabilization under typical operating conditions. This even though the simplest possible control scheme was used, so that significant improvements also appear likely.

6.2 Suggestions for Further Study

The investigation of this control scheme revealed several areas requiring further exploration. First, the compressor transfer function measurements must be made with a hot-wire anemometer in order to have confidence in the modelling of the compression system.

The controller dynamics must also be more thoroughly investigated. The controller instability observed during these experiments was unmodelled and may have precluded larger surge line extension. Because the effect of the controller instability was apparent even with this very simple controller, the successful implementation of a more sophisticated control scheme would demand the full characterization of the additional dynamics.

The problems associated with repeatability and reliability of an analog control loop suggest that a future controller be implemented digitally. A digital control loop allows flexibility in testing various feedback laws to optimize control. Such an experiment is being initiated at the high speed test facility, and will use a personal computer with analog-to-digital and digital-to-analog interfaces to process the control signals. The digital controller will first attempt to duplicate the analog controller results to verify its design, then will explore more complex throttle control schemes.

One throttle control scheme that appears promising is the close-coupled controller with the valve between the compressor and the plenum. Because the control valve must balance the loss of usable plenum pressure rise across it with the benefits of controllability, a simple control law did not prove adequate. Since the close-coupled control valve effectively modifies the compressor to create a compressor with "different" characteristics, this type of control suggests that the valve motion may be able to be tailored for operation in different regions of the compressor map. This is an area that is also regarded as having high priority for further study.

REFERENCES

1) Chen, G.T., "Active Control of Turbomachinery Instabilities -- Initial Calculations and Results", M.S. Thesis, Department of Aeronautics and Astronautics, MIT, August 1987.

2) Dean, R.C., Jr. and Young, L.R., "The Time Domain of Centrifugal Compressor and Pump Stability and Surge", Journal of Fluids Engineering, Transactions of the ASME, March 1977, pp. 53-63.

3) Dussourd, J.L., Pfannebecker, G.W., and Singhania, S.K., "An Experimental Investigation of the Control of Surge in Radial Compressors Using Close Coupled Resistances", Journal of Fluids Engineering, Transactions of the ASME, March 1977, pp. 64-75.

4) Emmons, H.W., Pearson, C.E., and Grant, H.P., "Compressor Surge and Stall Propagation", ASME Transactions, Vol. 77, April 1955, pp. 455-469.

5) Epstein, A.H., Ffowcs Williams, J.E., and Greitzer, E.M., "Active Suppression of Compressor Instabilities", AIAA-86-1994, AIAA 10th Aeroacoustics Conference, July 1986.

6) Fink, D.A., "Surge Dynamics and Unsteady Flow Phenomena in Centrifugal Compressors", Ph.D. Thesis, Department of Aeronautics and Astronautics, MIT, May 1988.

7) Greitzer, E.M., "The Stability of Pumping Systems -- The 1980 Freeman Scholar Lecture", Journal of Fluids Engineering, Vol. 103, June 1981, pp. 193-242.

8) Horowitz, P. and Hill, W., The Art of Electronics, Cambridge University Press, Cambridge, 1980.

9) Huang, X., "Active Control of Aerodynamic Instabilities", Ph.D. Thesis, Department of Engineering, University of Cambridge, July 1988.

10) Jansen, W., Carter, A.F., and Swarden, M.C., "Improvements in Surge Margin for Centrifugal Compressors", in Centrifugal Compressors, Flow Phenomena and Performance, AG28.

11) Mazzawy, "Surge-Induced Structural Loads in Gas Turbines", Journal of Engineering for Power, Transactions of the ASME, Vol. 102, January 1980, pp. 162-168.

12) Ower and Pankhurst, The Measurement of Air Flow, Pergamon Press Ltd., Oxford, 1966.

13) Paduano, J., Unpublished Report on Design and Implementation of Motor Controller, MIT, 1988.

14) Palm, W. J., III, Modeling, Analysis, and Control of Dynamic Systems, John Wiley & Sons, Inc., New York, 1983.

15) Press, W.H., Flannery, B.P., Teukolsky, S.A., and Vetterling, W.T., Numerical Recipes -- The Art of Scientific Computing, Cambridge University Press, Cambridge, 1986.

16) Reeves, G.B., "Estimation of Centrifugal Compressor Stability with Diffuser Loss-Range System", Journal of Fluids Engineering, Transactions of the ASME, March 1977, pp. 76-83.

17) Sehra, A., Private Communication.

18) Senoo, Y. and Kinoshita, Y., "Influence of Inlet Flow Conditions and Geometries of Centrifugal Vaneless Diffusers on Critical Flow Angle for Reverse Flow", Journal of Fluids Engineering, Transactions of the ASME, March 1977, pp. 98-103.

19) Stenning, A.H., "Rotating Stall and Surge", Journal of Fluids Engineering, Transactions of the ASME, Vol. 102, March 1980, pp. 14-20.

20) Taylor, E.S., "The Centrifugal Compressor", Part J in Aerodynamics of Compressors and Turbines, W.R. Hawthorne, editor, Princeton University Press, Princeton, N.J., 1964.

21) Toyama, K., Runstadler, P.W., Jr., and Dean, R.C., Jr., "An Experimental Study of Surge in Centrifugal Compressors", Journal of Fluids Engineering, Transactions of the ASME, March 1977, pp. 115-131.

22) Wright, S. and Lambie, D., Undergraduate Part II Report, "Stability of a Compression System", Cambridge University, Engineering Department, 1984.

ACTIVE COMPRESSOR STALL STABILIZATION

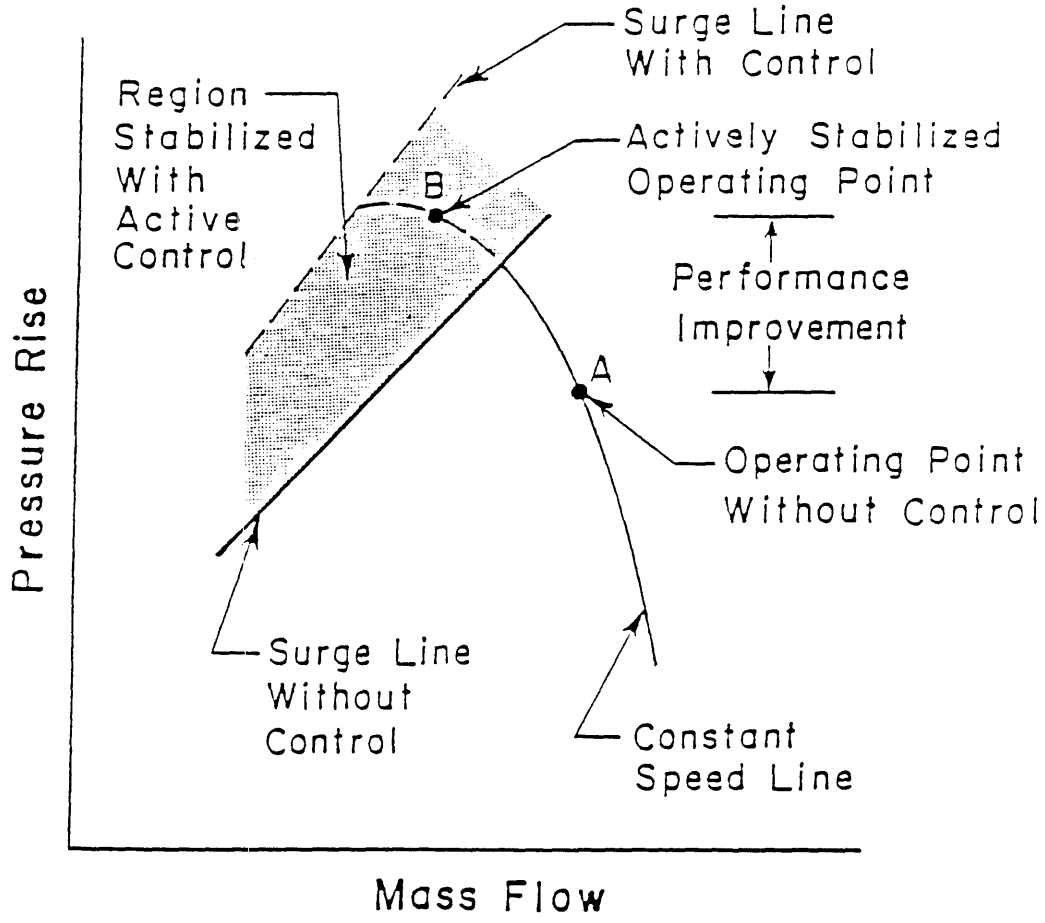

Figure 1.1 Active Surge Control

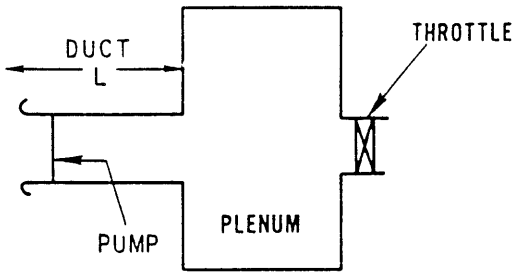

PUMPING SYSTEM

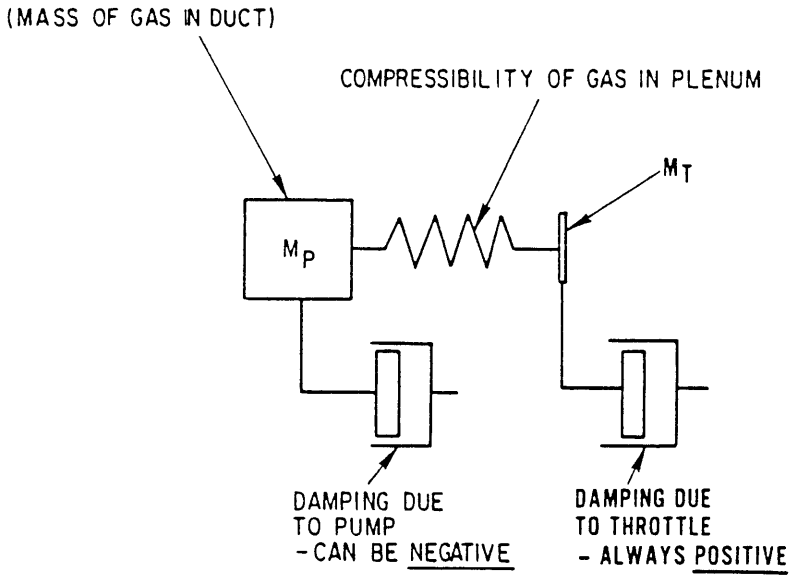

MASS/SPRING/DAMPER SYSTEM

Figure 1.2 Lumped Parameter Model of a Simple Compression System

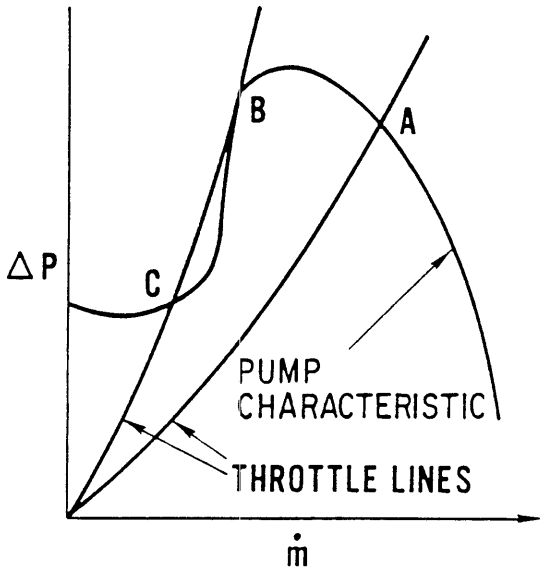

STATIC INSTABILITY

UNSTABLE IF SLOPE OF PUMP CHARACTERISTIC GREATER THAN SLOPE OF THROTTLE LINE (POINT B)

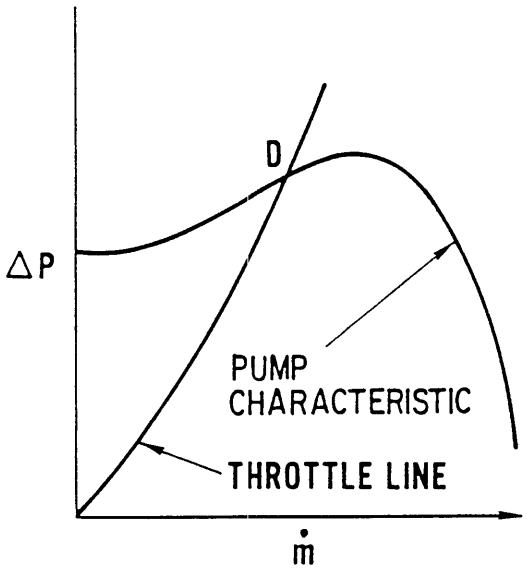

DYNAMIC INSTABILITY

EVEN IF STATICALLY STABLE SYSTEM CAN BE DYNAMICALLY UNSTABLE (POINT D)

Figure 1.3 Stability Criteria on the Compressor Characteristic

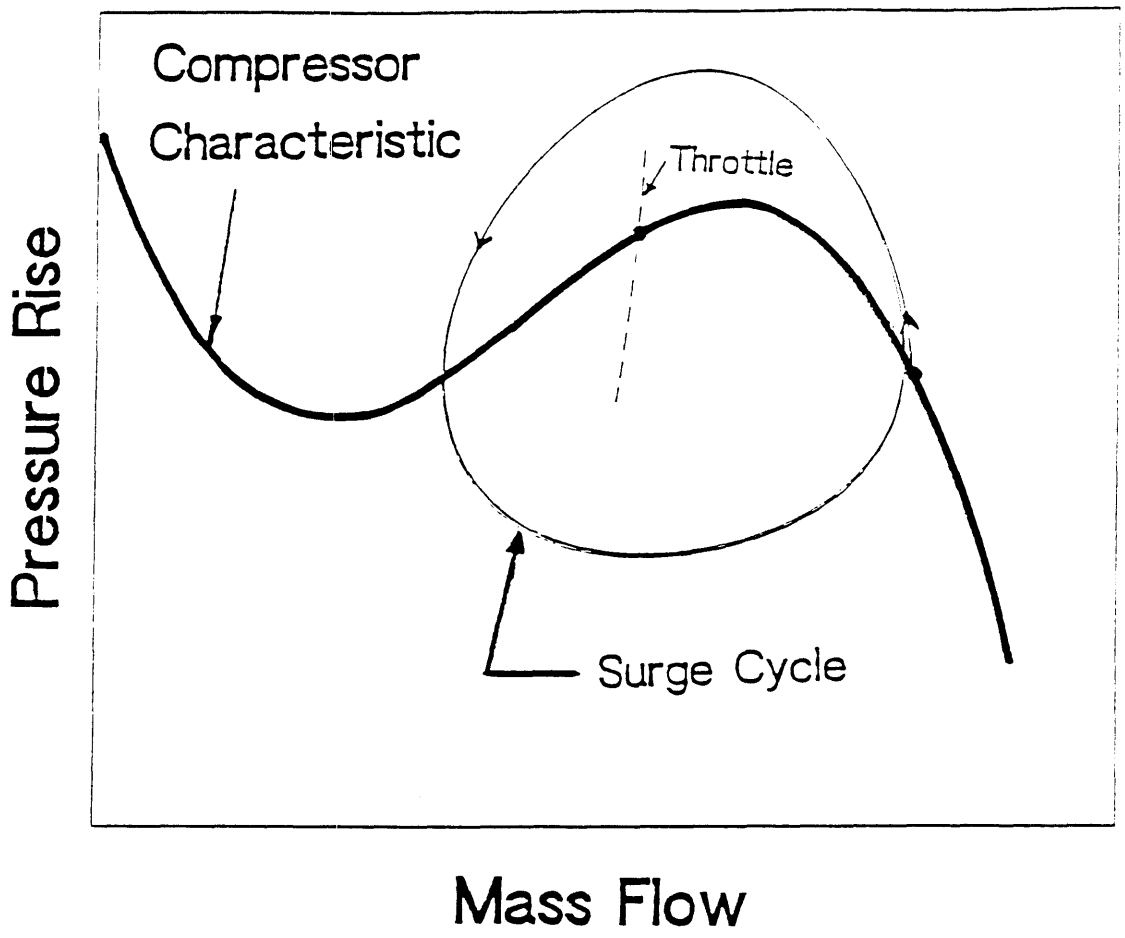

Figure 1.4 Surge Limit Cycle

COMPRESSION SYSTEM WITH CONTROL
- Simple Generic Model -

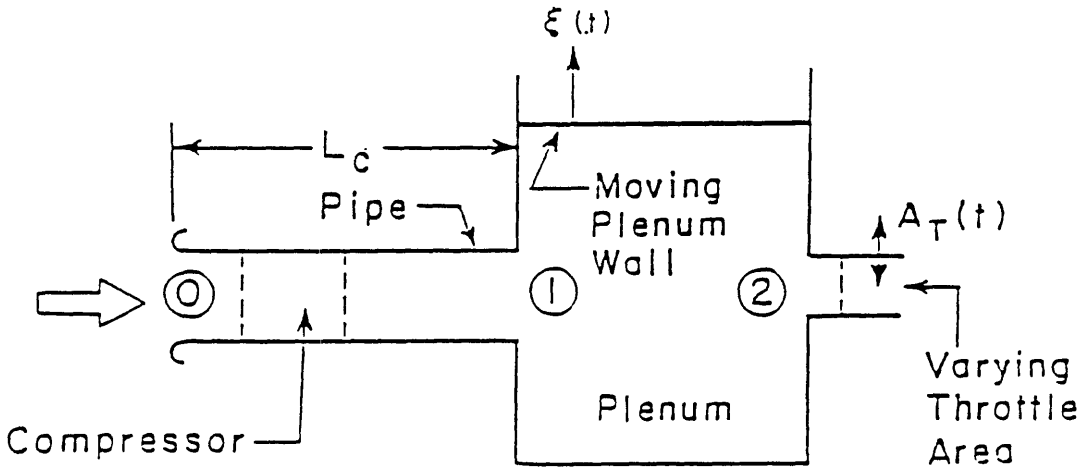

Figure 1.5 Lumped Parameter Model of Actively Controlled Compression System

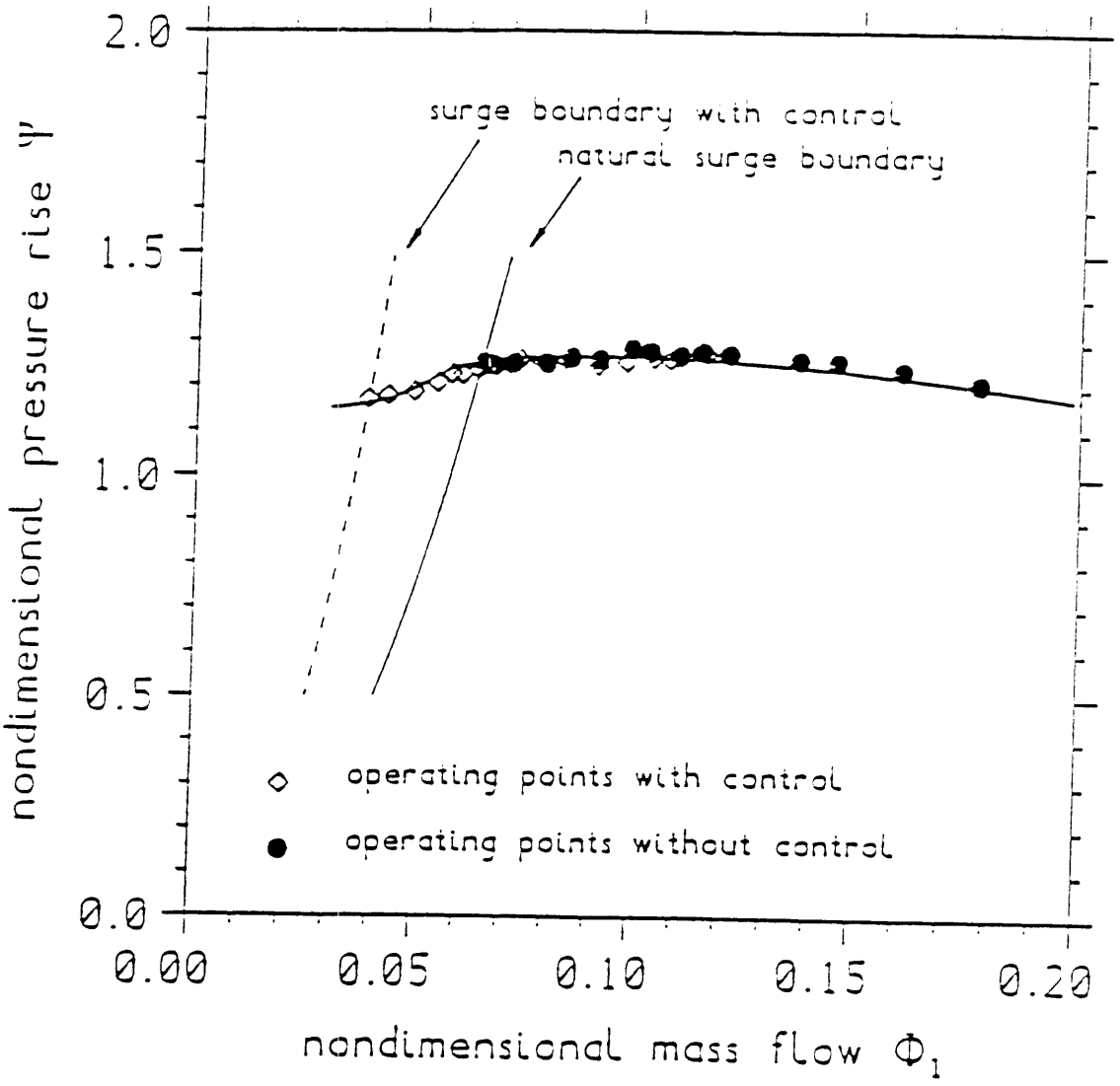

Figure 1.6 Active Volume Control Experimental Results (Huang) [9]

ACTIVE THROTTLE CONTROL MODEL

Plenum Exit Configuration

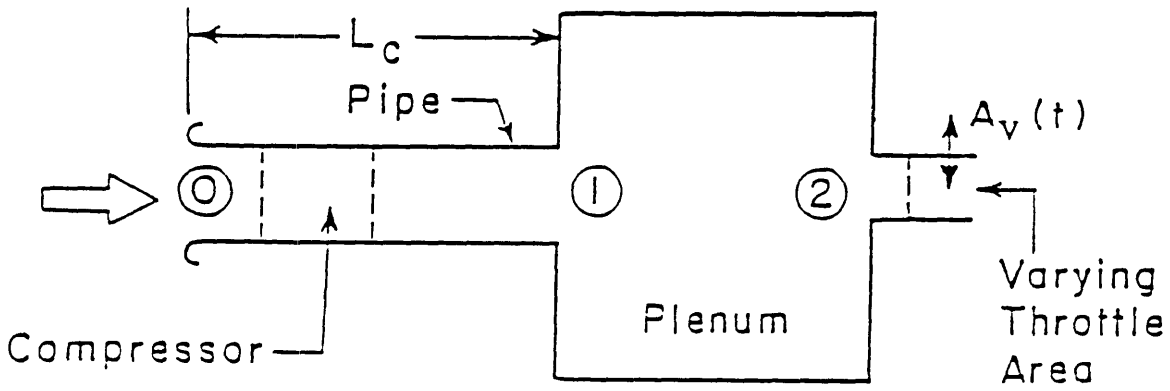

Figure 2.1 Model of Compression System with Plenum Exit Throttle Control

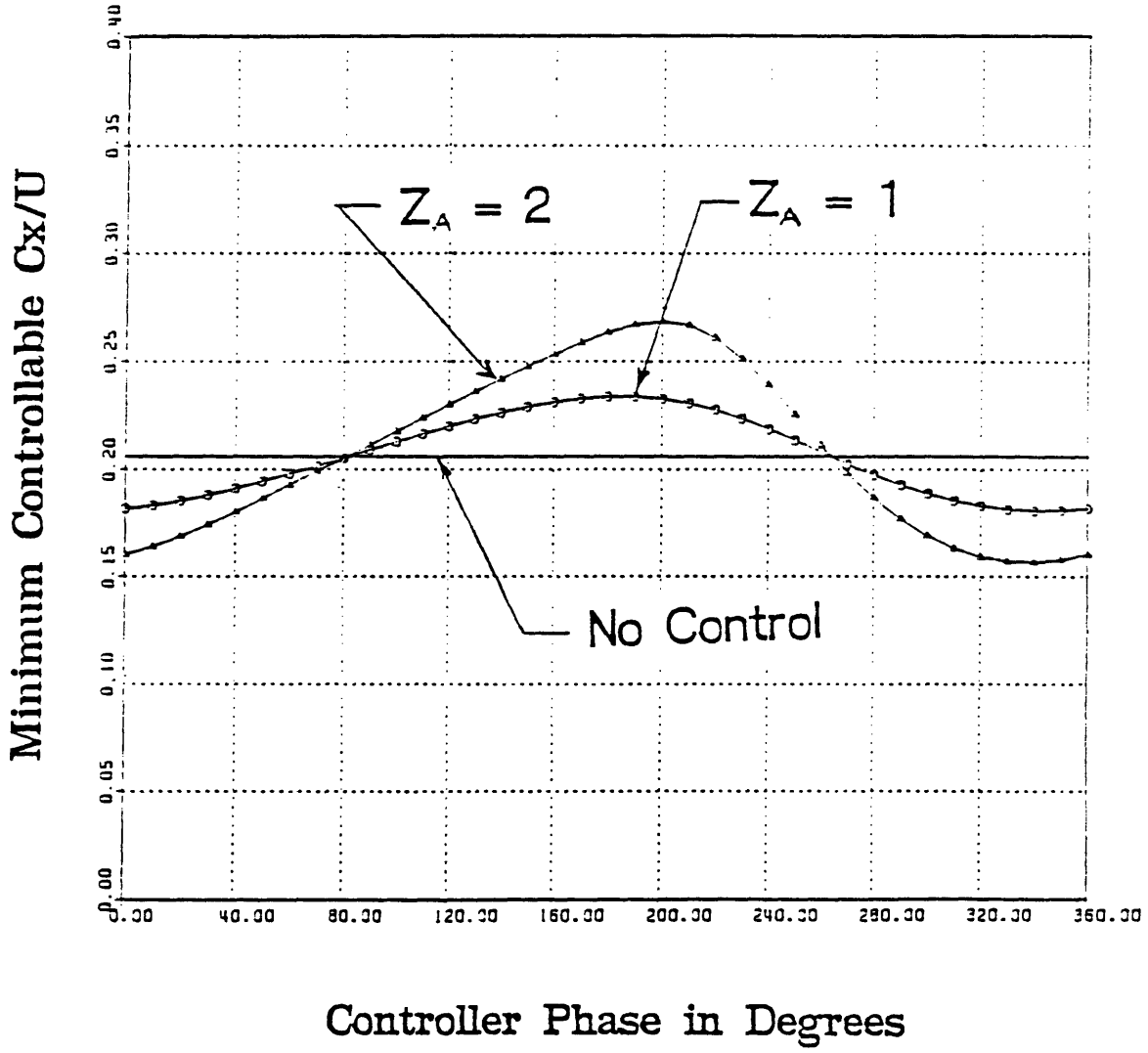

Figure 2.2 Minimum Controllable Flow Coefficient vs. Controller Phase (Chen) [1]. Magnitude of Controller Gain = z_A

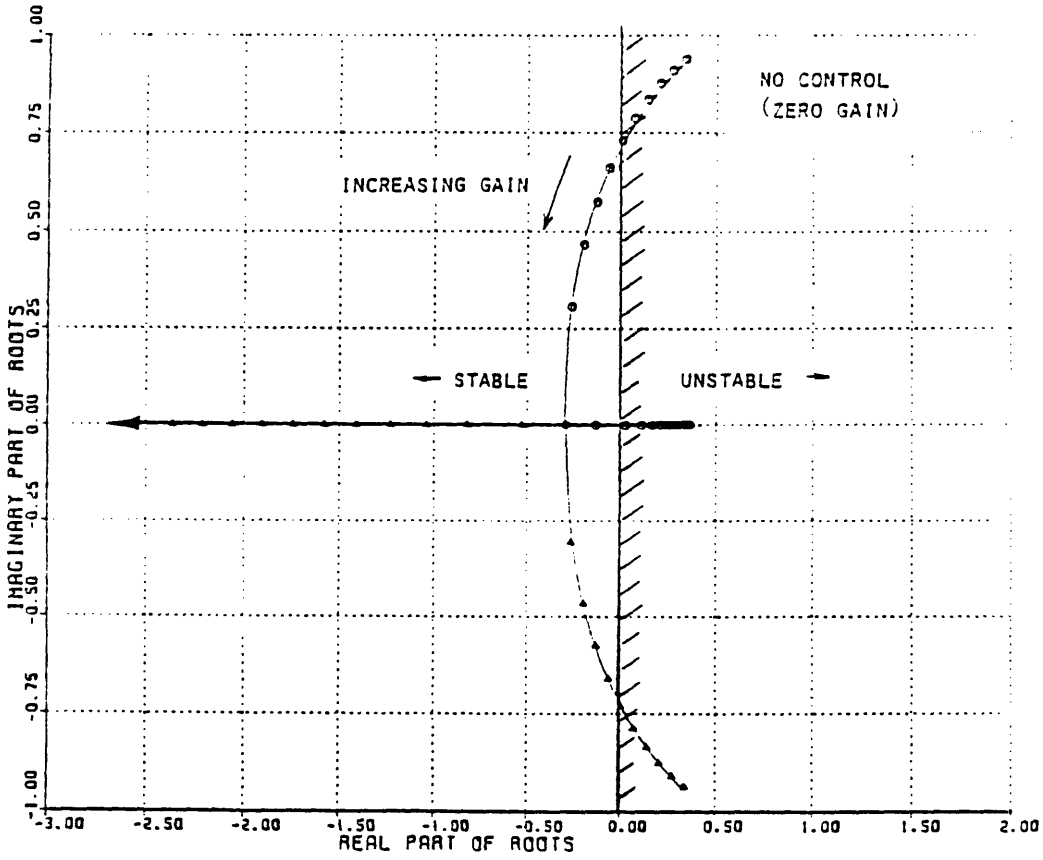

Figure 2.3 Root Locus for Controller at Zero Degrees Phase Shift
B = .61, Cubic Compressor Characteristic Assumed

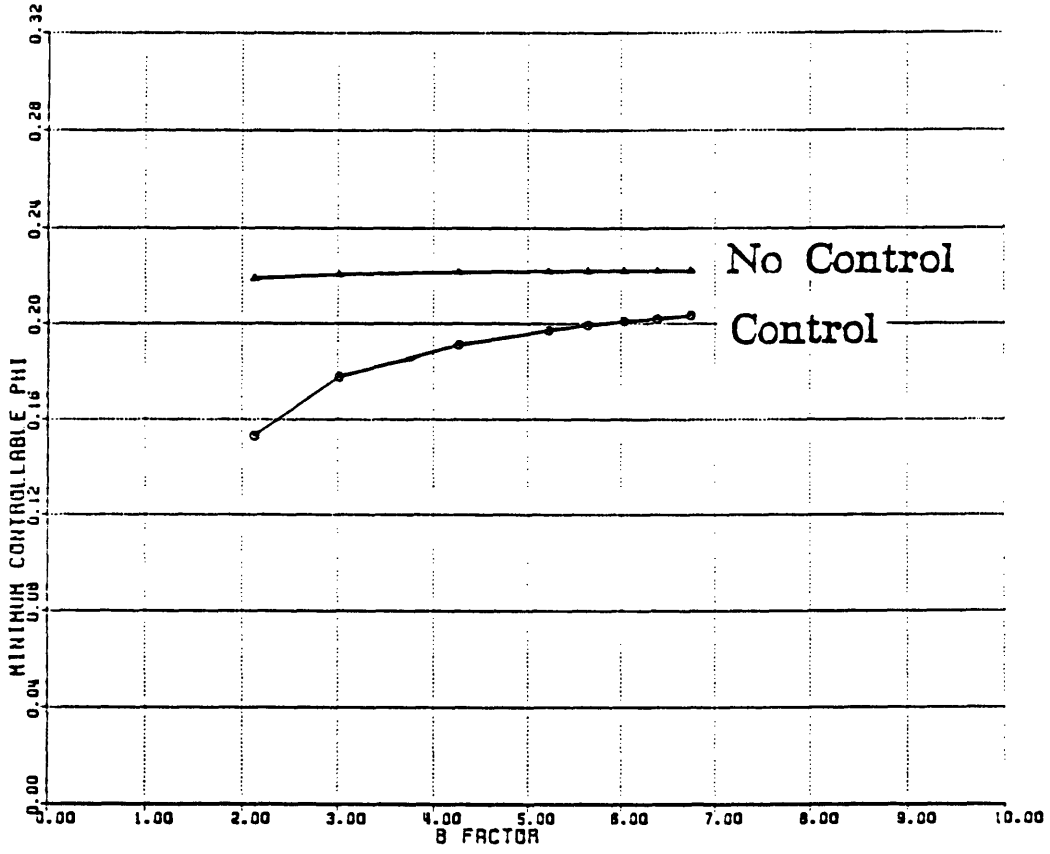

Figure 2.4 Minimum Controllable Flow Coefficient vs. B Parameter
Cubic Compressor Characteristic Assumed

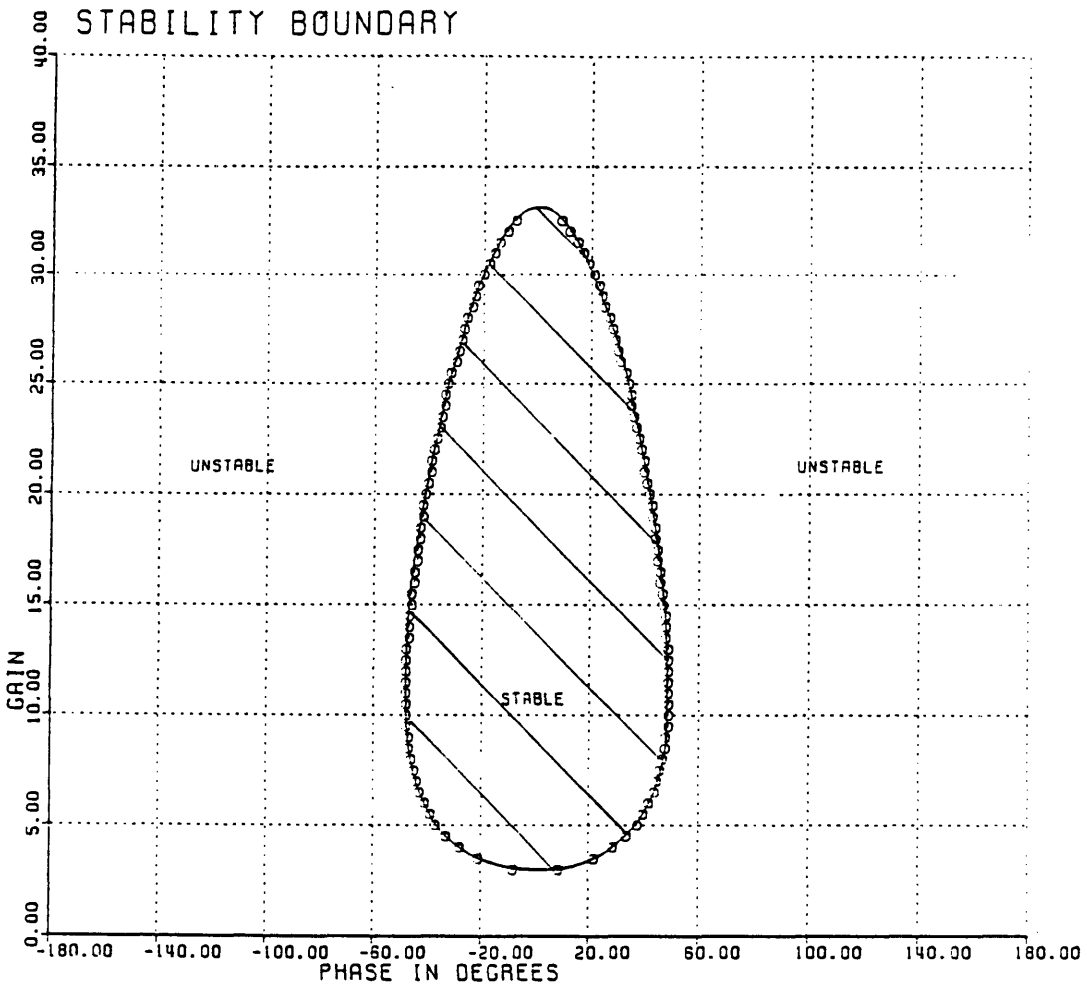

Figure 2.5 Stability Boundary in the Gain-Phase Plane
B .61, $\phi = .12$, $\psi = 1.87$, $\hat{T}_c = 1$

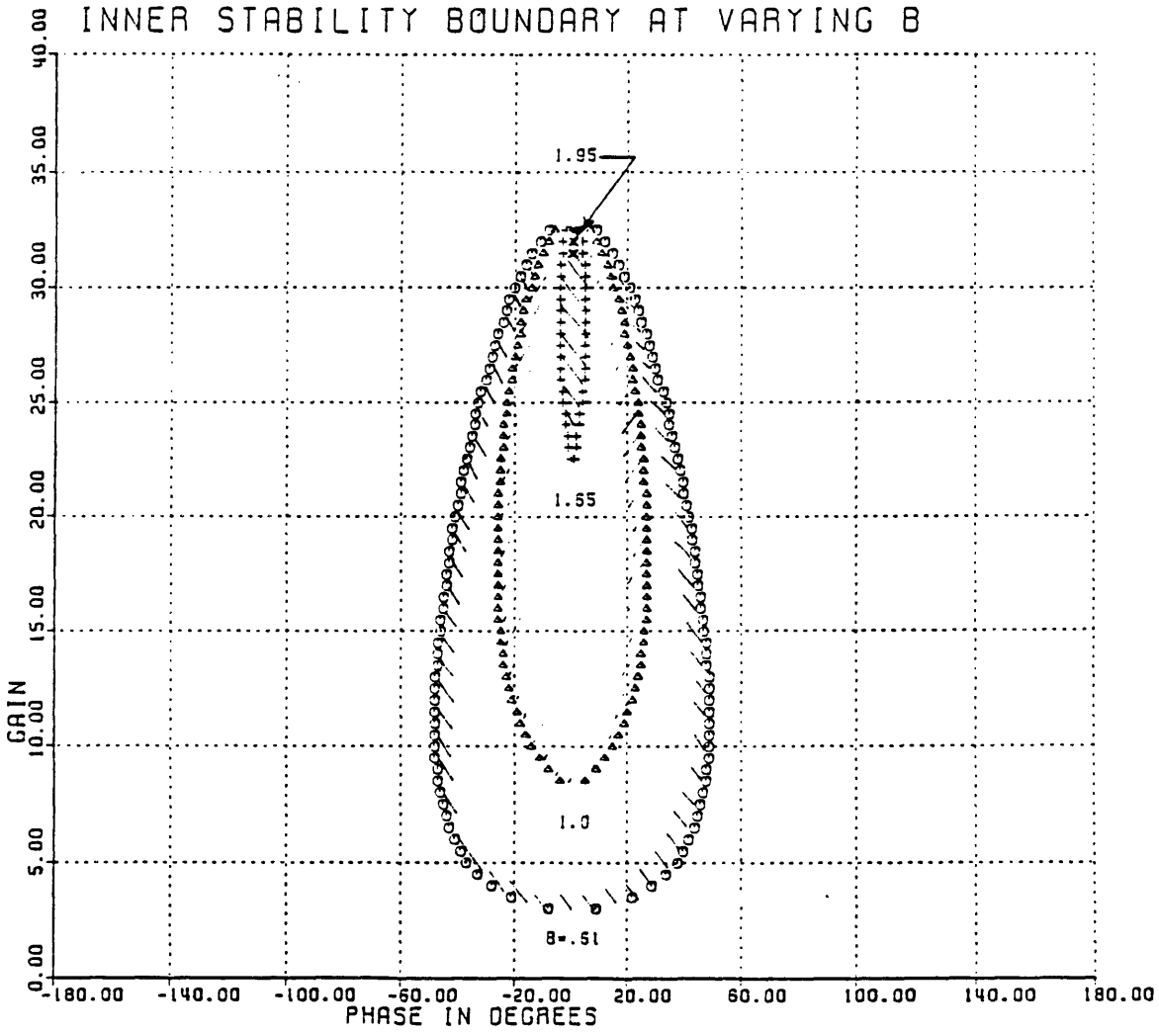

Figure 2.6 Variation of Stability Boundary with B Parameter
$\phi = .12, \psi = 1.87, \hat{T}_C = 1$

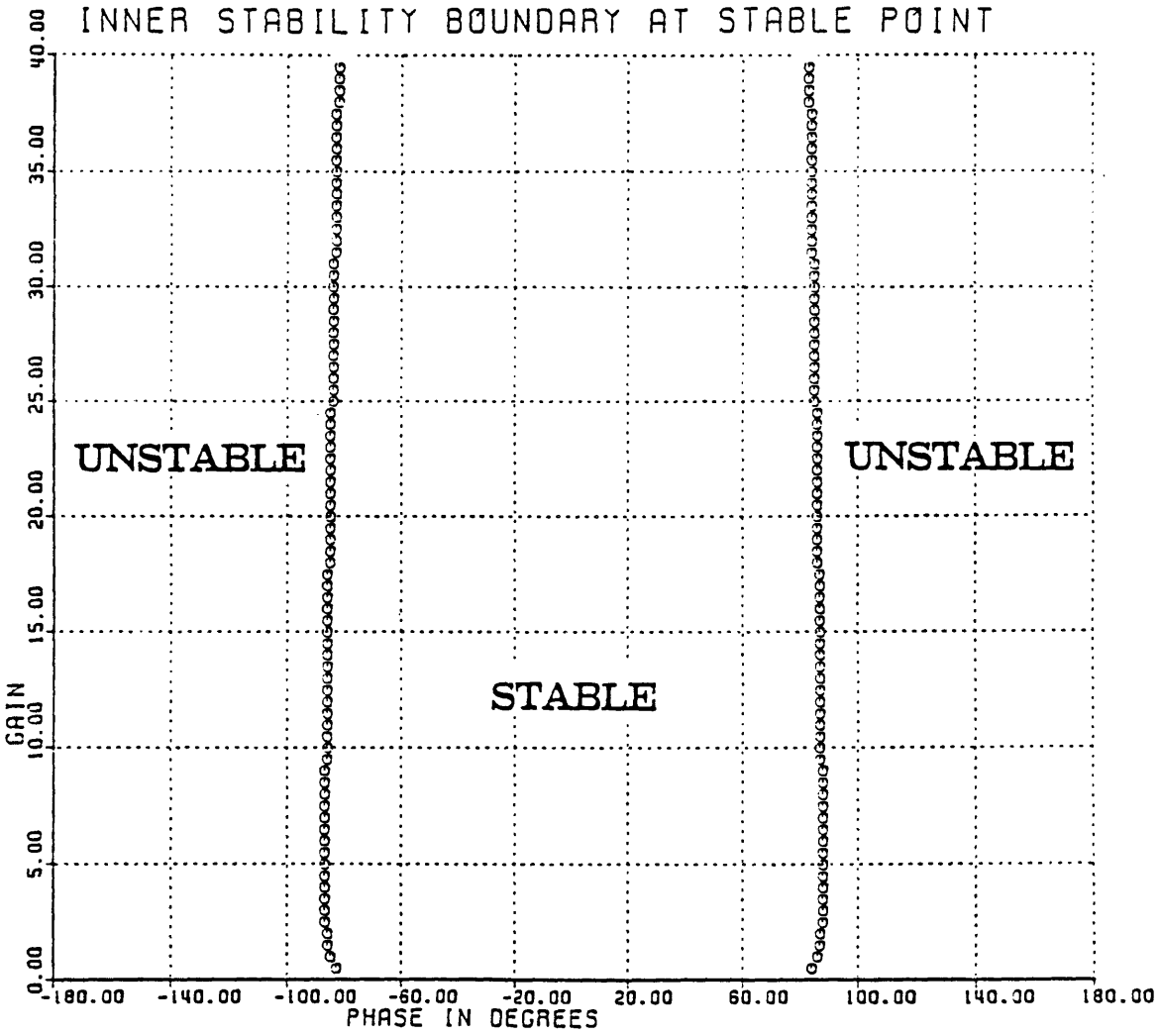

Figure 2.7 Stability Boundary at Nominally Stable Operating Point $\phi = .12, \psi = 1.87, \hat{T}_c = .1$

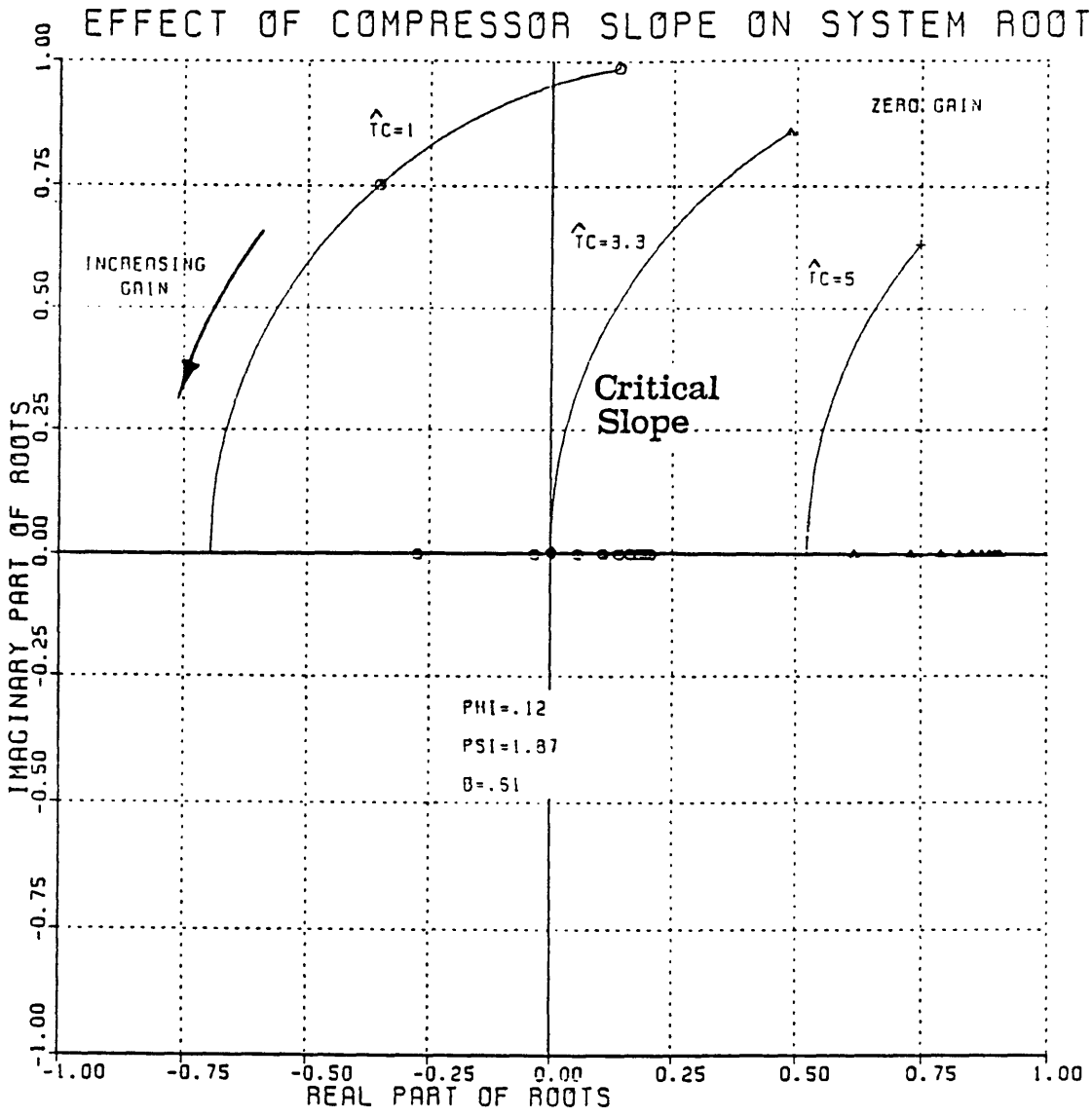

Figure 2.8 Effect of Compressor Slope on System Poles

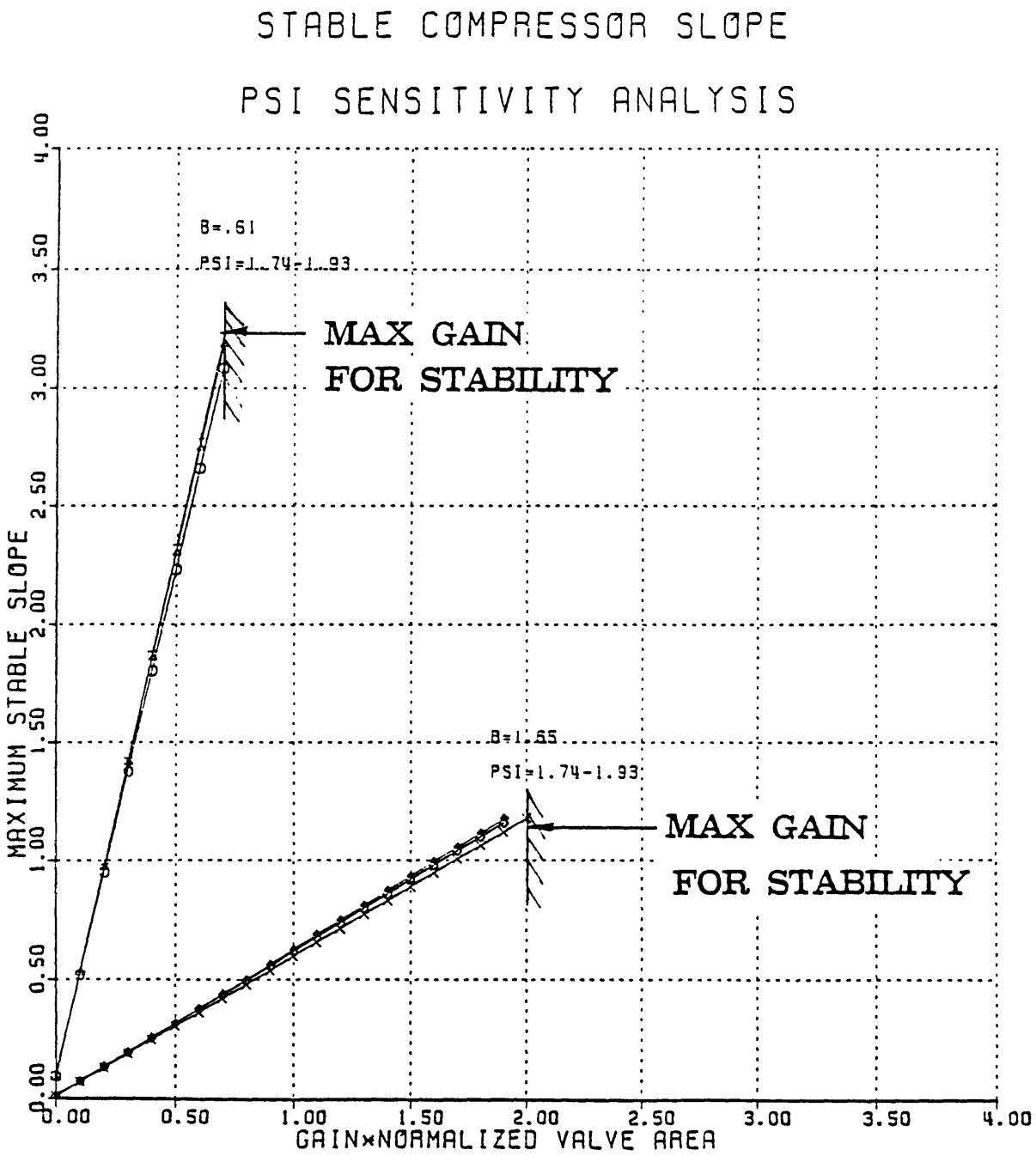

Figure 2.9 Slope Sensitivity Analysis for $\phi = .12$, ψ Varying from 1.74 to 1.93 Controller Gain = Magnitude of z_A x (A_v/A_{in})

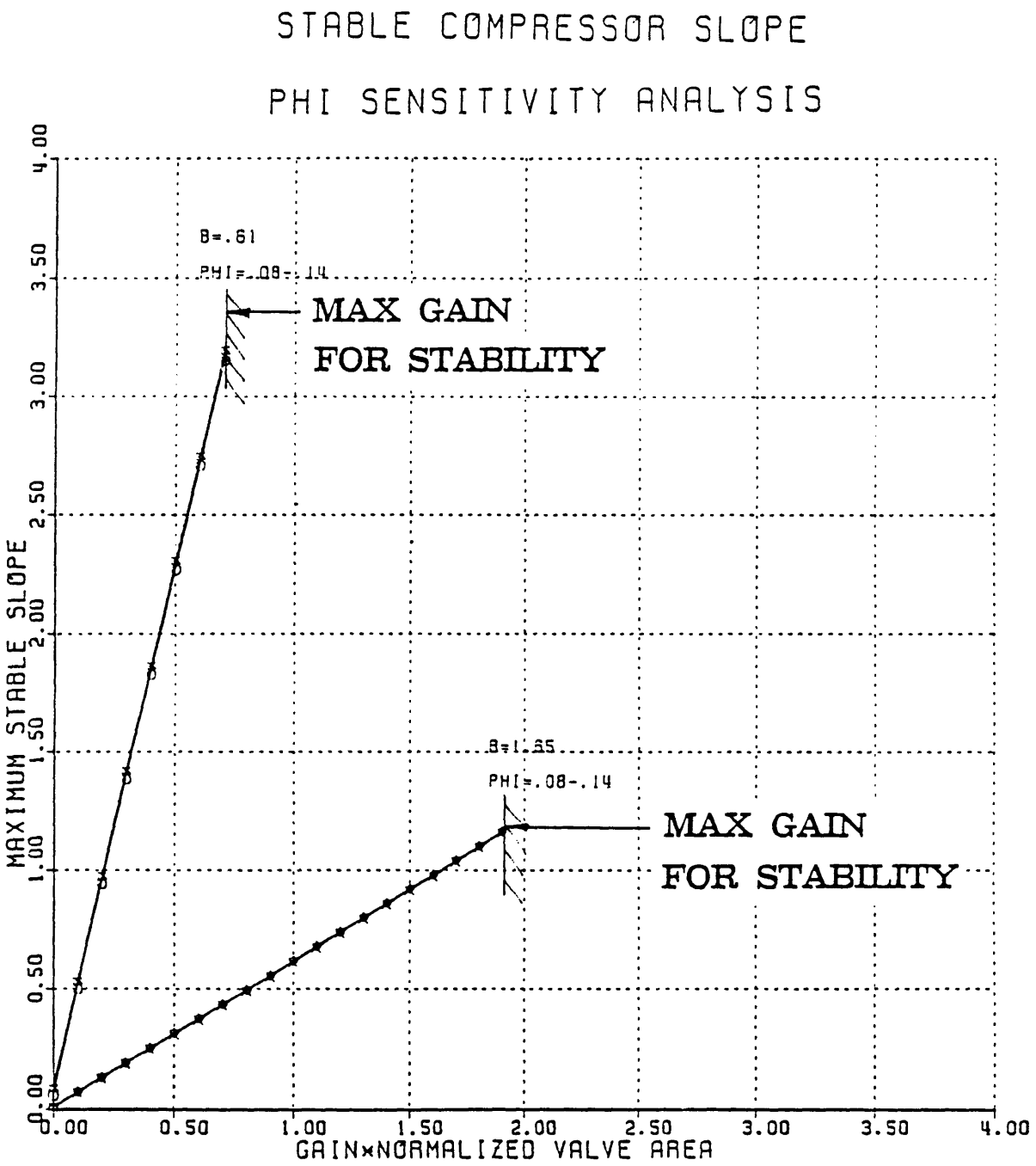

Figure 2.10 Slope Sensitivity Analysis for ψ = 1.87, ϕ Varying from .08 to .14
Controller Gain = Magnitude of z_A x (A_v/A_{in})

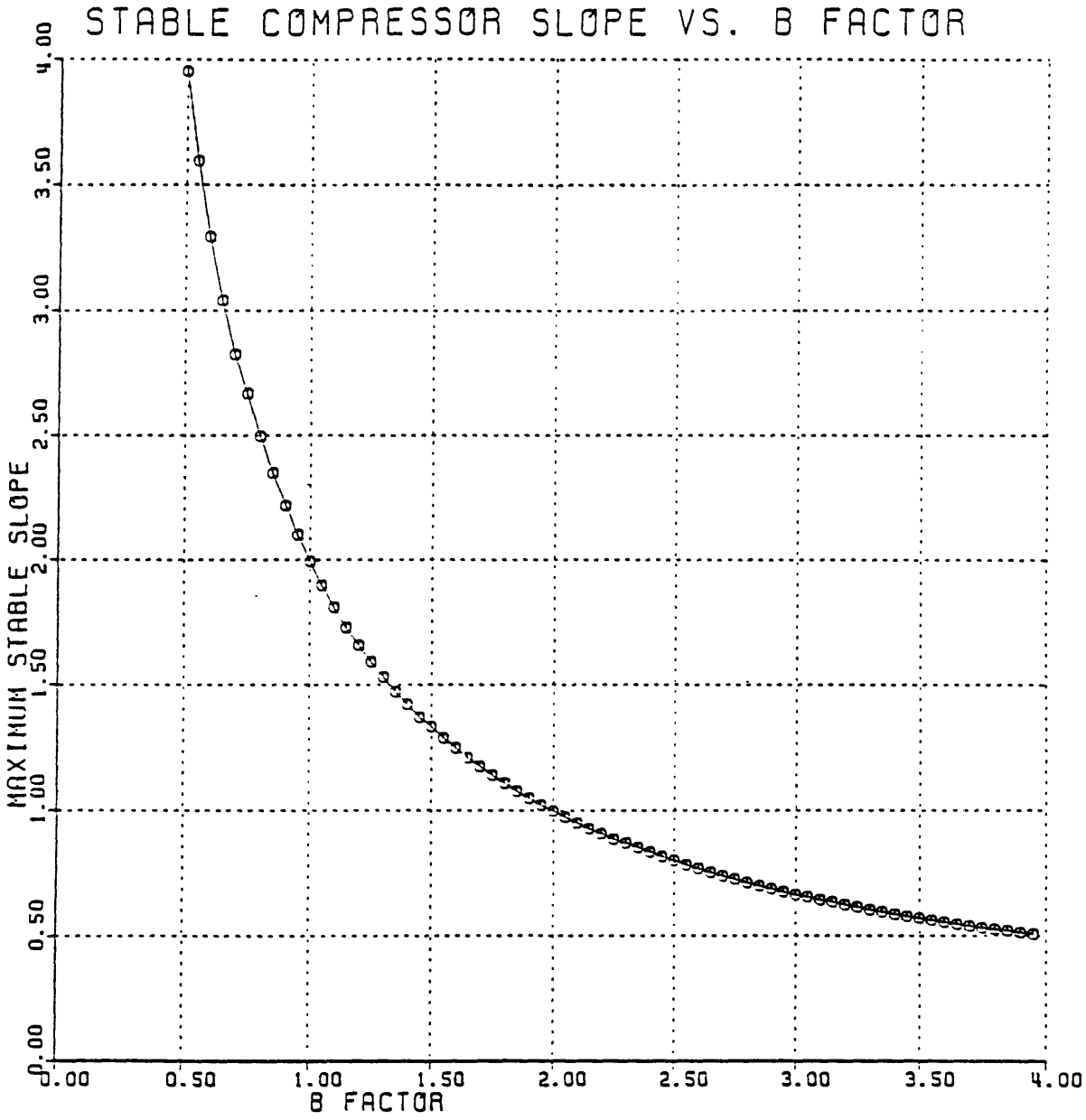

Figure 2.11 Maximum Tolerable Compressor Characteristic Slope vs. B Parameter

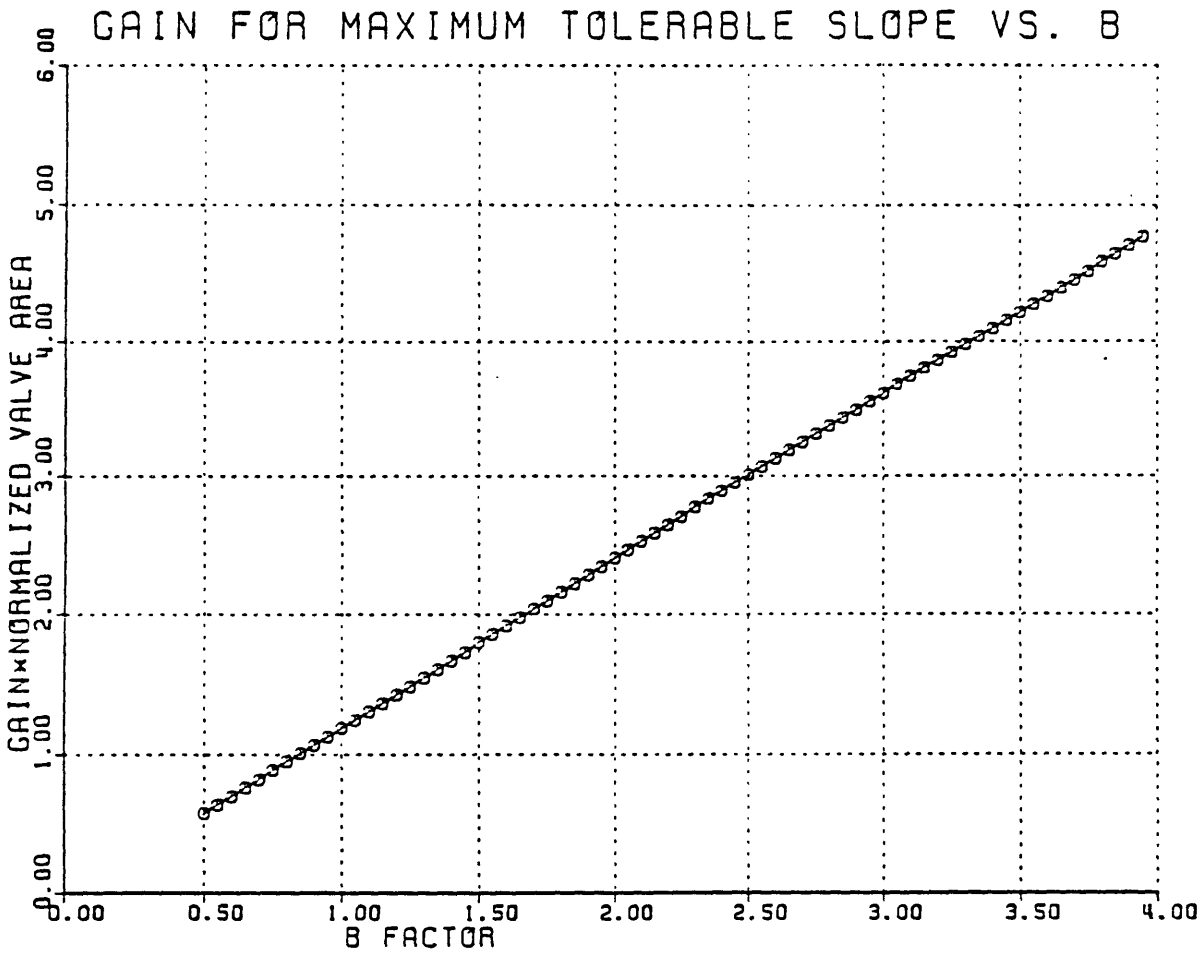

Figure 2.12 Required Controller Gain for Maximum Tolerable Compressor Characteristic Slope vs. B Parameter
Controller Gain = Magnitude of z_A x (A_v/A_{in})

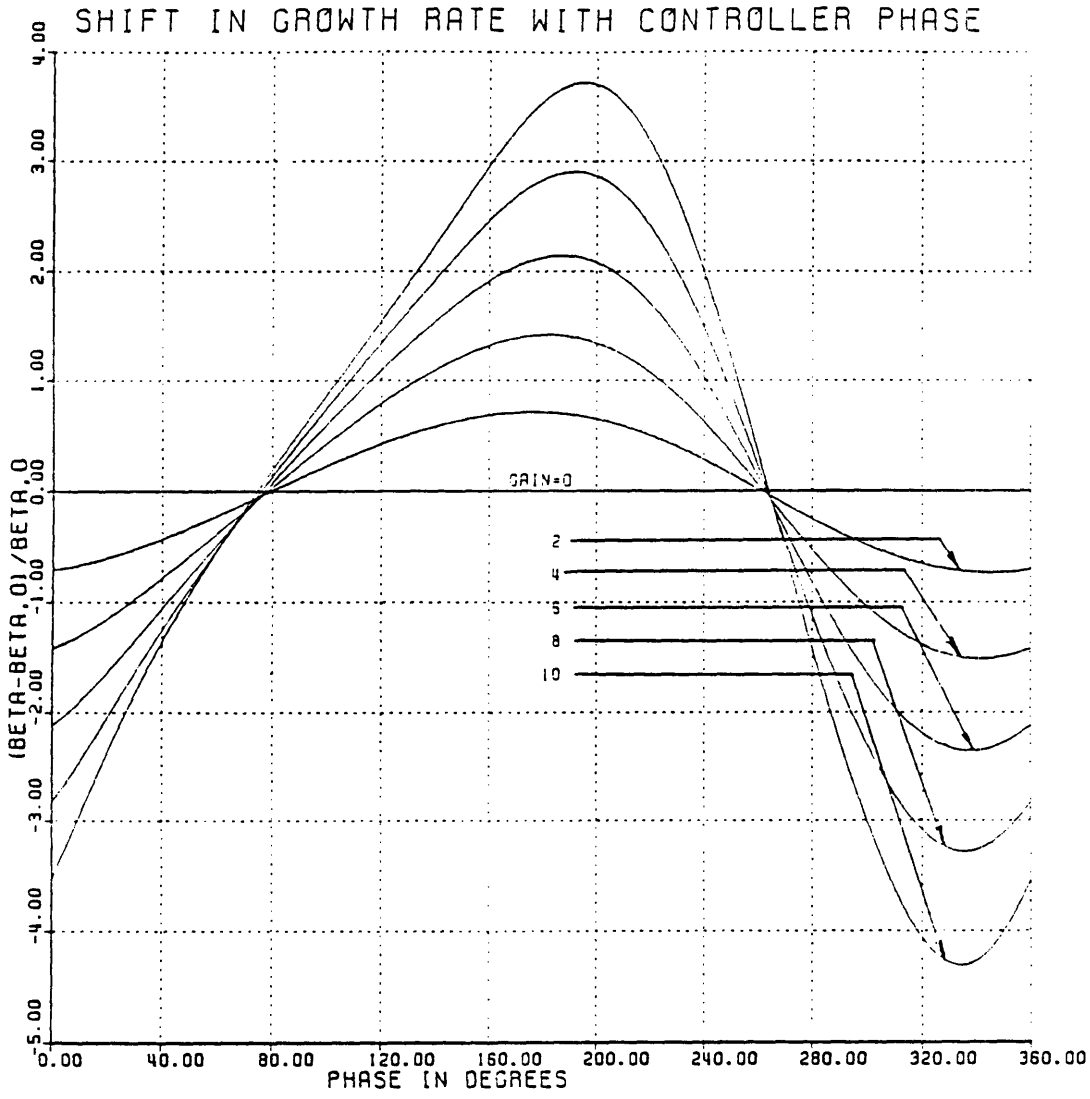

Figure 2.13 Variation of Perturbation Growth Rate with Controller Phase B = .61, Cubic Characteristic Assumed, Gain = Magnitude of z_A $\phi = .12$

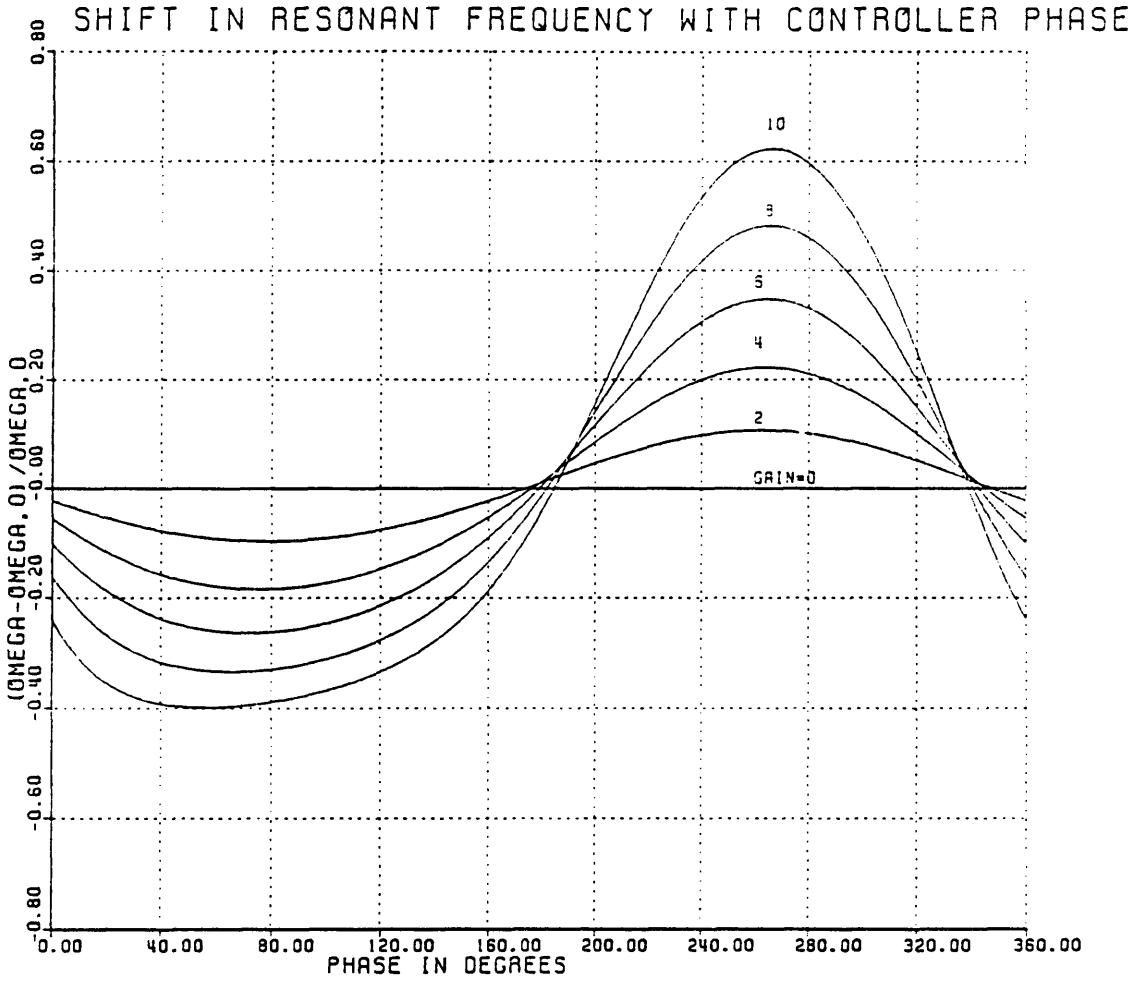

Figure 2.14 Variation of System Resonant Frequency with Controller Phase
B = .61, Cubic Characteristic Assumed, Gain = Magnitude of z_A
$\phi = .12$

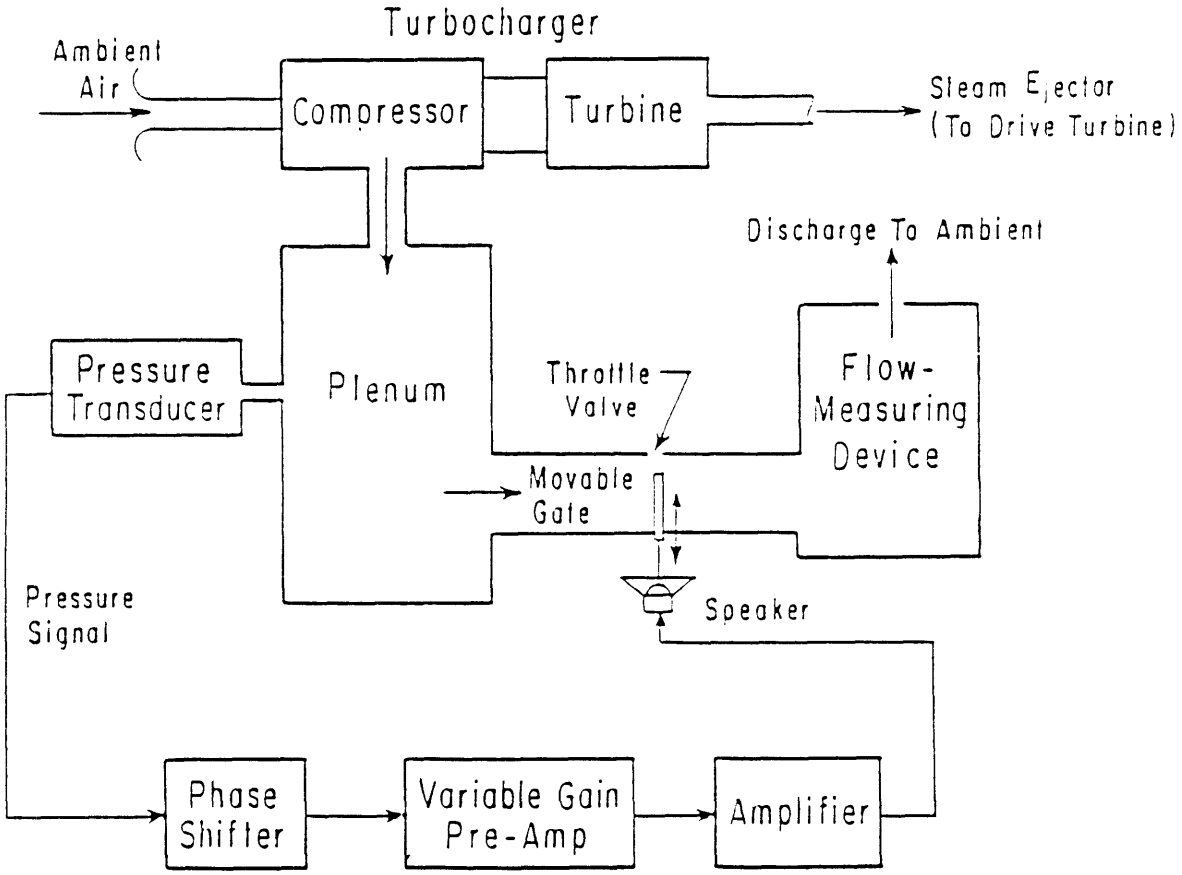

Figure 3.1 Low Speed Test Rig Schematic with Analog Control Loop

COMPRESSOR OPERATING CHARACTERISTICS

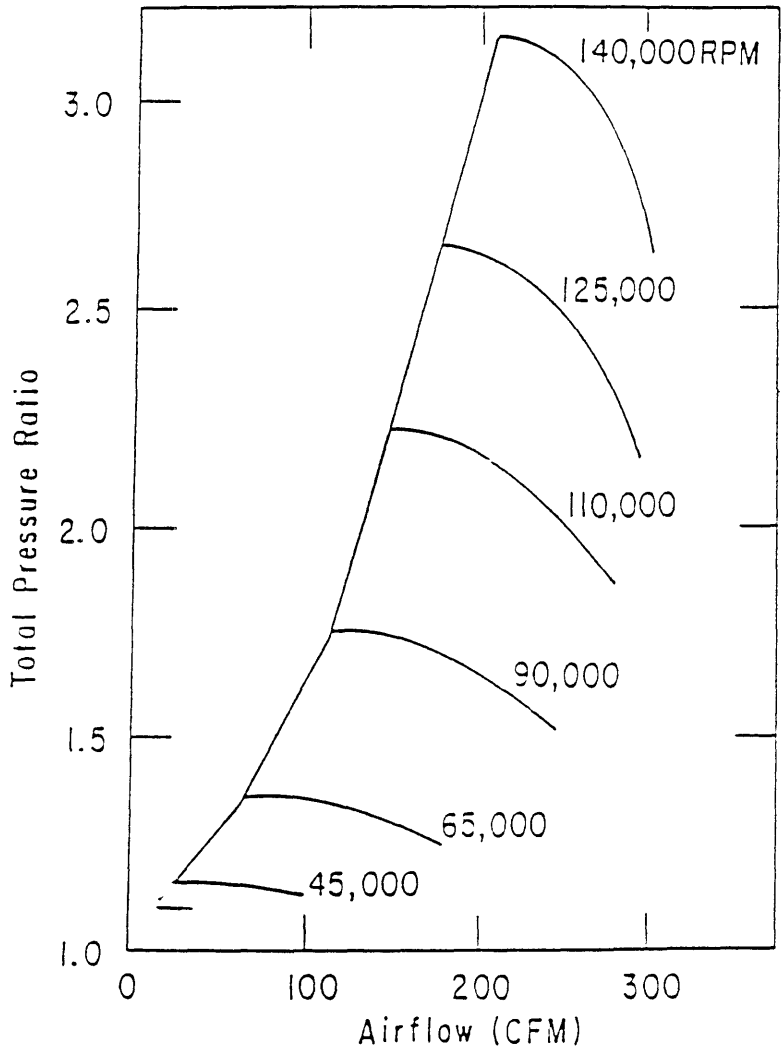

Figure 3.2 Holset H1D Turbocharger Compressor Map

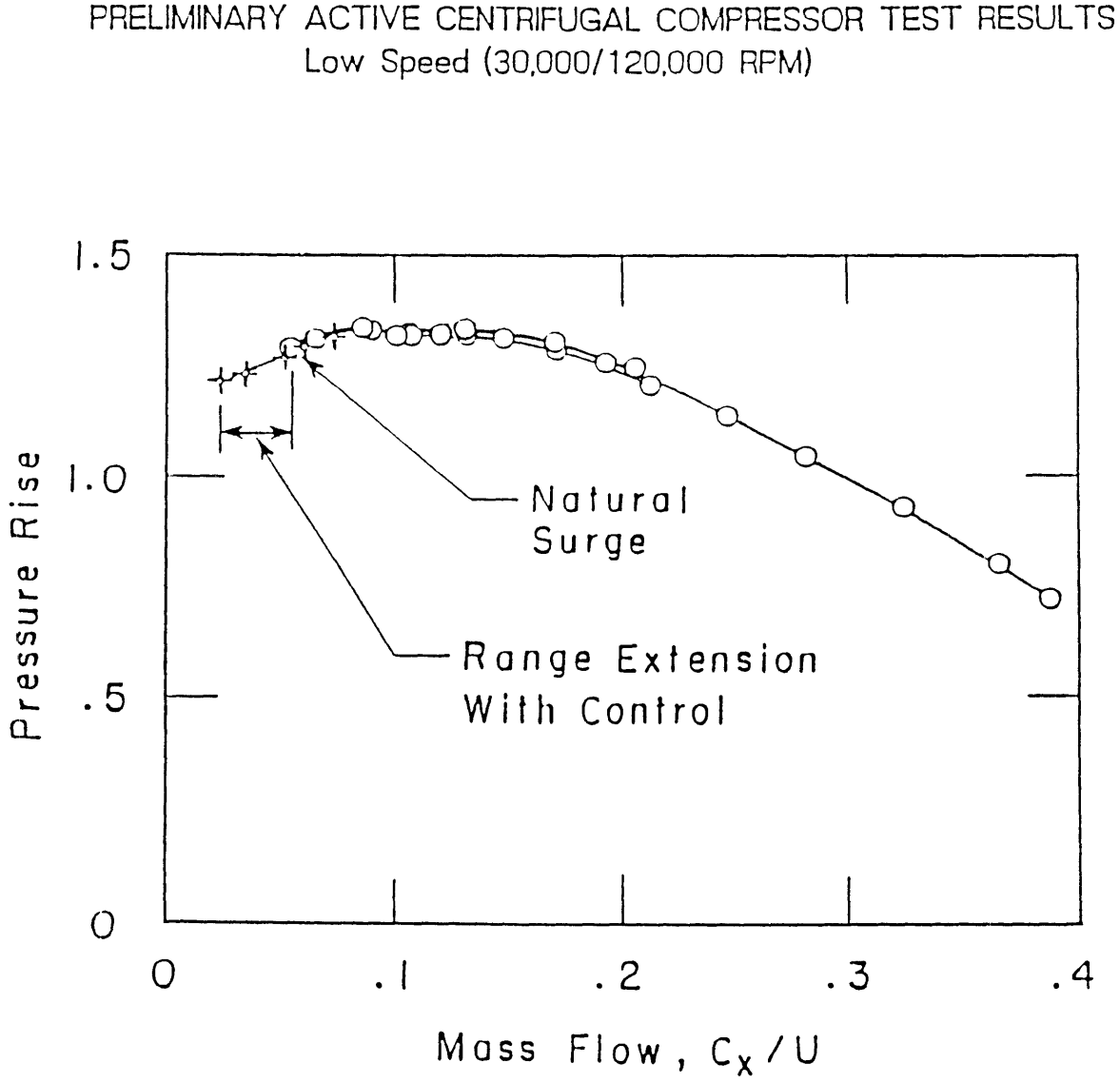

Figure 3.3 Surge Line Extension at Low Speed with Control

ACTIVELY STABILIZED CENTRIFUGAL COMPRESSOR

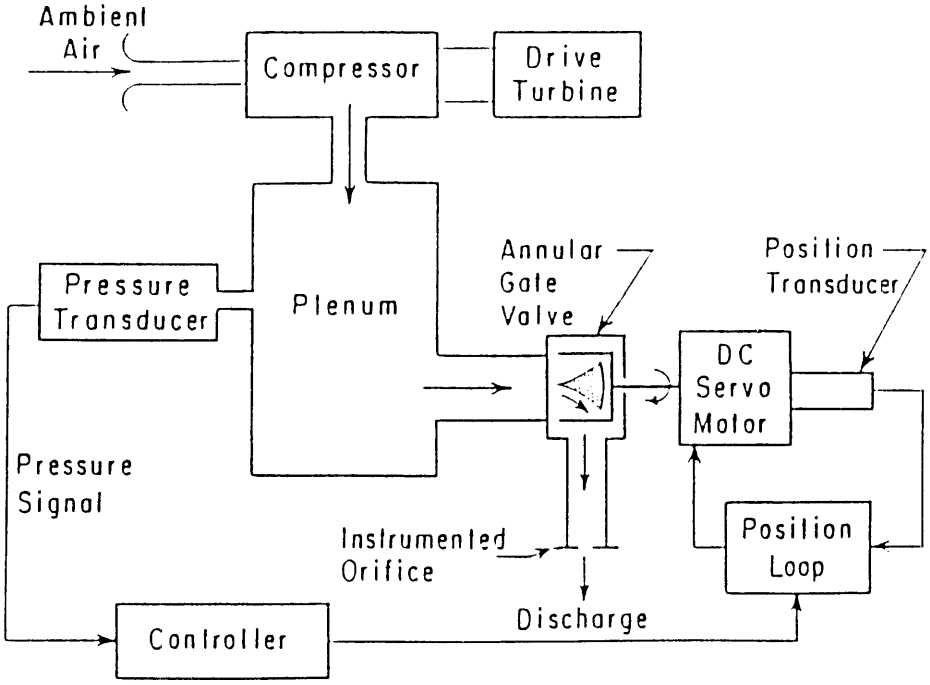

Figure 4.1 Flowpath for High Speed Test Facility

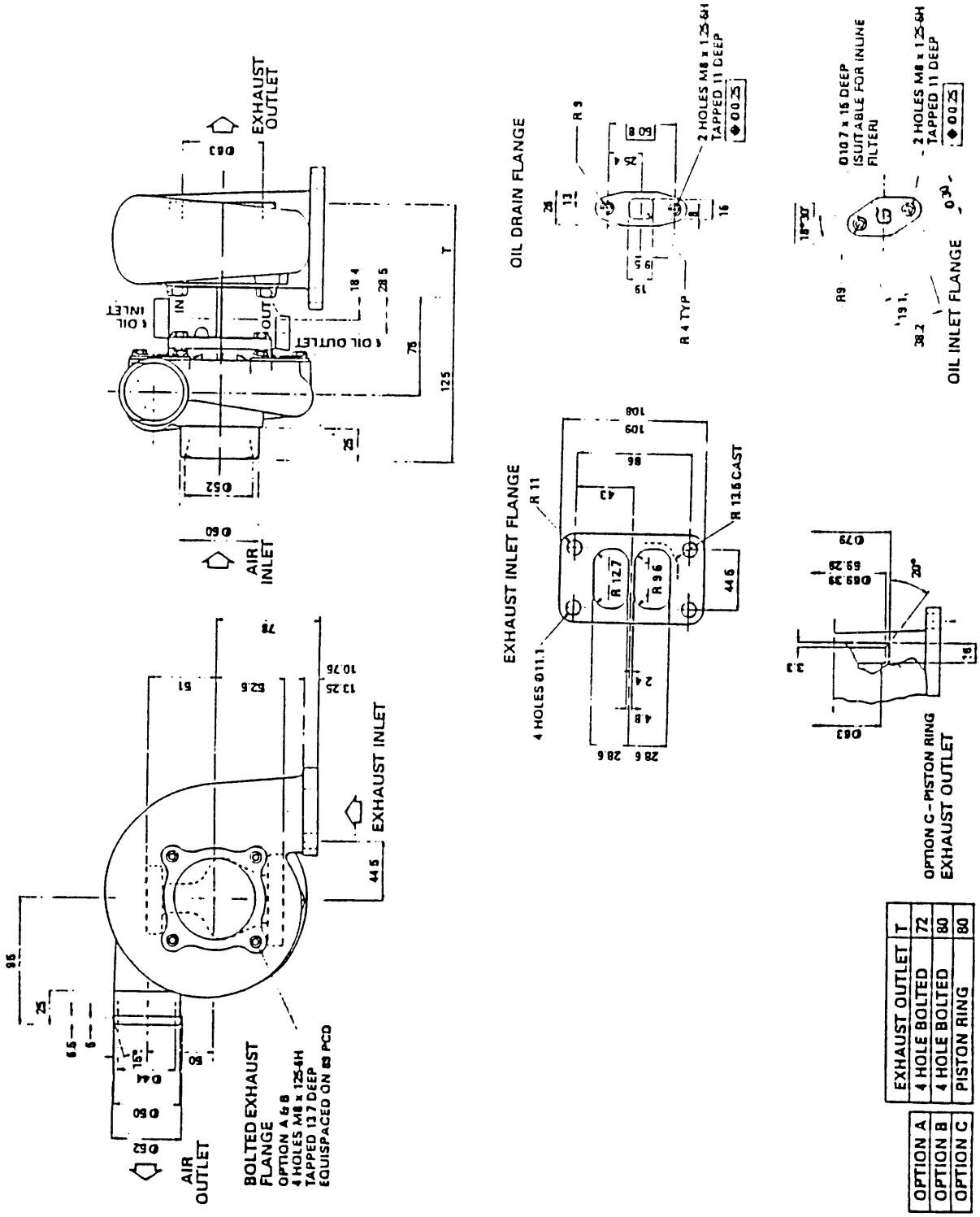

Figure 4.2 External Dimensions of Holset H1D Turbocharger, Page 1 of 2

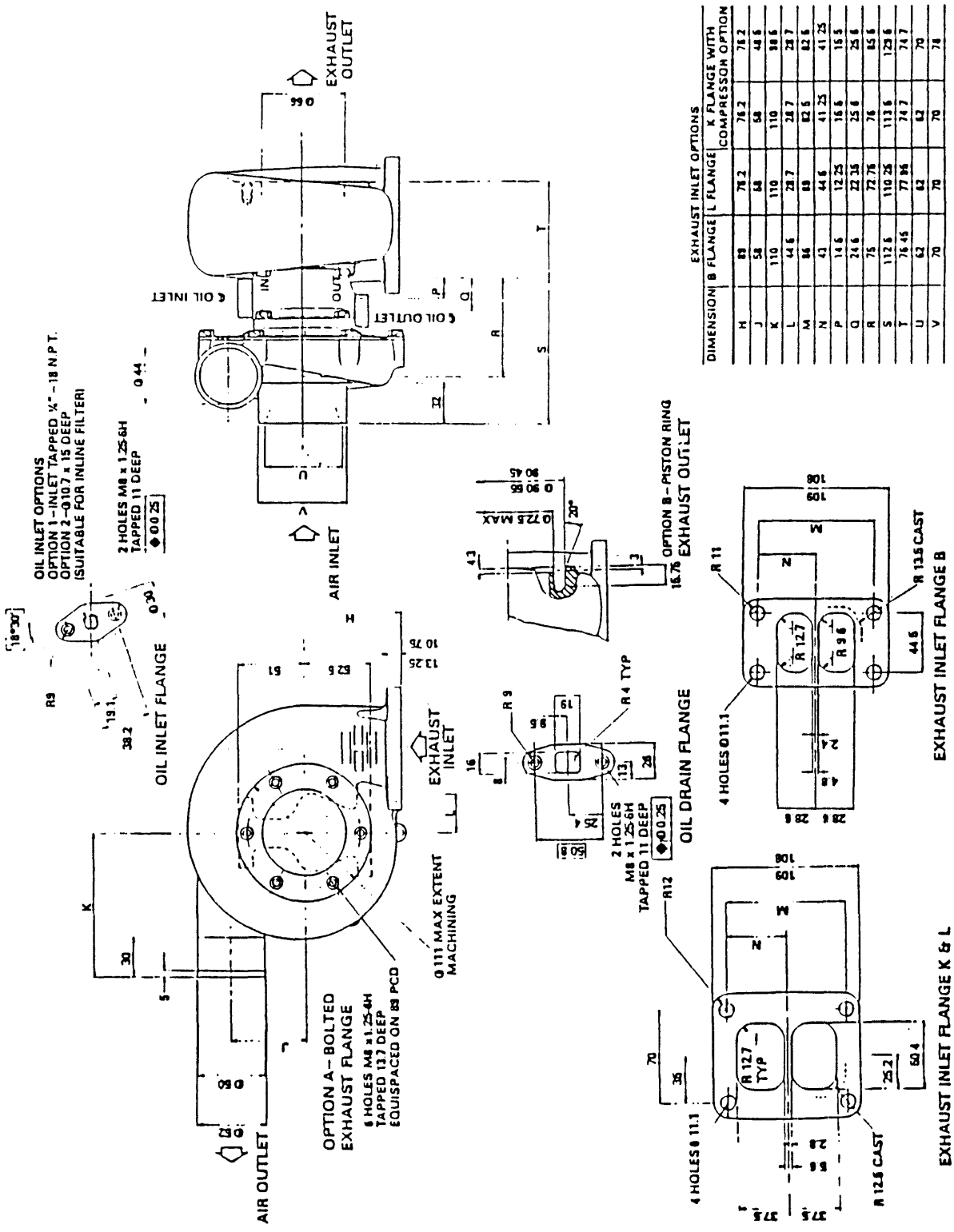

Figure 4.3 External Dimensions of Holset H1D Turbocharger, Page 2 of 2

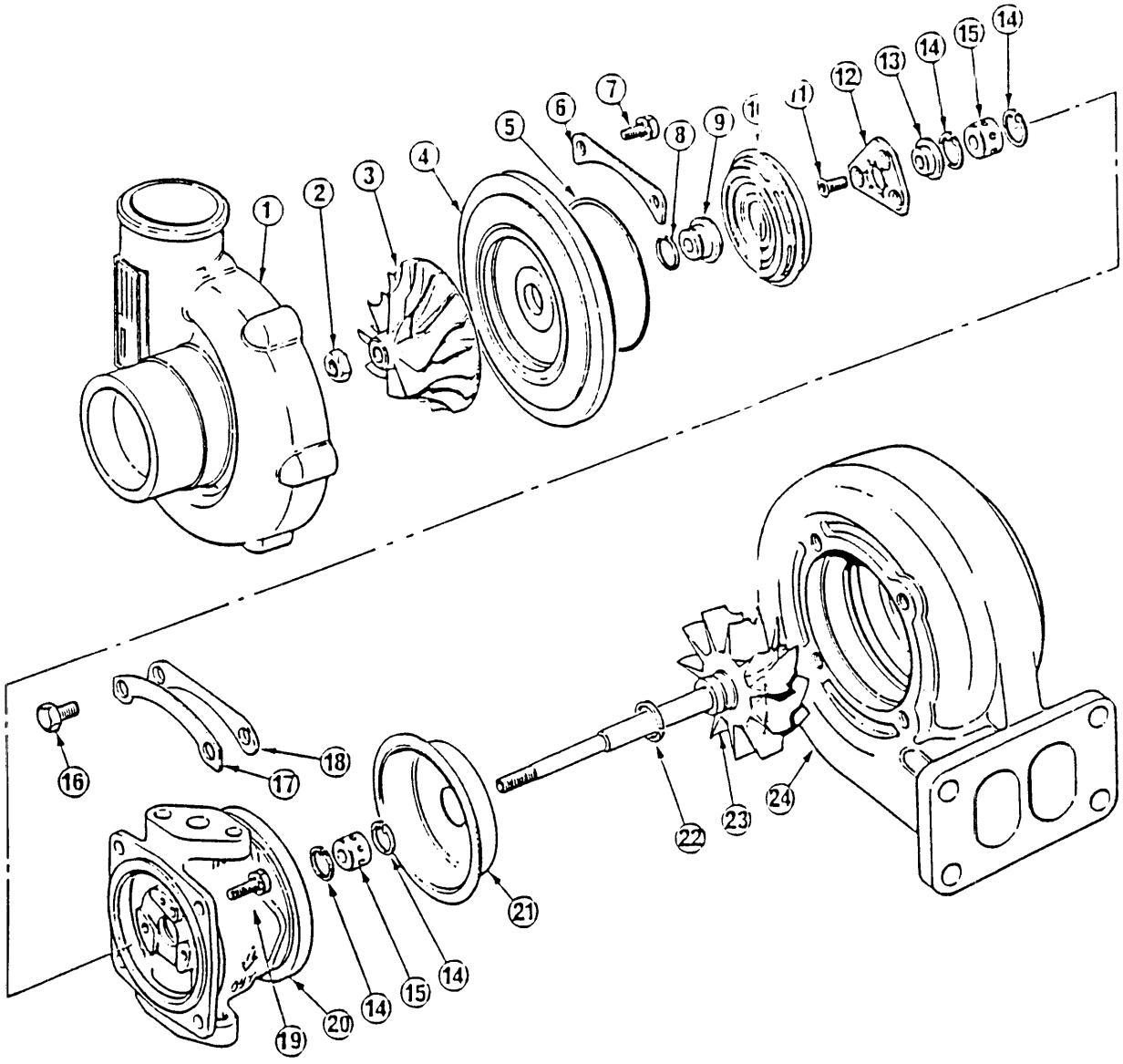

Figure 4.4 Exploded View of Holset H1D Turbocharger

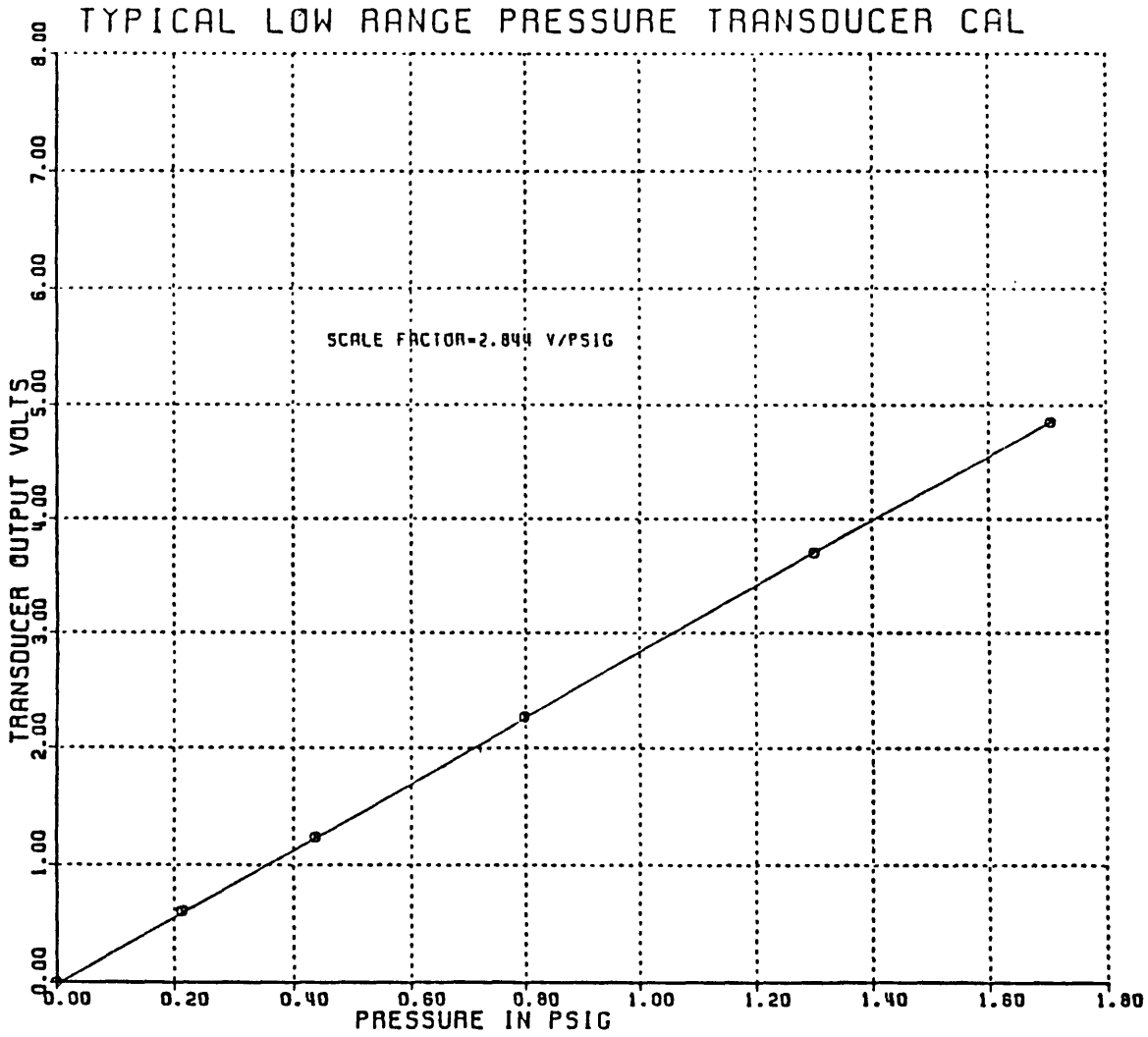

Figure 4.5 Typical Low Range Druck Pressure Transducer Calibration

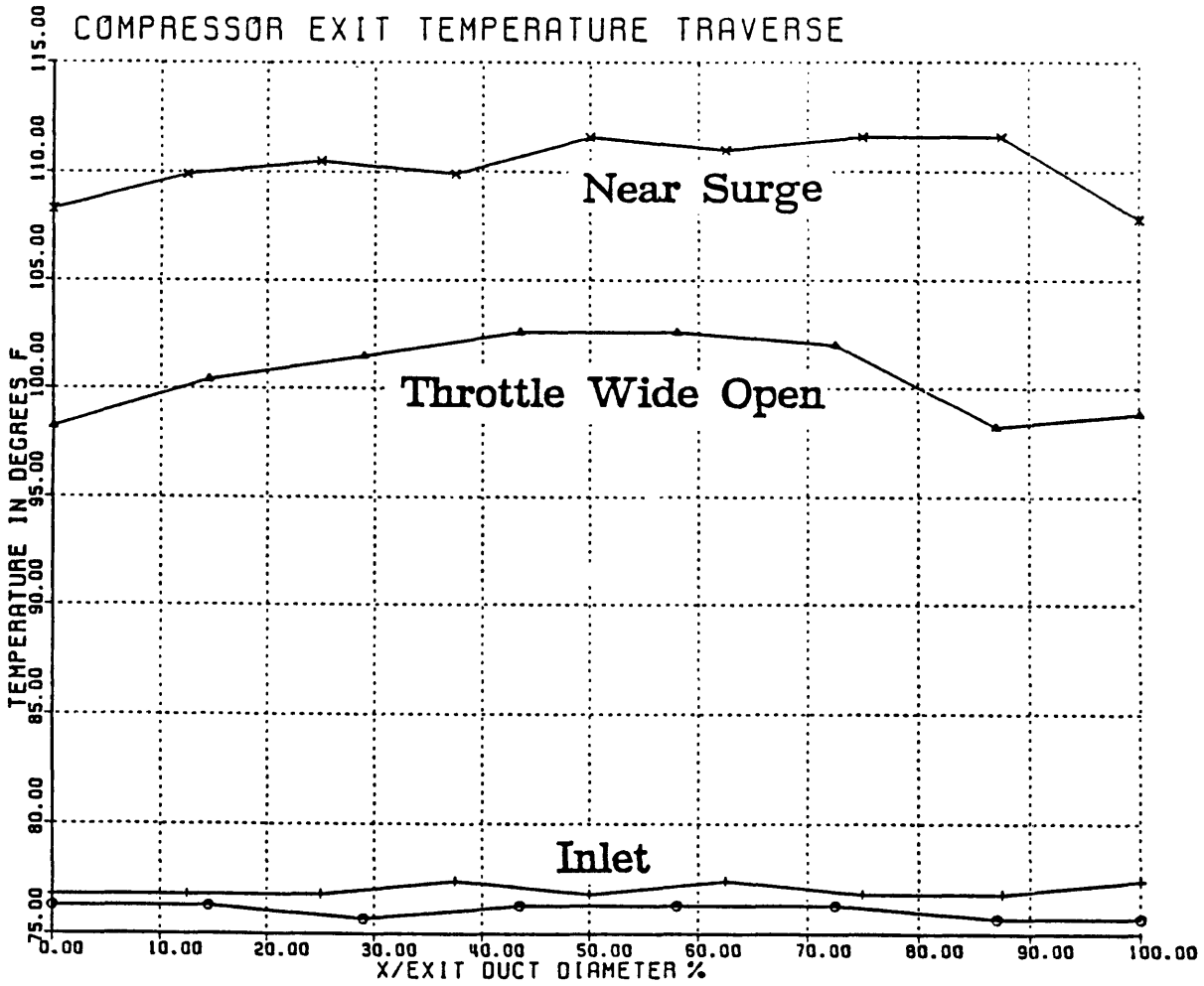

Figure 4.6 Radial Total Temperature Profile in Compressor Exit Duct

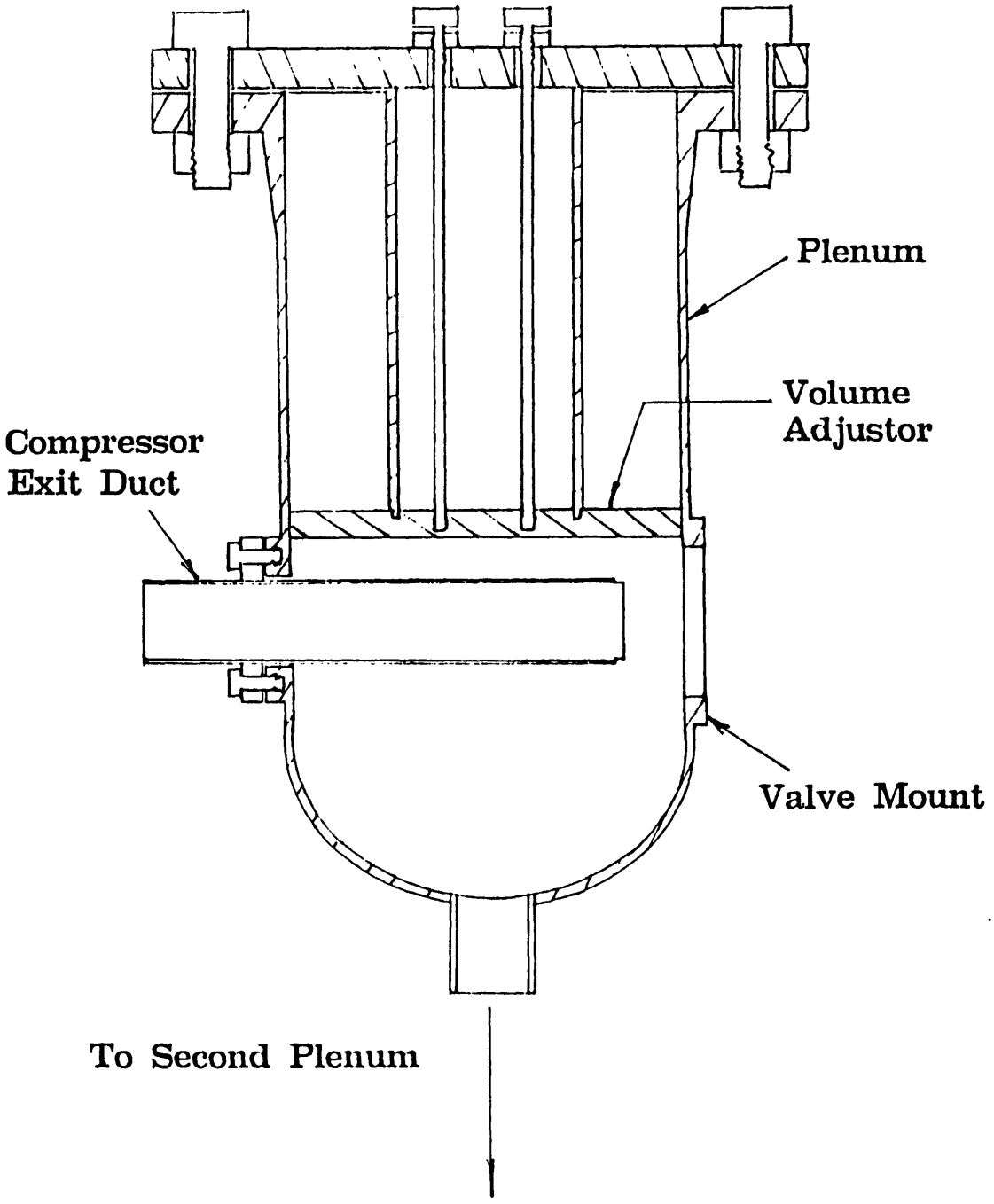

Figure 4.7 Cross-Sectional View of Main Plenum with Volume Adjustor

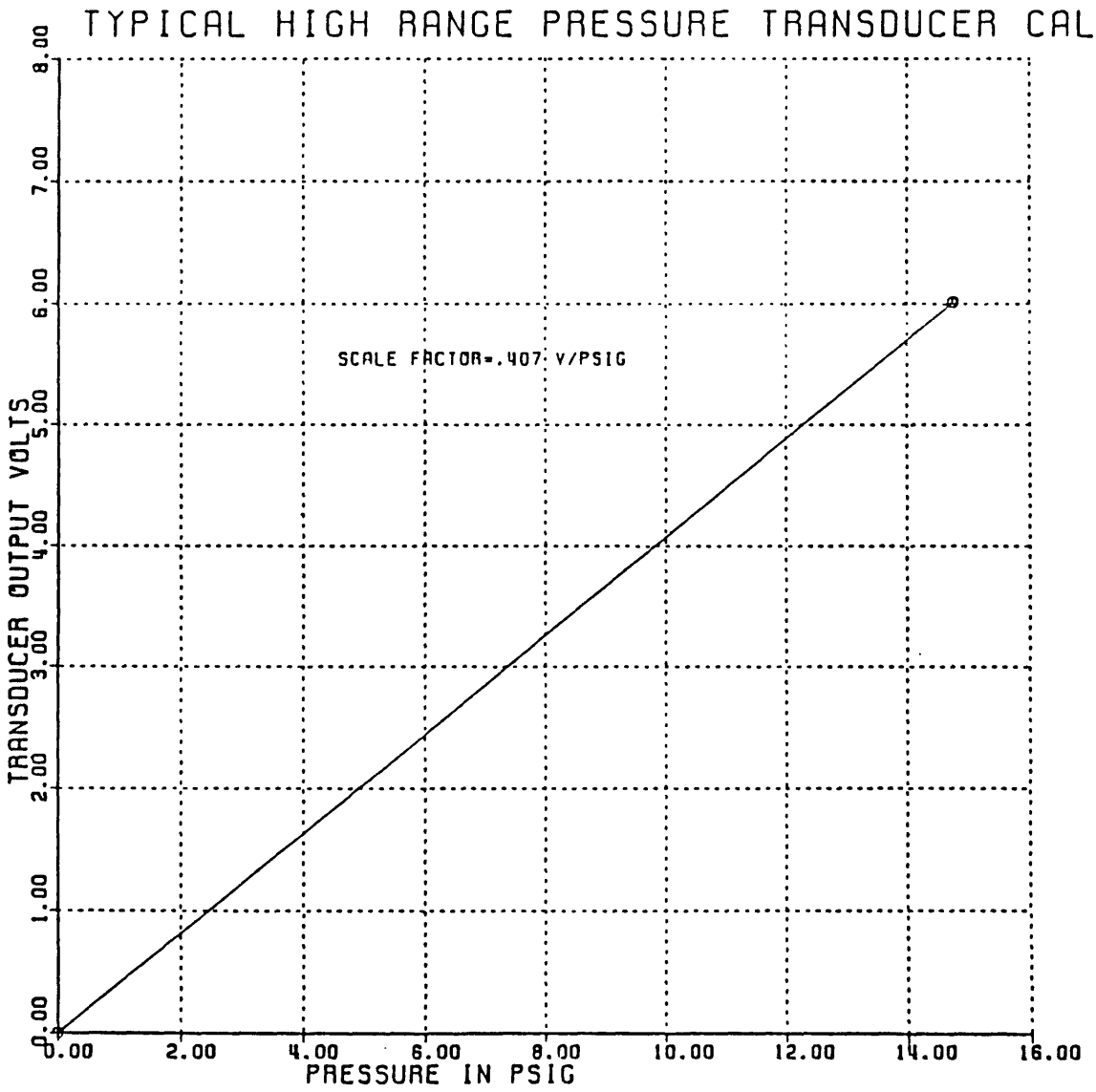

Figure 4.8 Typical High Range Druck Pressure Transducer Calibration

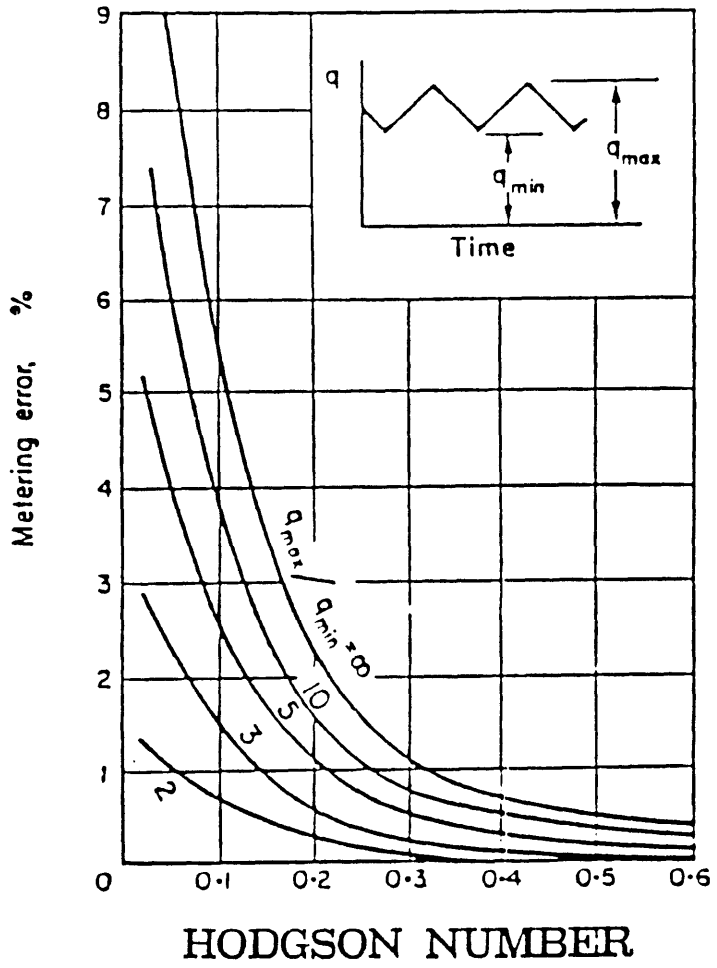

Figure 4.9 Error in Measurement of Flowrate in Pulsating Flow vs. Hodgson Number [12]
q = Actual Mass Flow

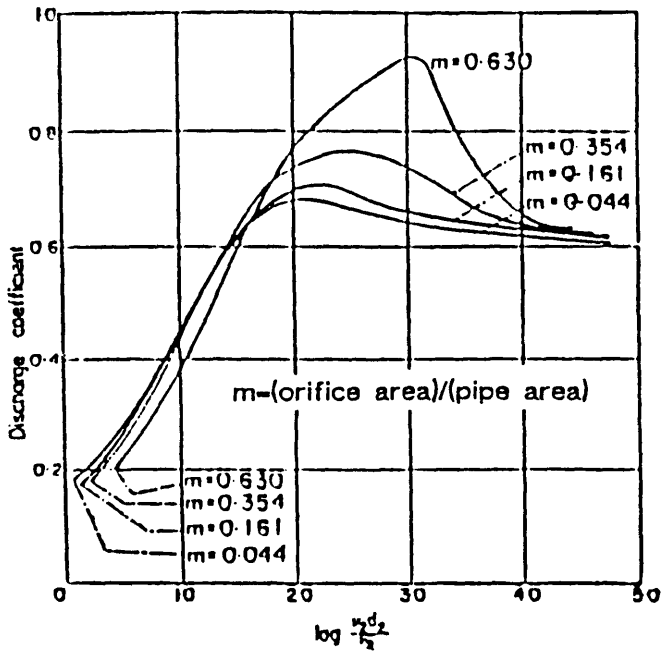

Figure 4.10(b) Predicted c_d vs. Reynolds Number [12]
Reynolds Number Based on Orifice Diameter

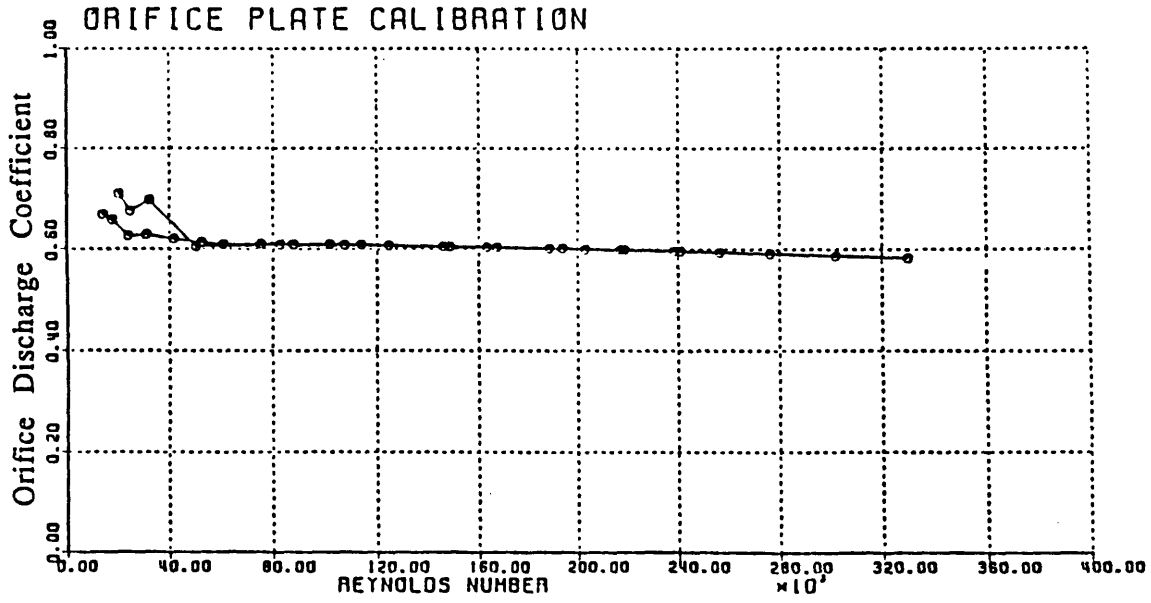

Figure 4.10(a) Orifice Discharge Coefficient Calibration, Experimental c_d vs. Reynolds Number
Reynolds Number Based on Orifice Diameter

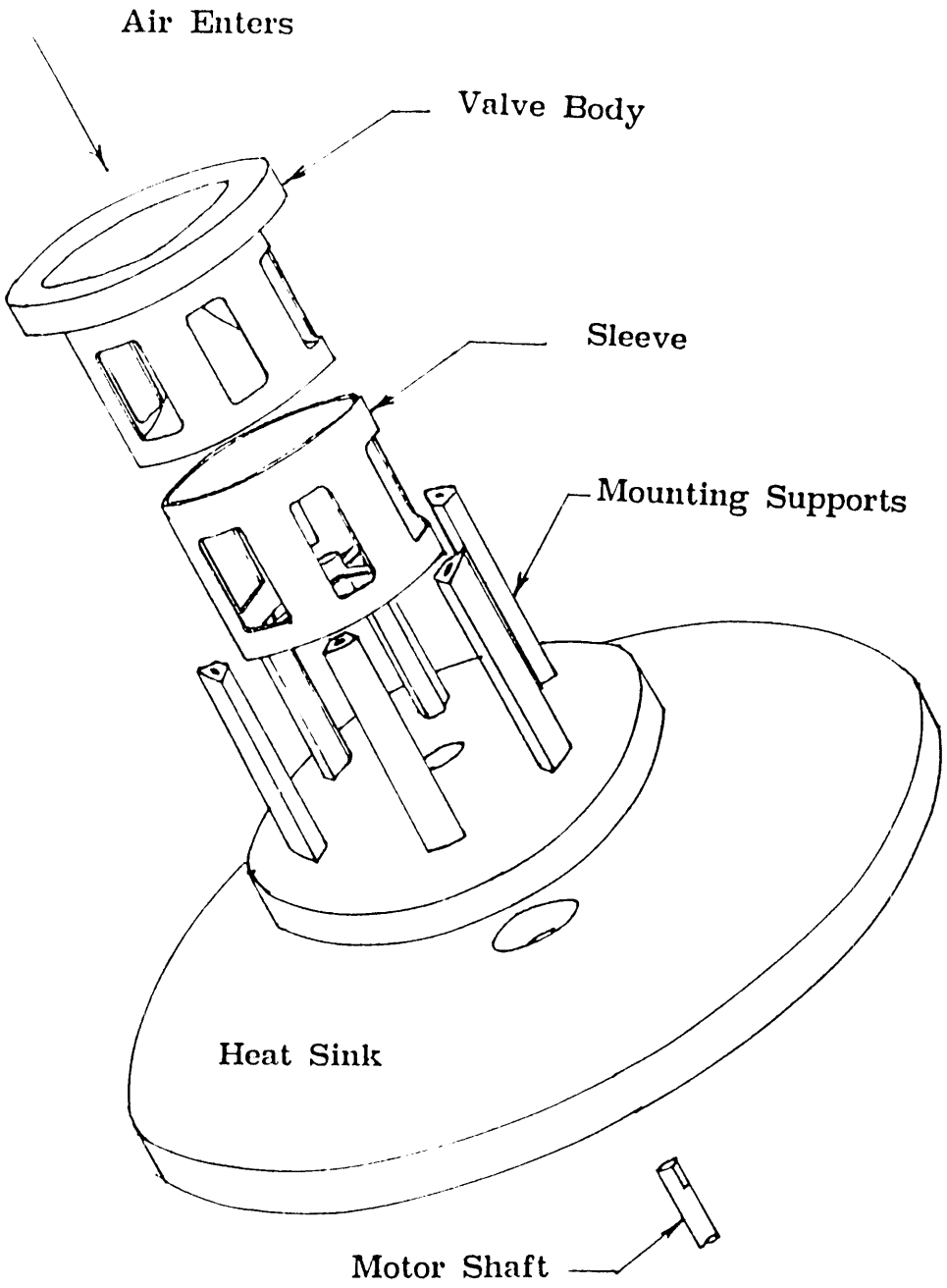

Figure 4.11 Exploded View of Rotary Actuated Control Valve

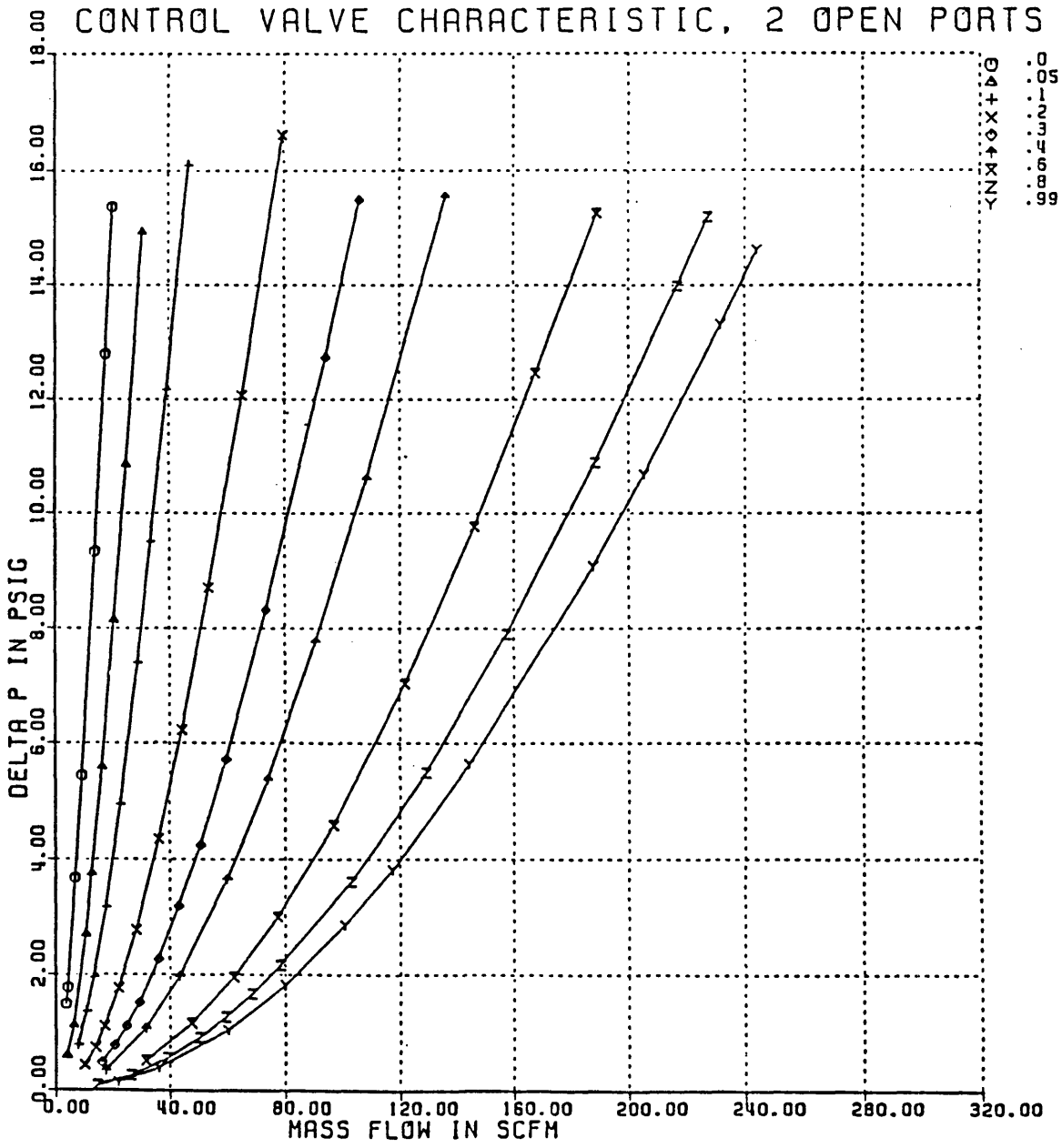

Figure 4.12 Control Valve Pressure Drop vs. Mass Flow Calibration
Pressure Drop = $P_{plenum} - P_0$

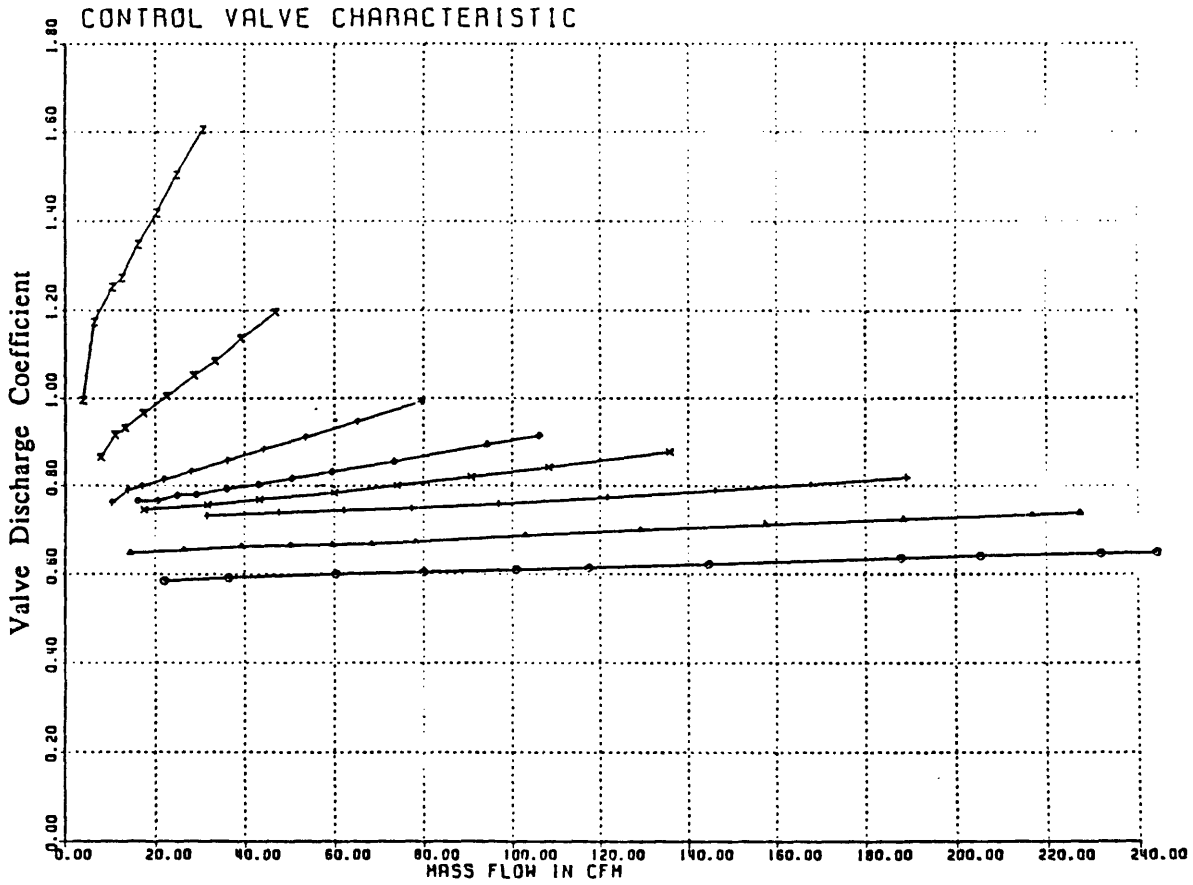

Figure 4.13(a) Measured Valve Discharge Coefficients Based on Indicated Throughflow Area

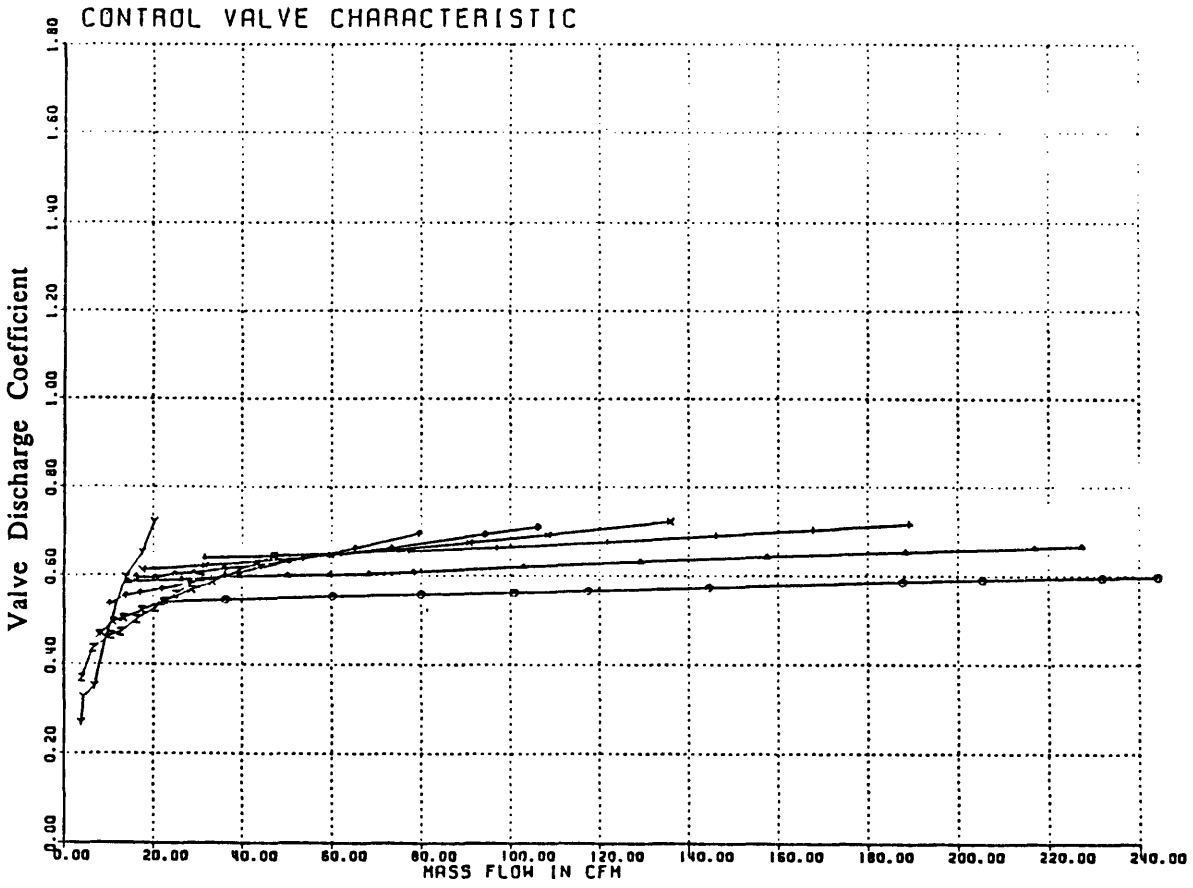

Figure 4.13(b) Measured Valve Discharge Coefficients Based on Throughflow Area with Leakage Path
Leakage Assumed to be Through Valve Annulus

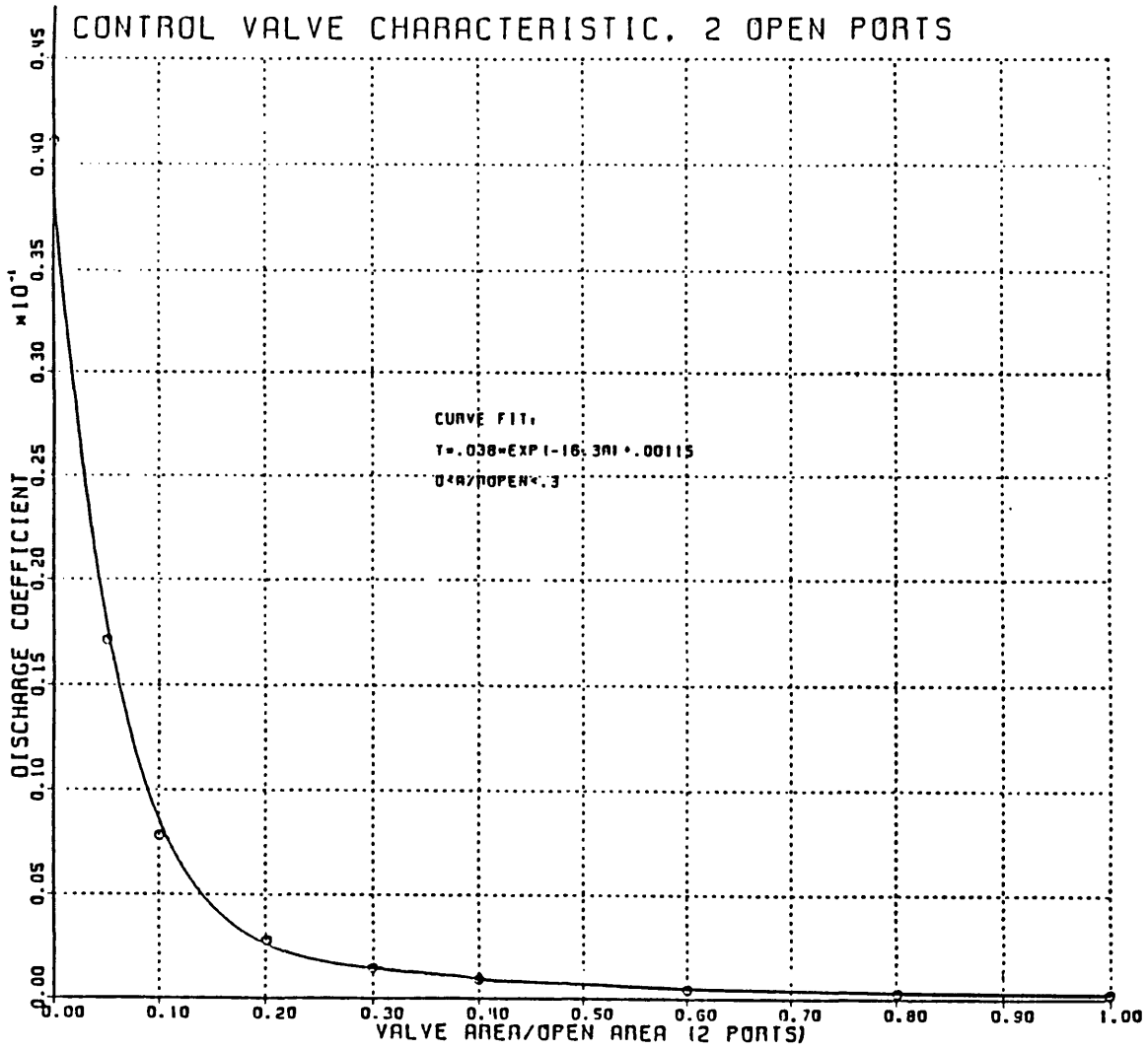

Figure 4.14 Experimental "Total" Discharge Coefficient vs. Indicated Throttle Area Coefficient = $(P_{plenum} - P_0)$ in psid/(Mass Flow in SCFM)^2

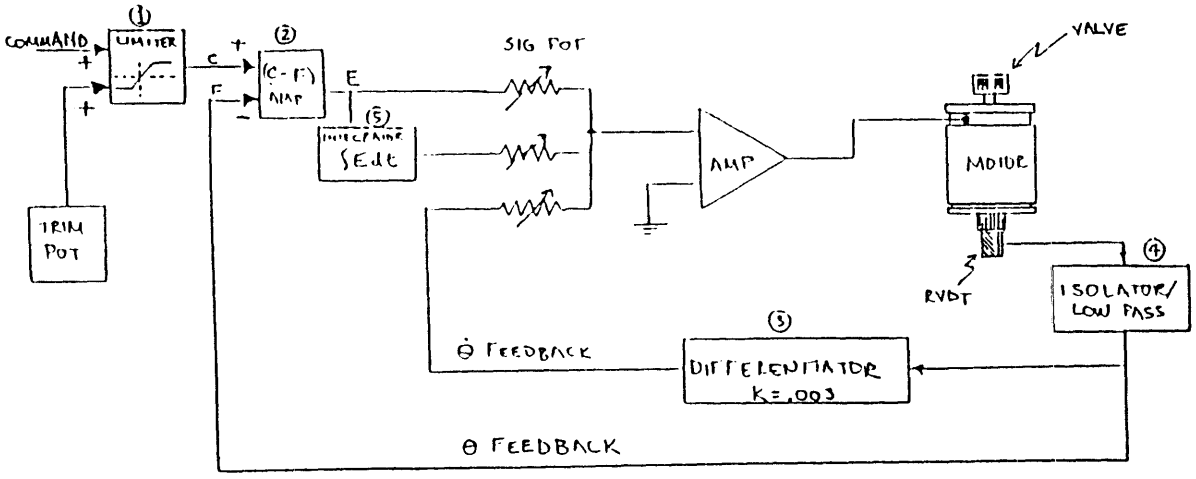

Figure 4.15 Motor Position Control Loop Schematic [13]

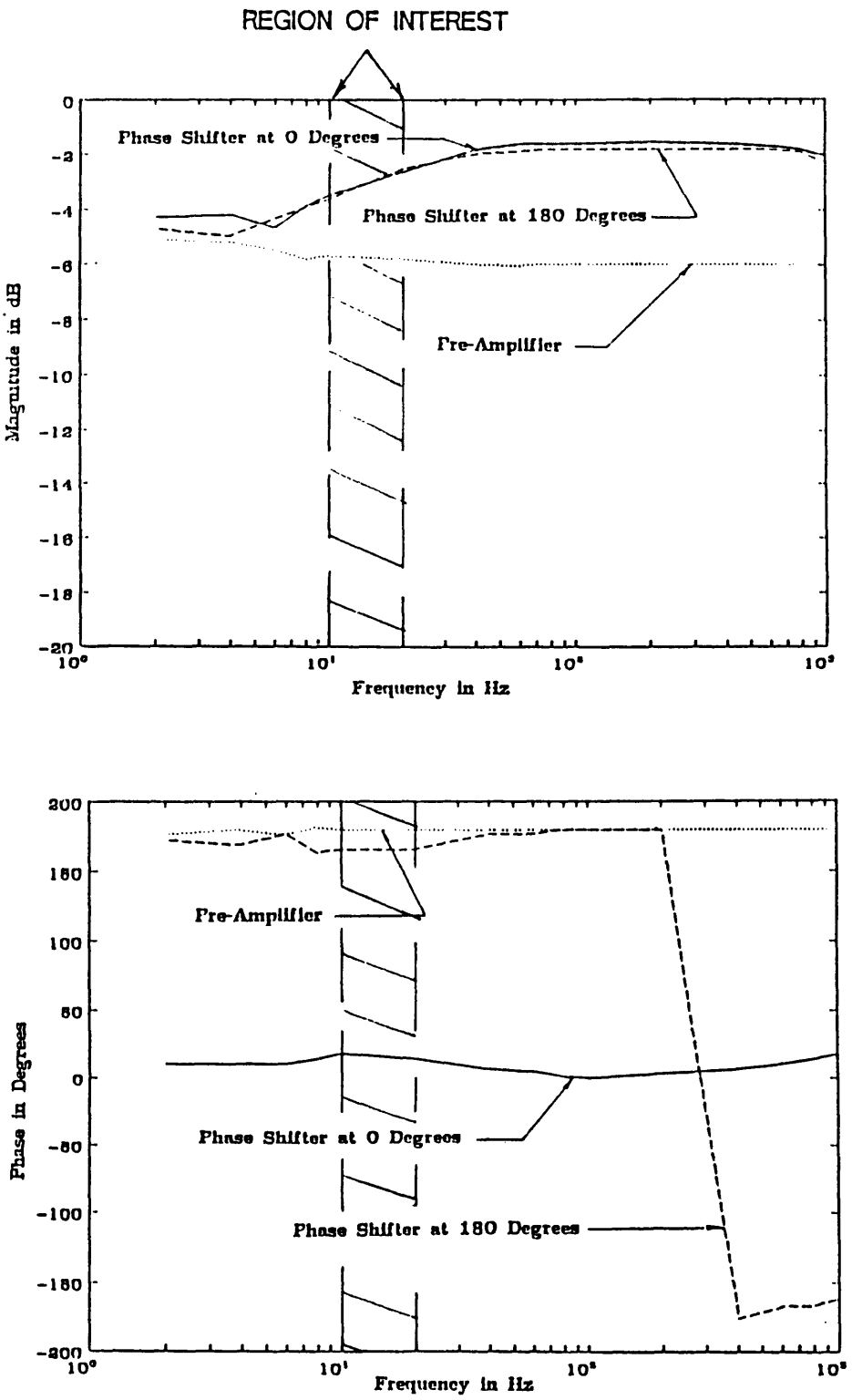

Figure 4.16 Phase Shifter and Pre-Amplifier Transfer Functions

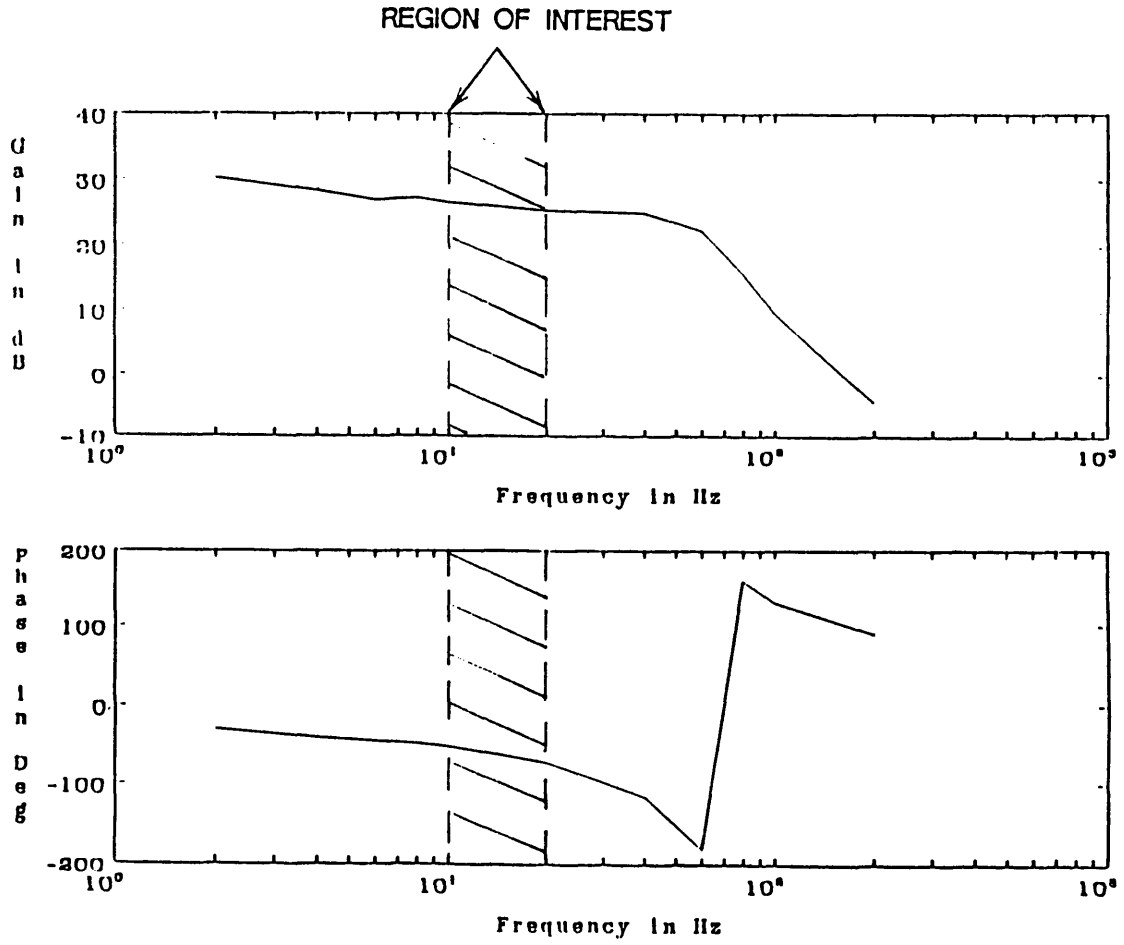

Figure 4.17(a) Motor Position Control Loop Transfer Function, Low Level Signal
Abrupt Change in Phase is an Artifice of Plotting near ±180°

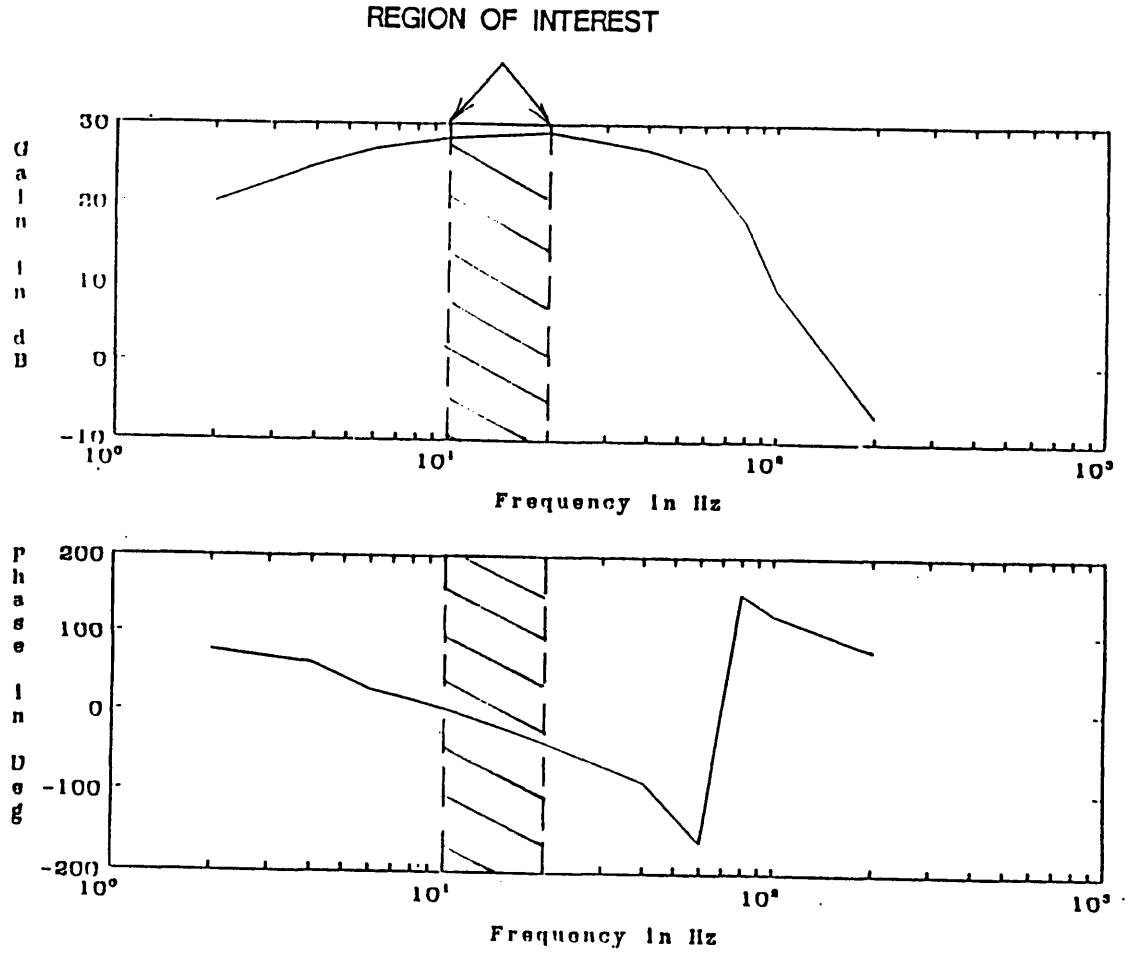

Figure 4.17(b) Motor Position Control Loop Transfer Function, High Level Signal Abrupt Change in Phase is an Artifice of Plotting Near ±180°

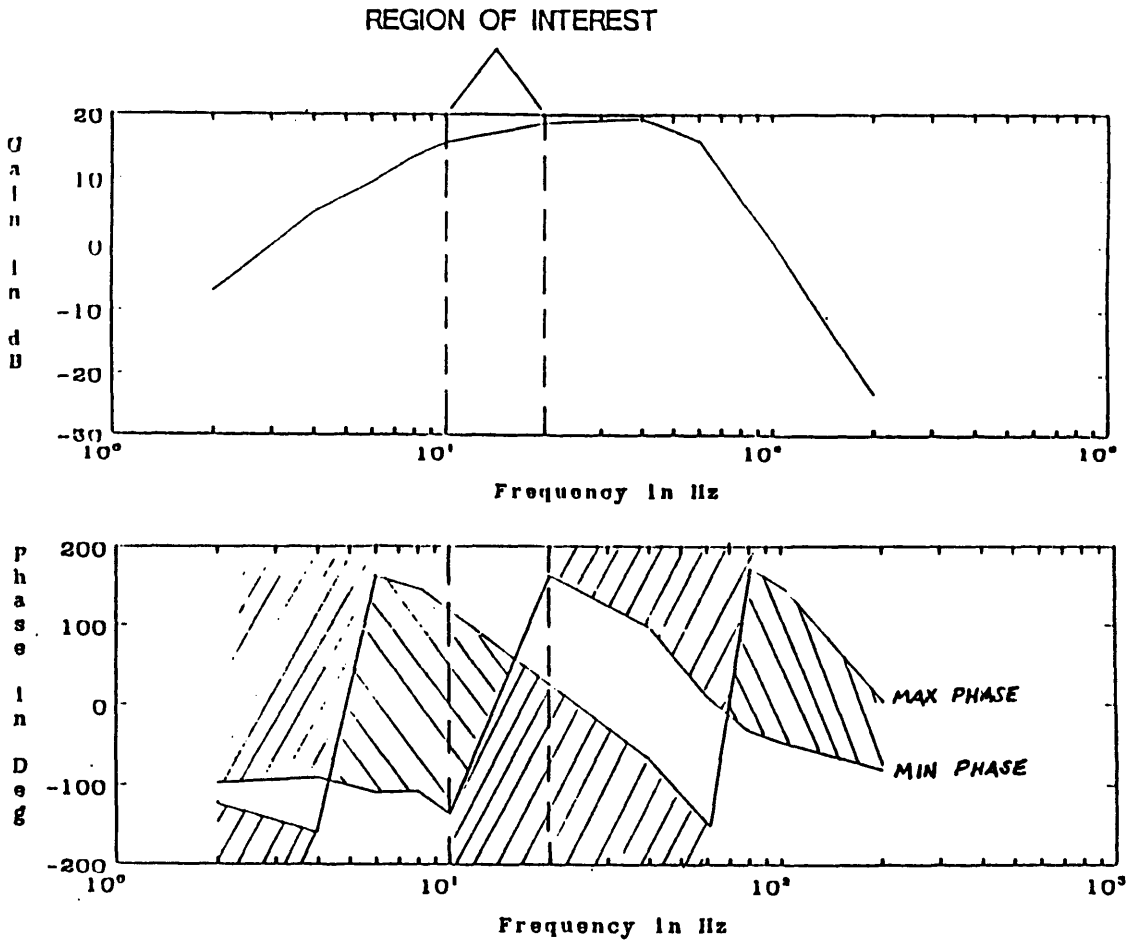

Figure 4.18 Overall Control Loop Transfer Function from Phase Shifter to RVDT
Abrupt Change in Phase is an Artifice of Plotting near ±180°
Cross-Hatched Areas Accessible Between Min and Max Phase Shift

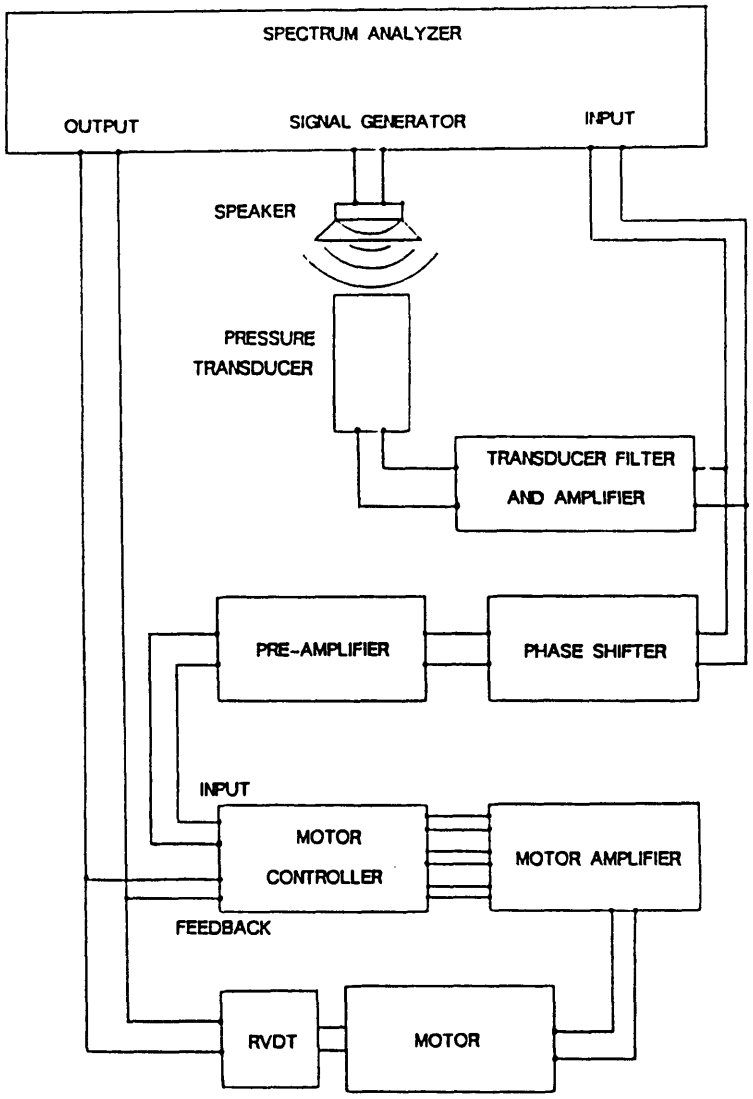

Figure 4.19(a) Overall Control Loop Transfer Function Including Pressure Transducer, Test Setup Schematic

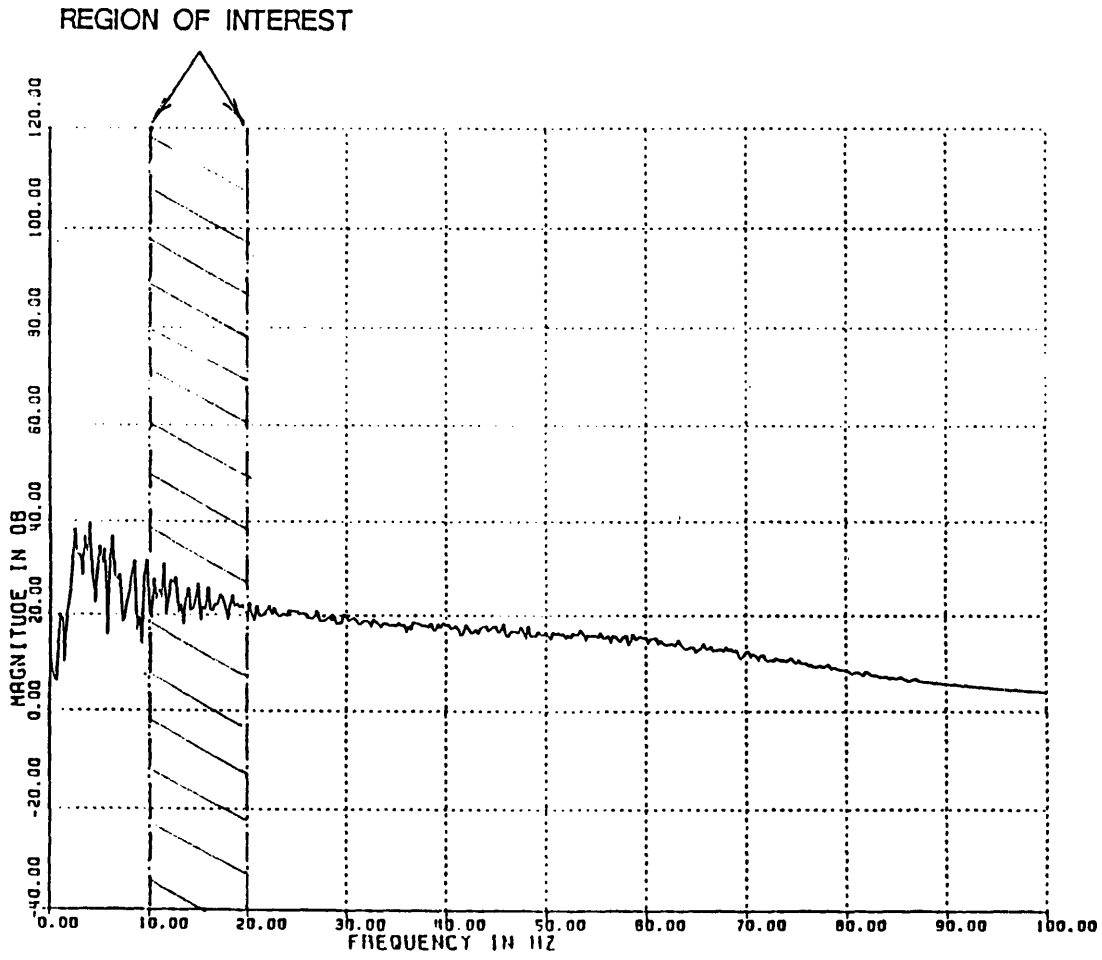

Figure 4.19(b) Overall Control Loop Transfer Function Including Pressure Transducer, Measured Magnitude

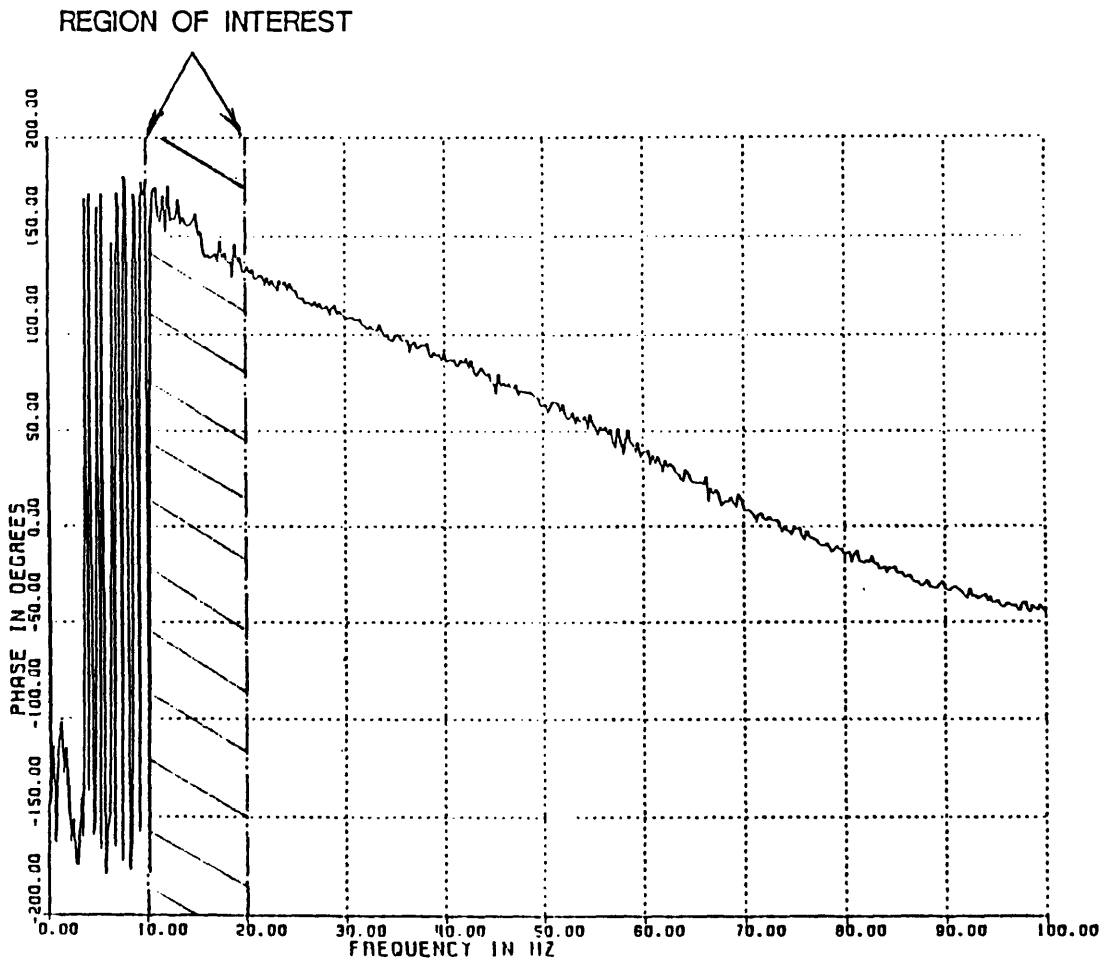

Figure 4.19(c) Overall Control Loop Transfer Function Including Pressure Transducer, Measured Phase

Abrupt Changes in Phase at Low Frequencies are an Artifice of Plotting Near ±180°

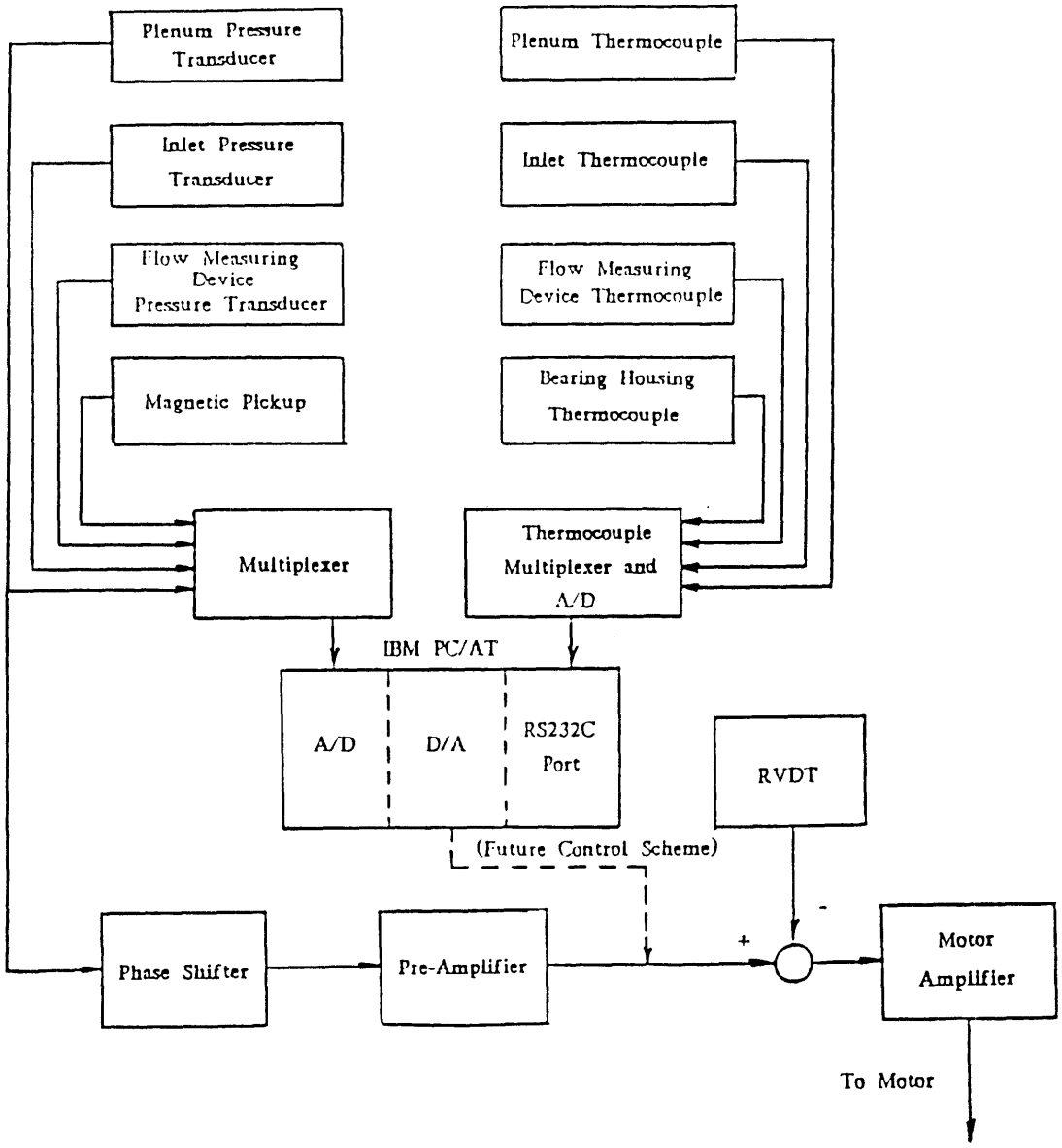

Figure 4.20 Schematic of Data Acquisition Inputs and Outputs to the Controller

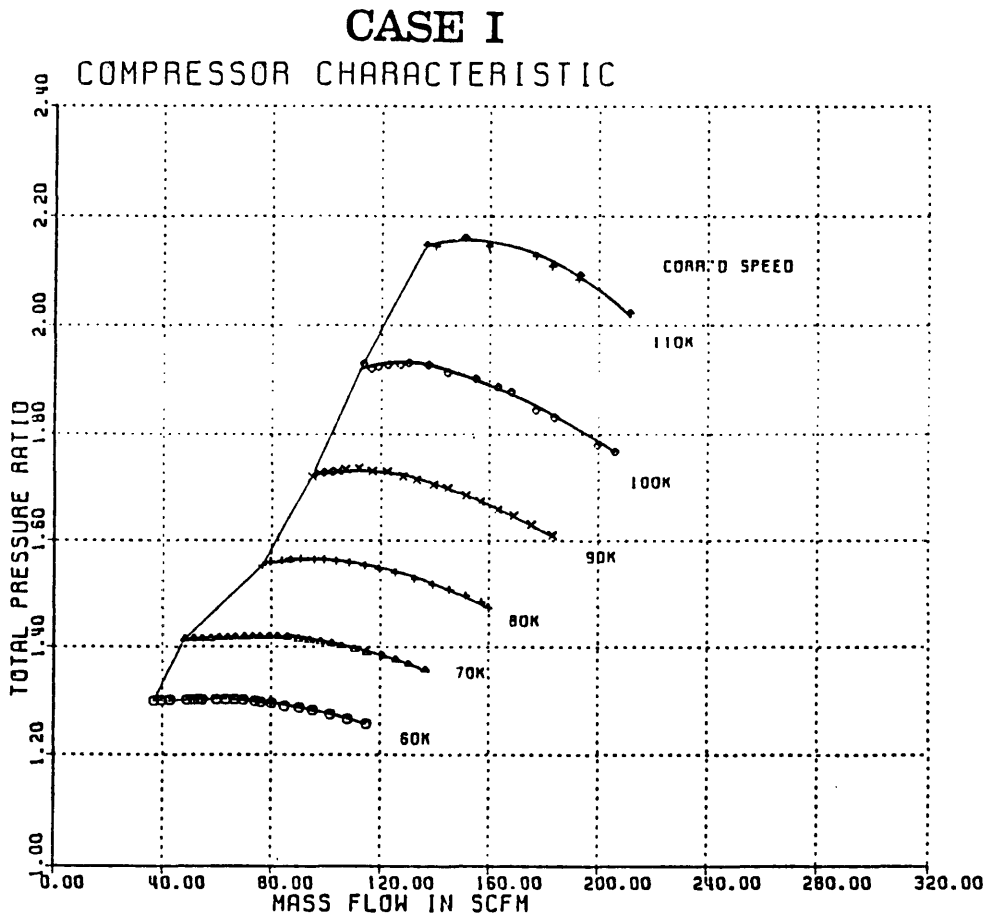

Figure 5.1(a) Measured Compressor Map in Small B Configuration, Pressure Ratio vs. SCFM

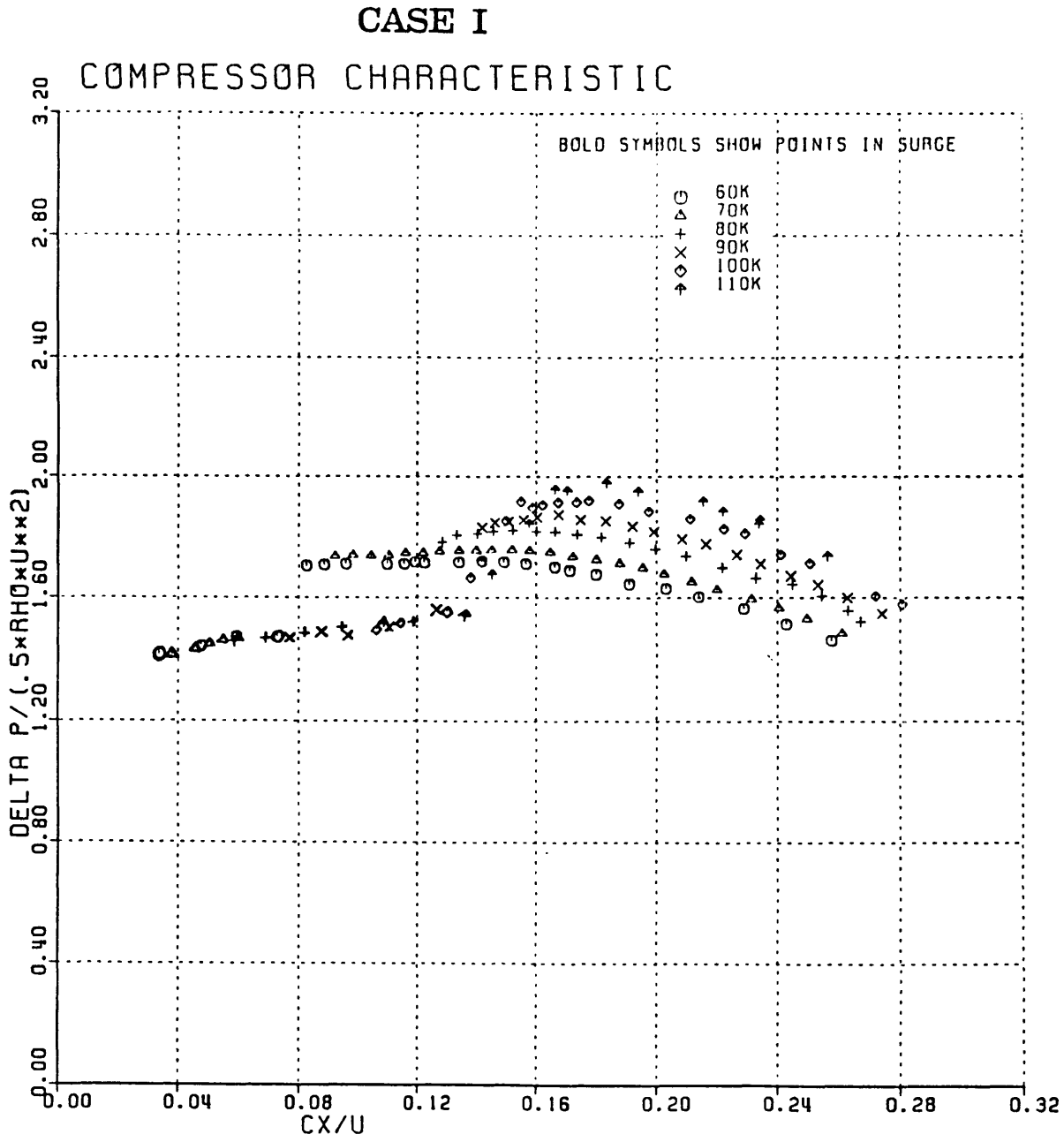

Figure 5.1(b) Measured Compressor Map in Small B Configuration, ψ vs. ϕ

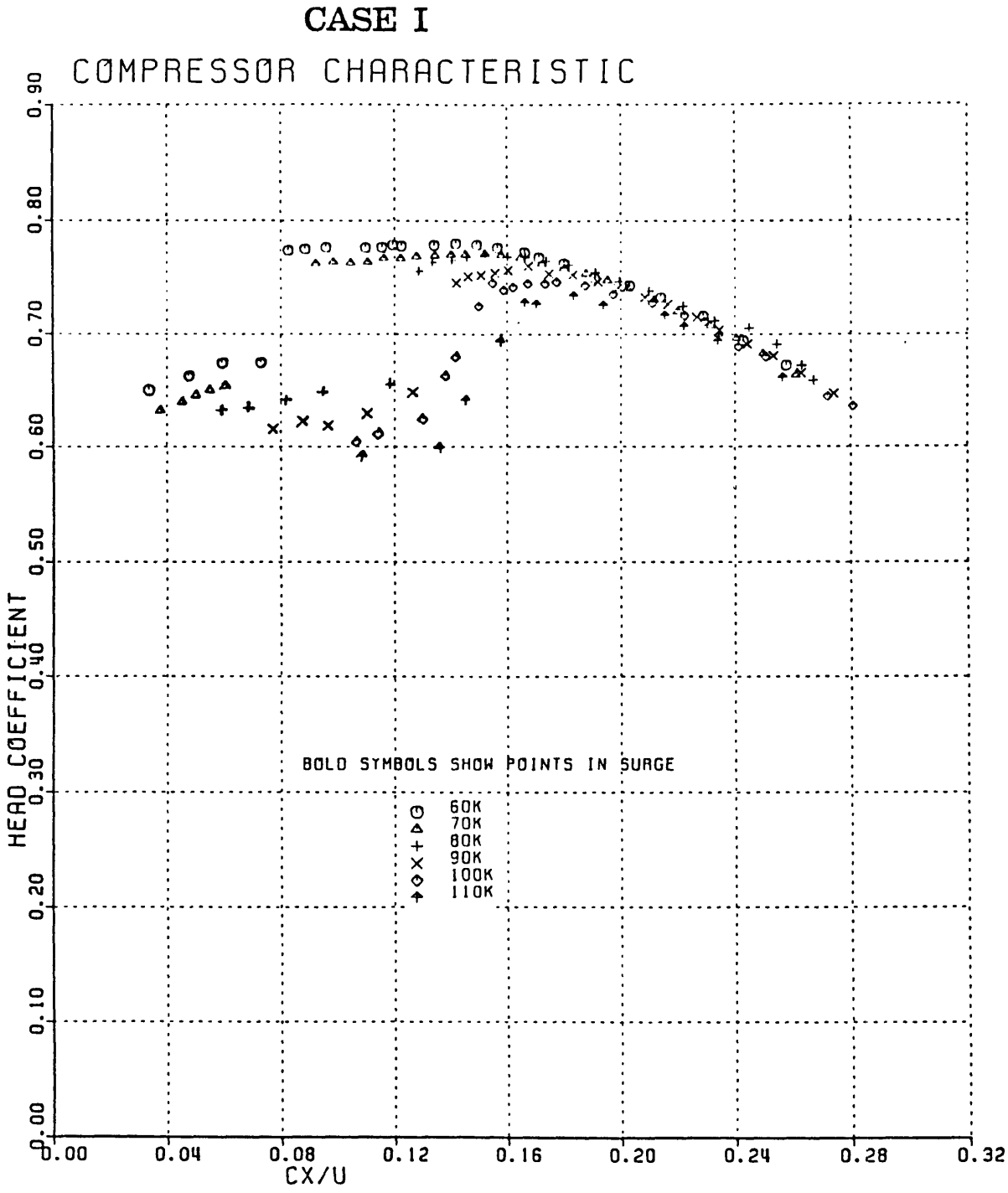

Figure 5.1(c) Measured Compressor Map in Small B Configuration, Head Coefficient vs. ϕ

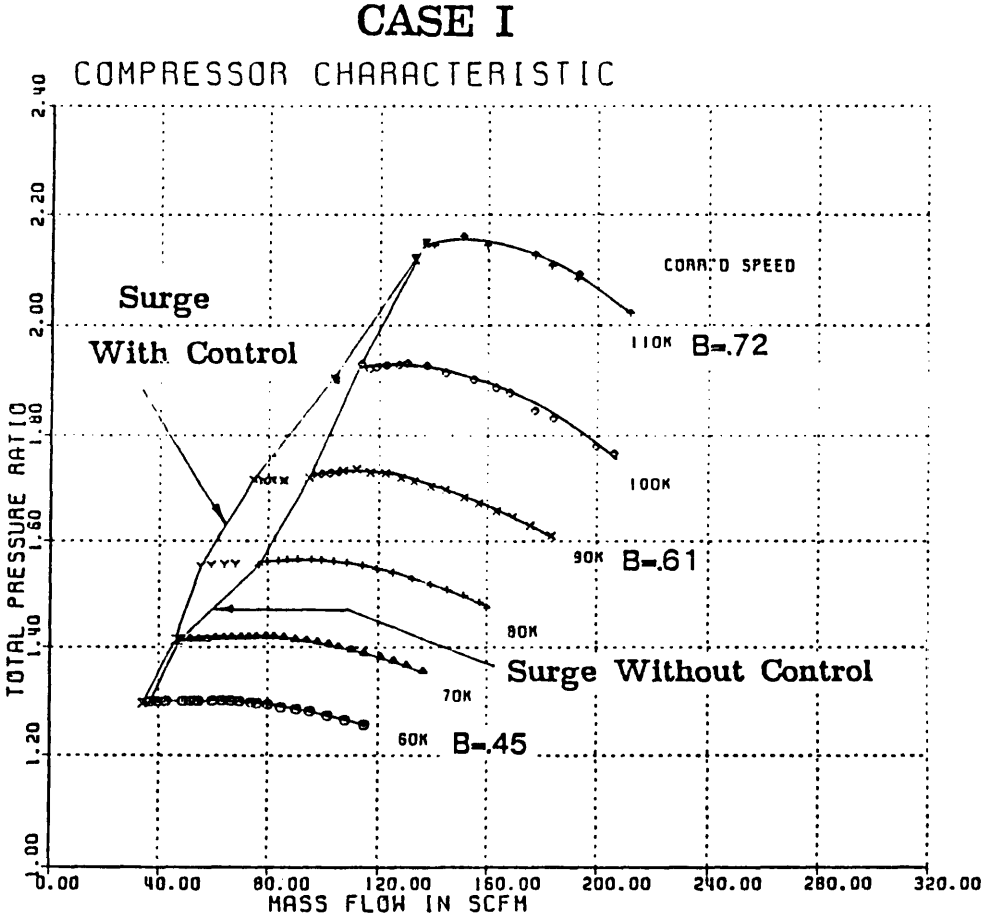

Figure 5.2 Surge Line Shift with Controller, Small B Configuration

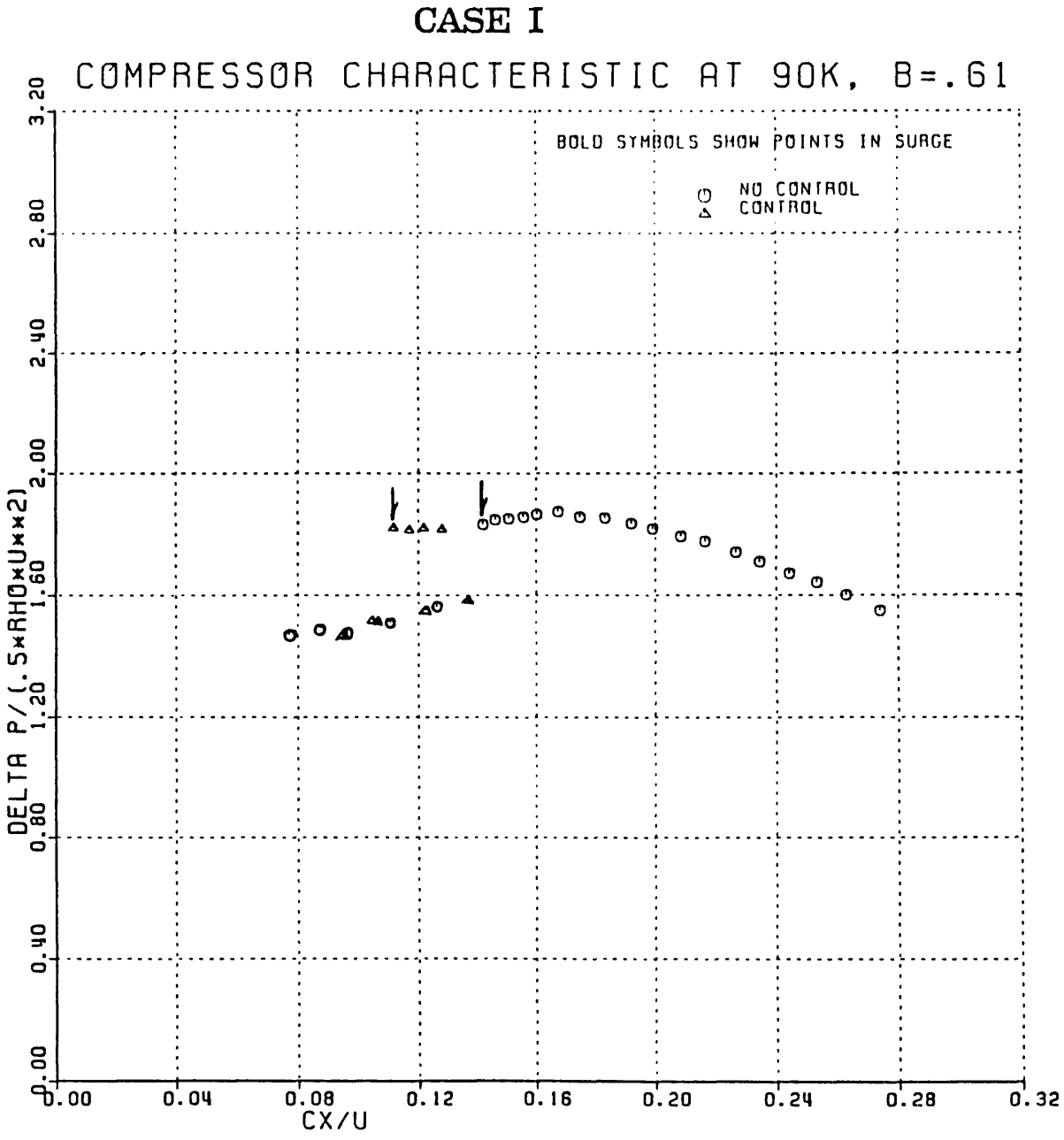

Figure 5.3 Control Effect at N_{corr} = 90,000 RPM on ψ vs. ϕ
Near Surge Points Shown Flagged

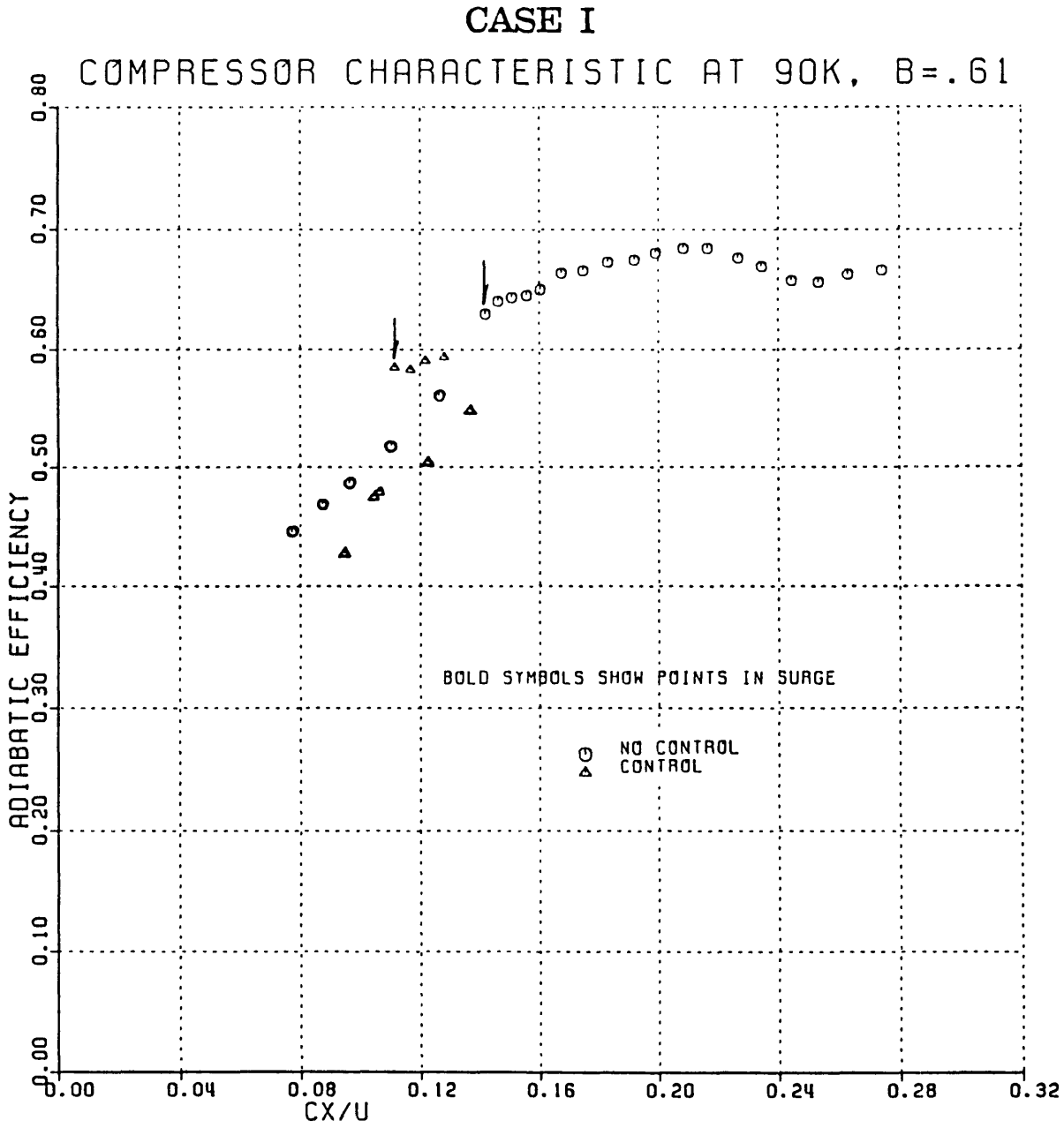

Figure 5.4 Compressor Adiabatic Efficiency Under Control at N_{corr} = 90,000 RPM Near Surge Points Shown Flagged

CASE II

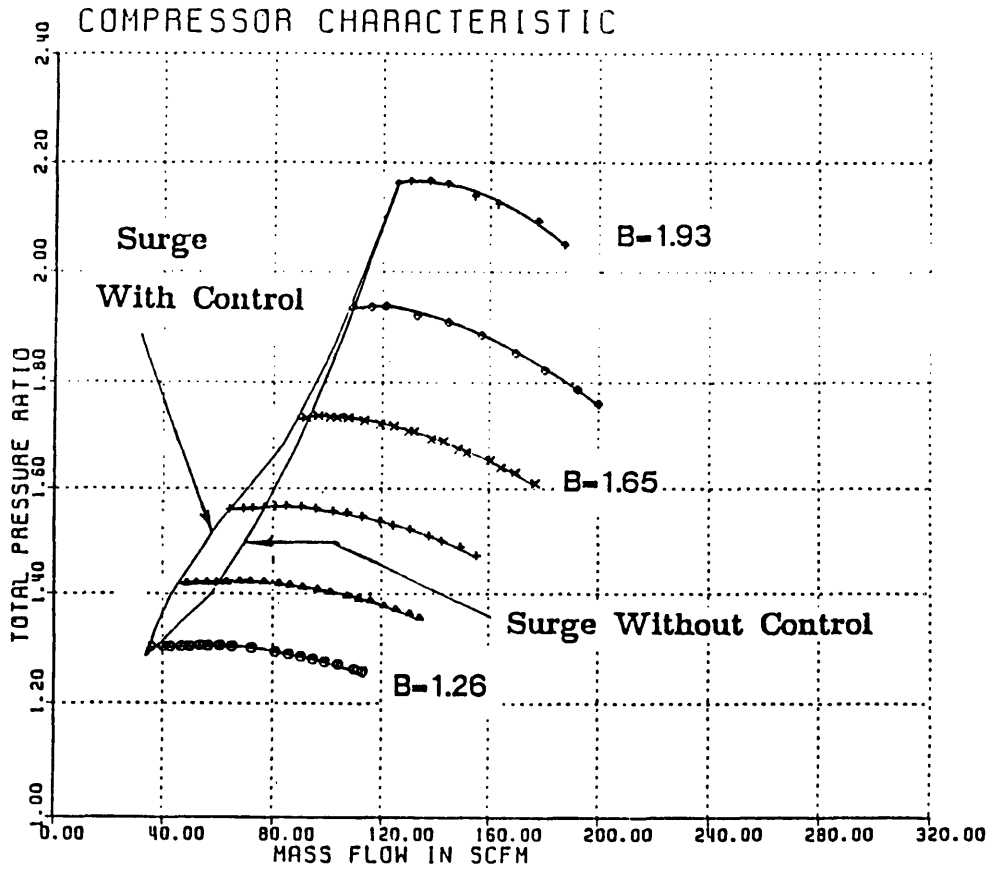

Figure 5.5 Measured Compressor Map in Large B Configuration, ψ vs. ϕ Surge Line Extension with Control Shown

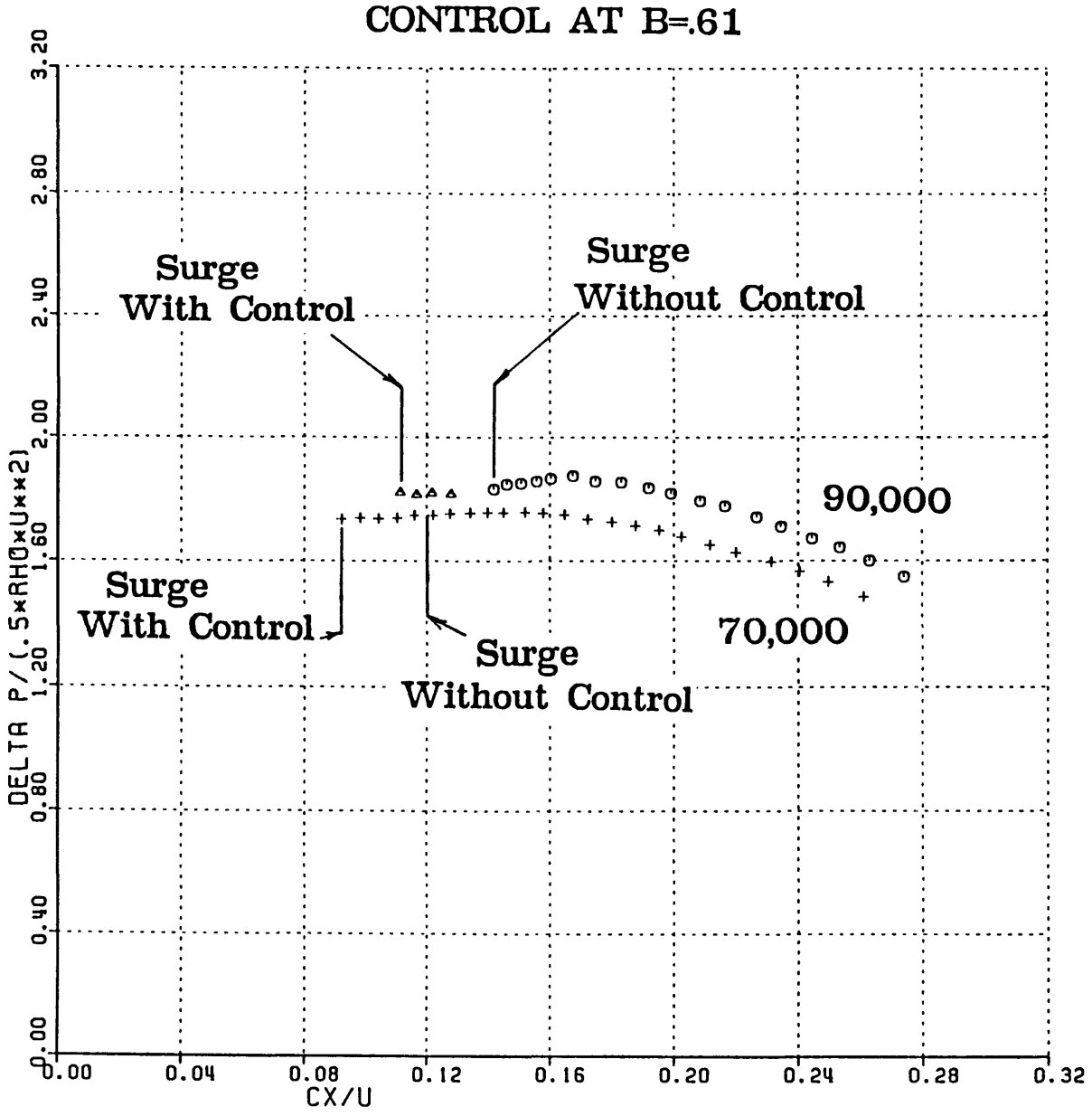

Figure 5.6 Control Effect at the Same B Parameter, Different Speed
B = .61 at N_{corr} = 70,000 -- Case III
= 90,000 -- Case I

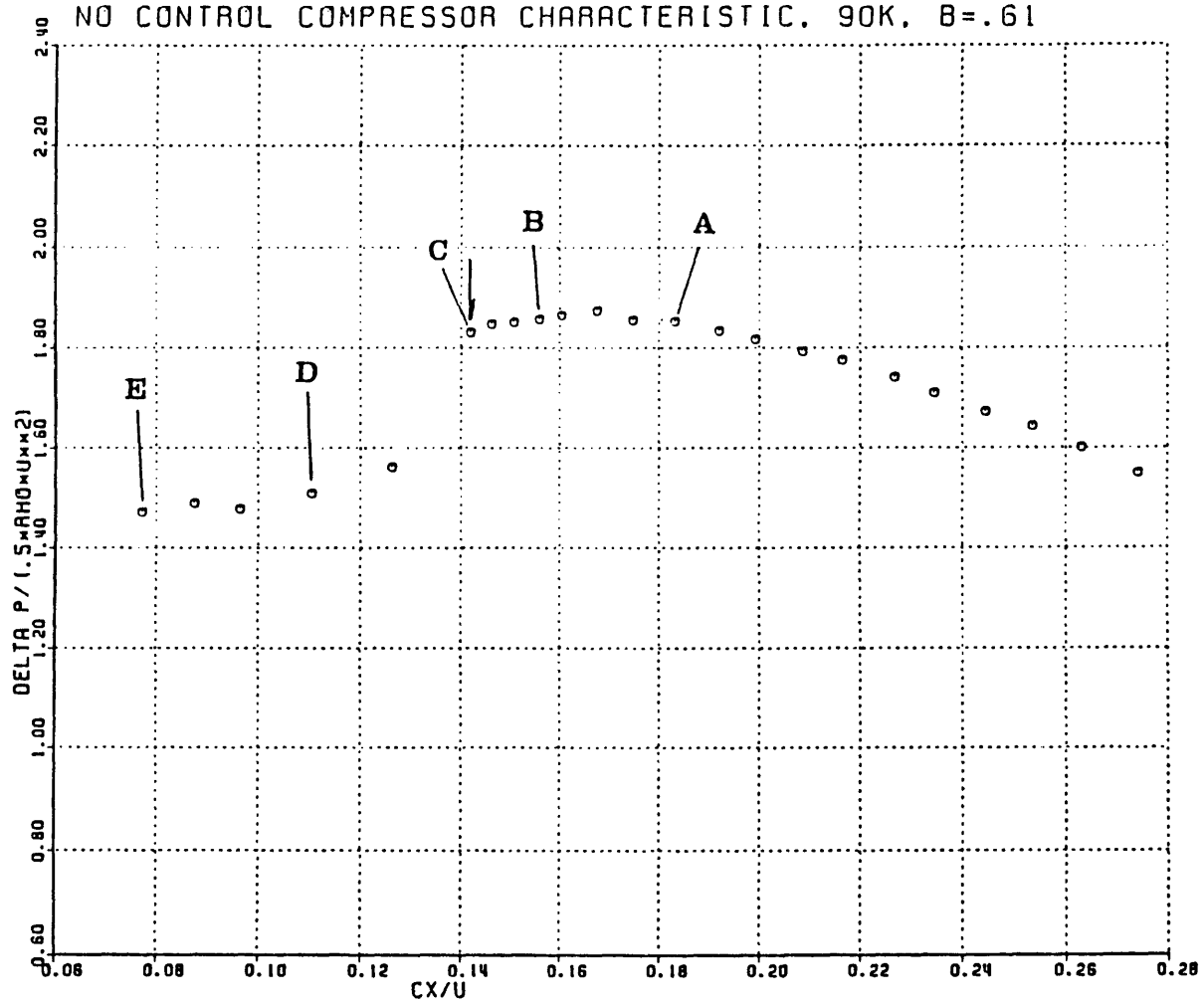

Figure 5.7(a) Nondimensional Compressor Characteristic at N_{corr} = 90,000 RPM, Showing Measured Points, Near Surge Point Shown Flagged

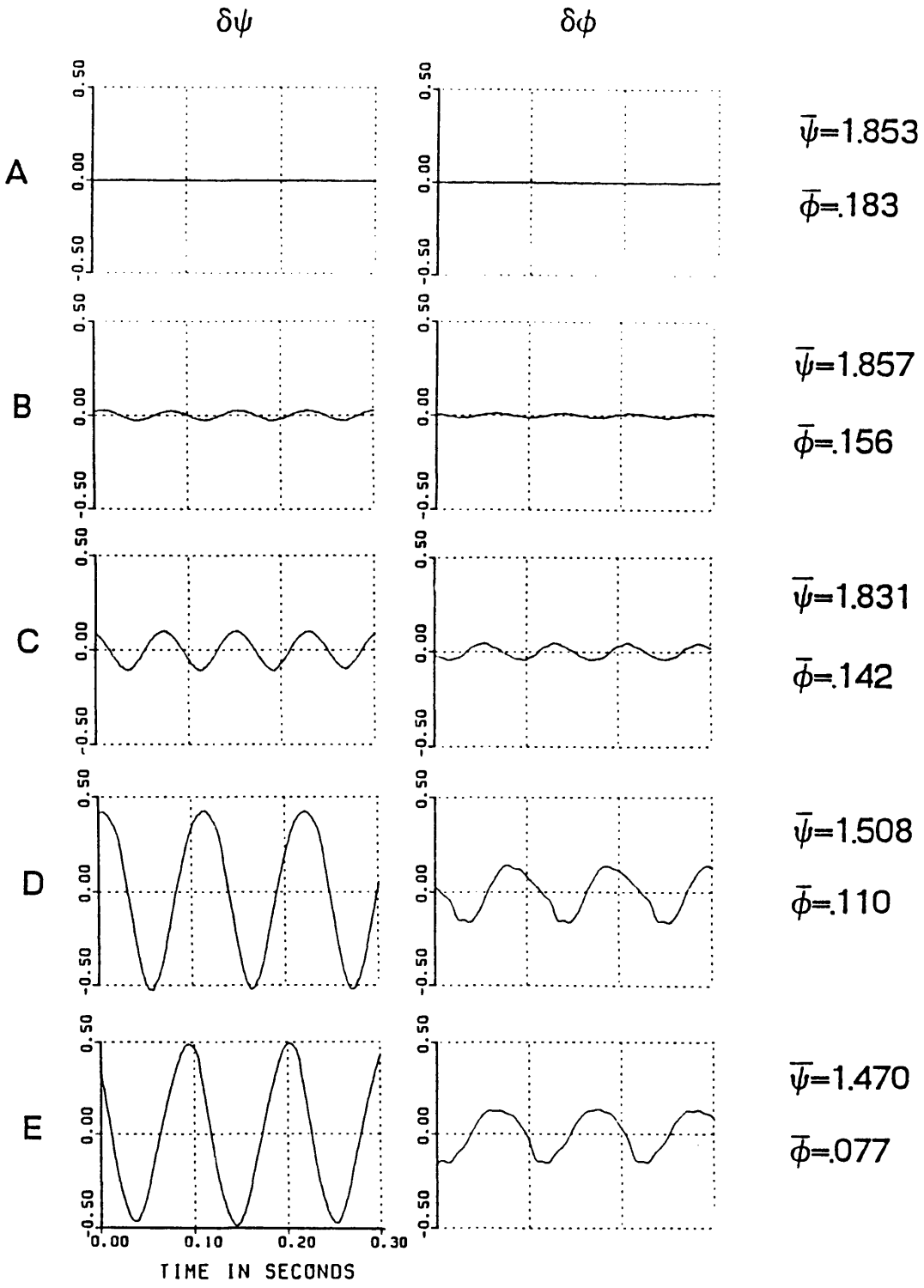

Figure 5.7(b) Nondimensional Perturbations at N_{corr} = 90,000 RPM

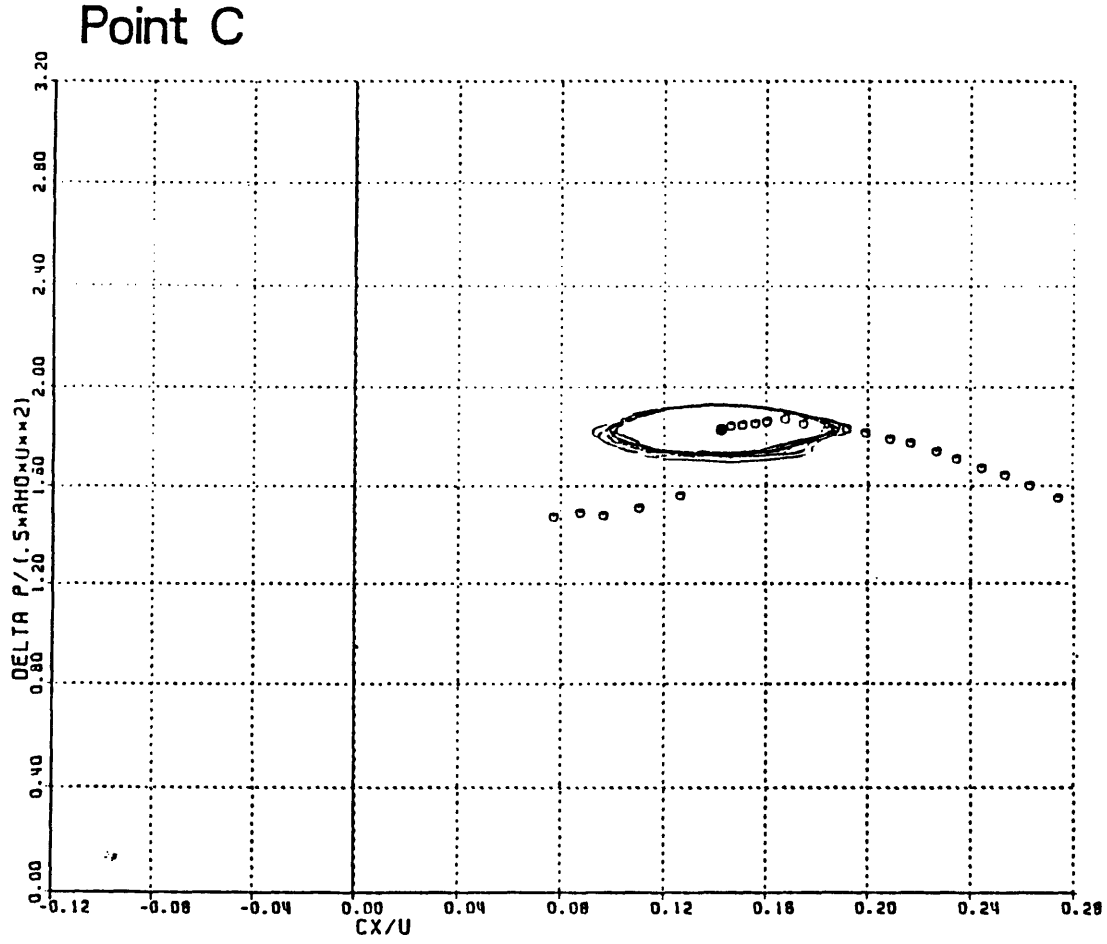

Figure 5.8 Uncontrolled Mild Surge Cycles in ψ - ϕ Plane, Point C Mean Operating Point Shown Solid

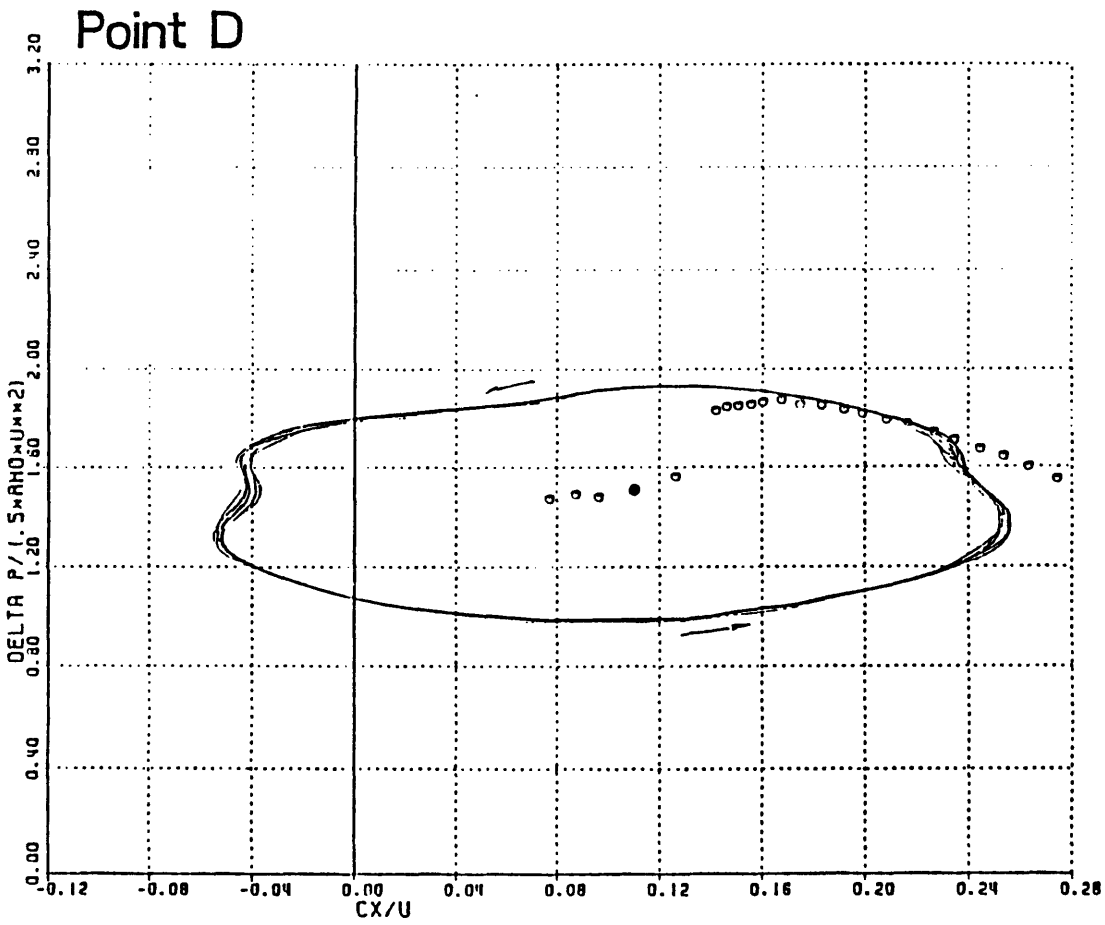

Figure 5.9 Uncontrolled Deep Surge Cycles in ψ - ϕ Plane, Point D
Mean Operating Point Shown Solid

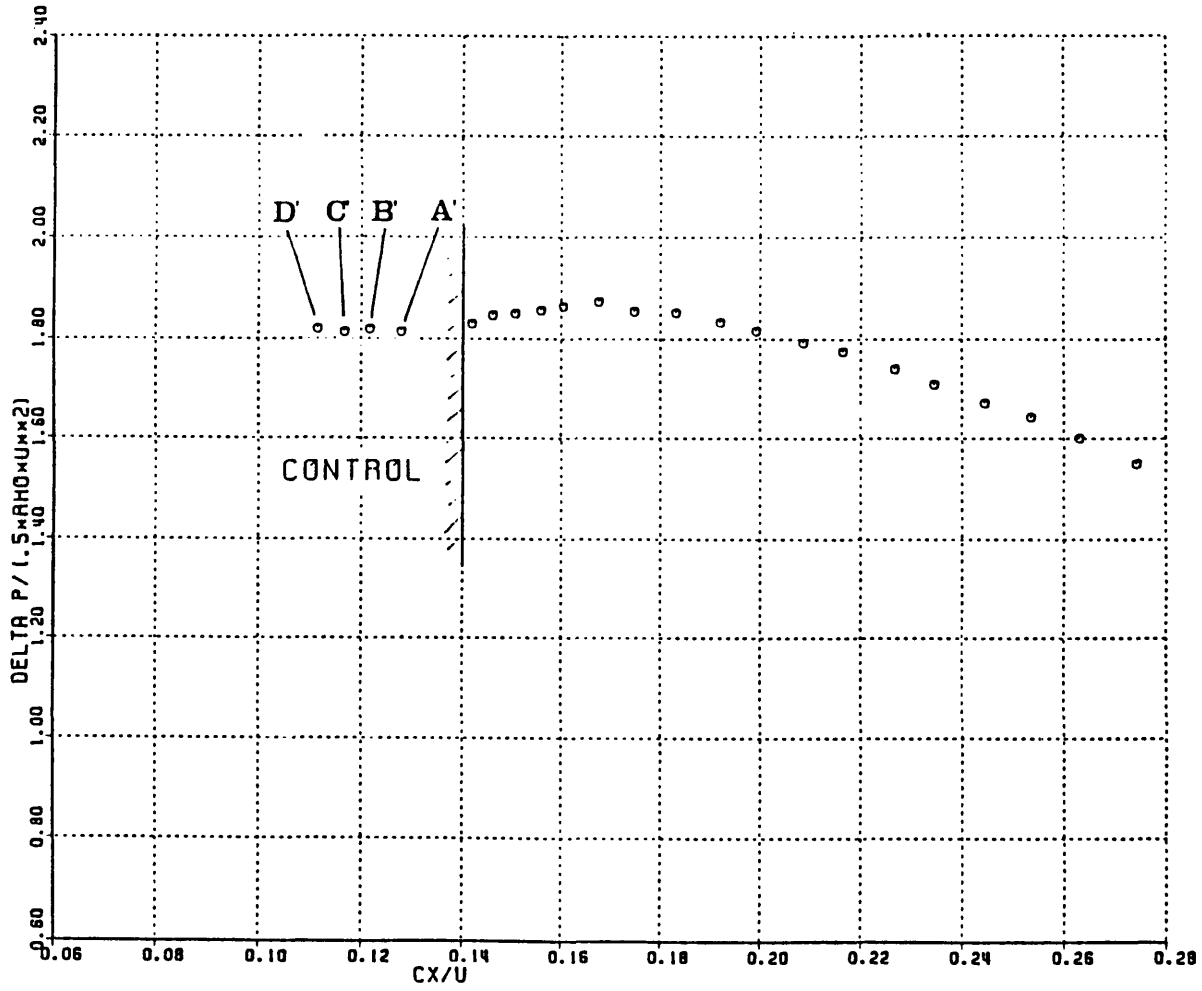

Figure 5.10(a) Nondimensional Compressor Characteristic at N_{corr} = 90,000 RPM, Showing Measured Control Points

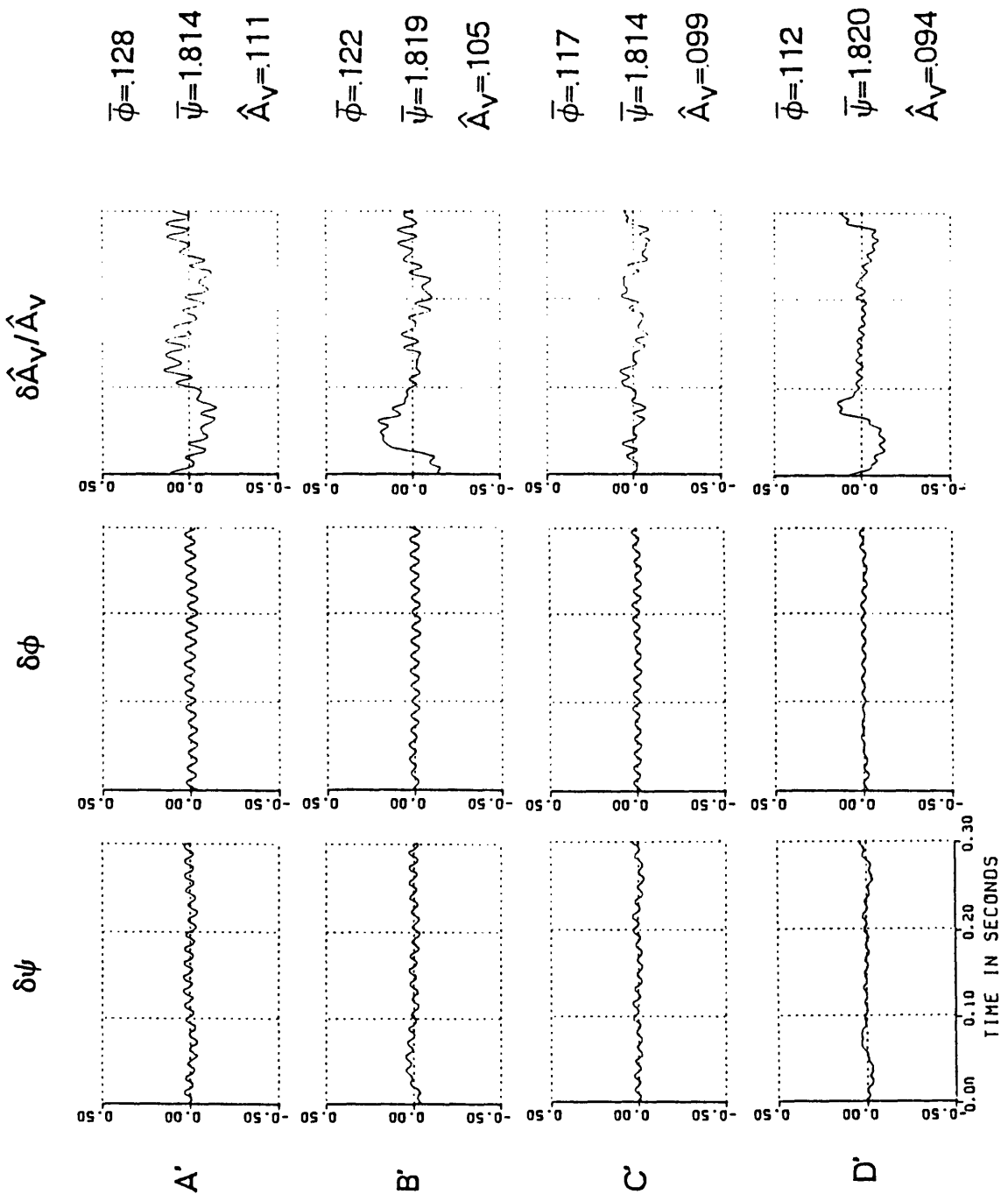

Figure 5.10(b) Nondimensional Perturbations at N_{corr} = 90,000 RPM Under Control

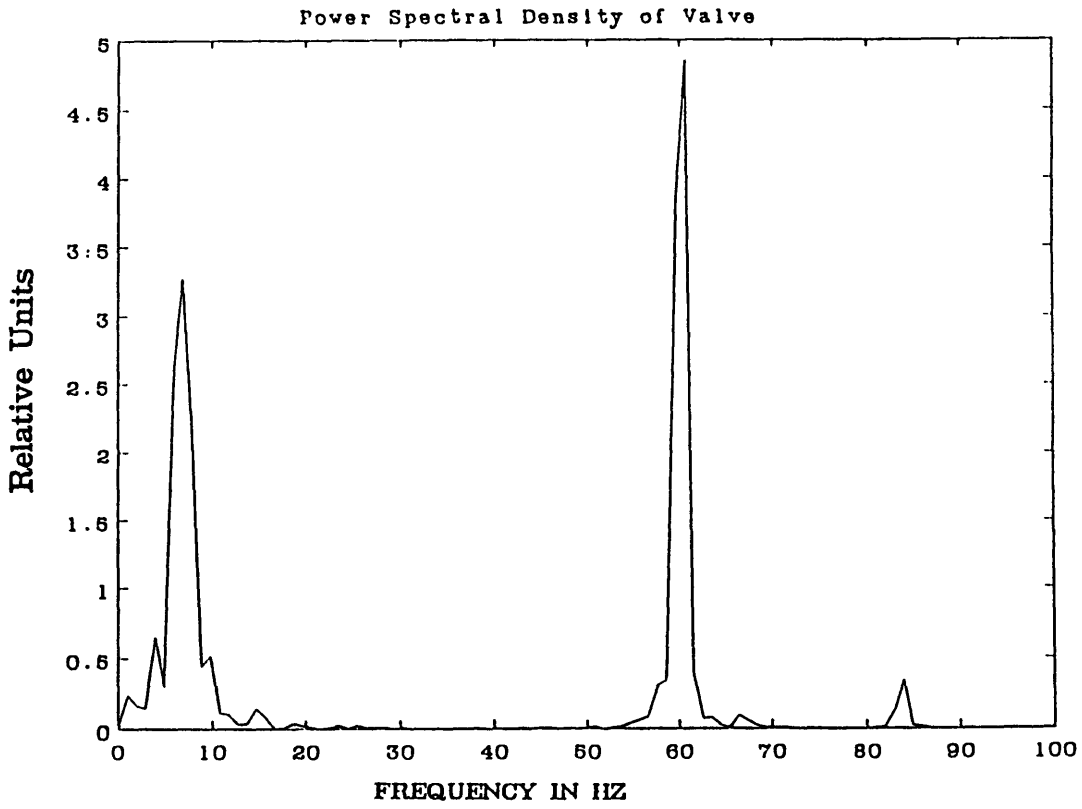

Figure 5.11 Power Spectral Density of Valve Motion Under Control at Point A'

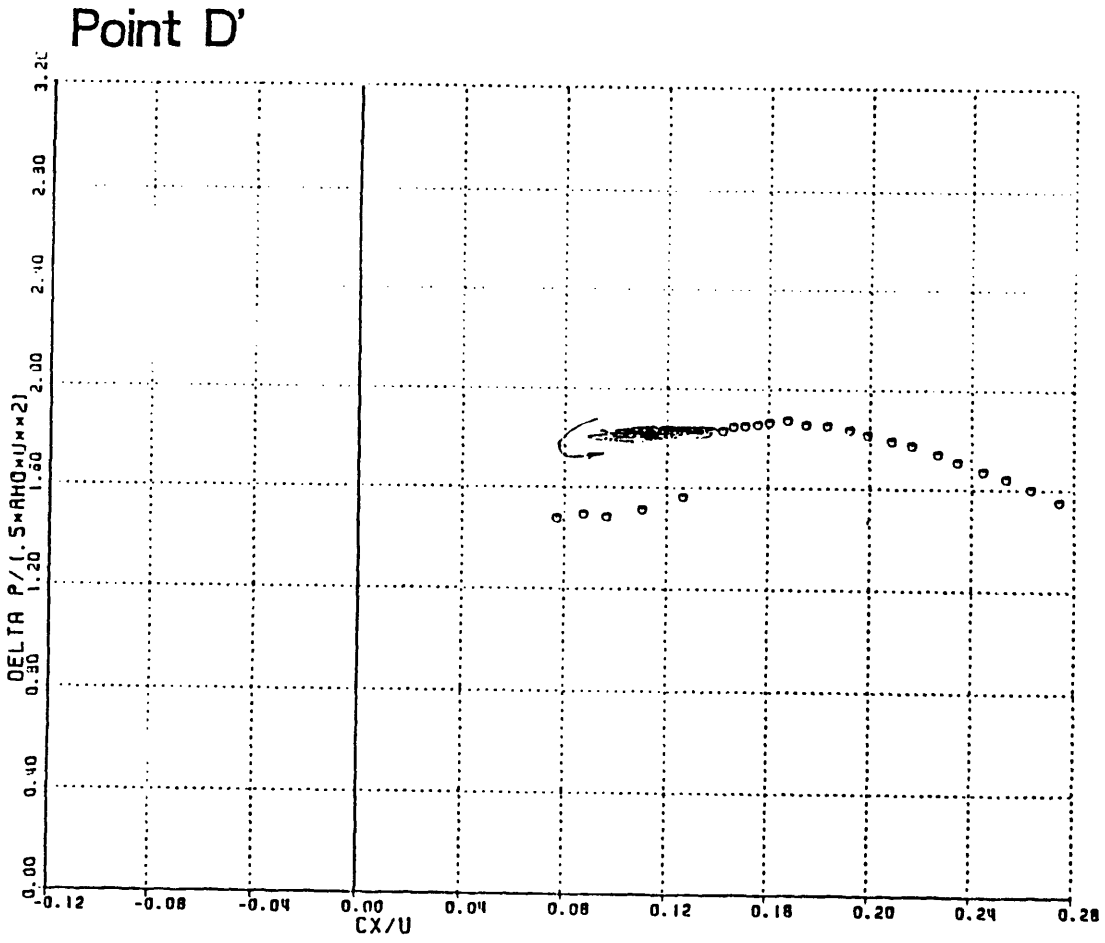

Figure 5.12 Controlled Perturbations in ψ - ϕ Plane, Point D'

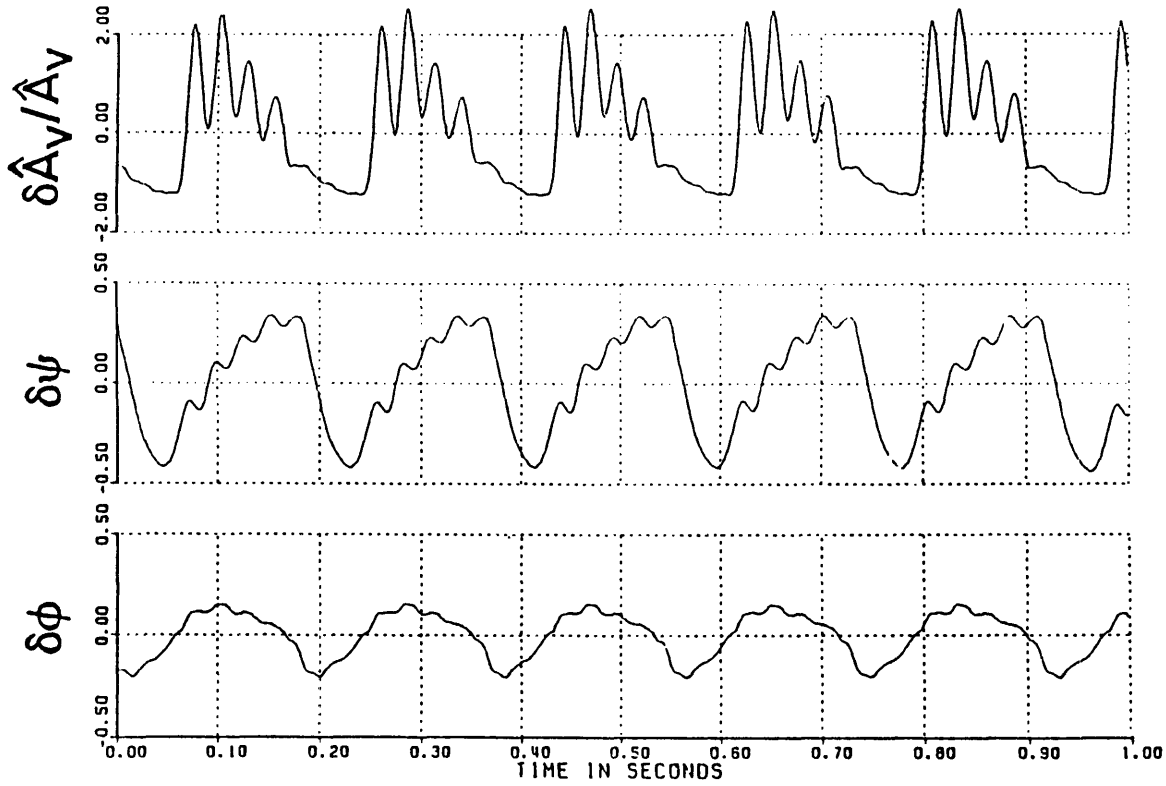

Figure 5.13 Nondimensional Perturbations with Control in Deep Surge

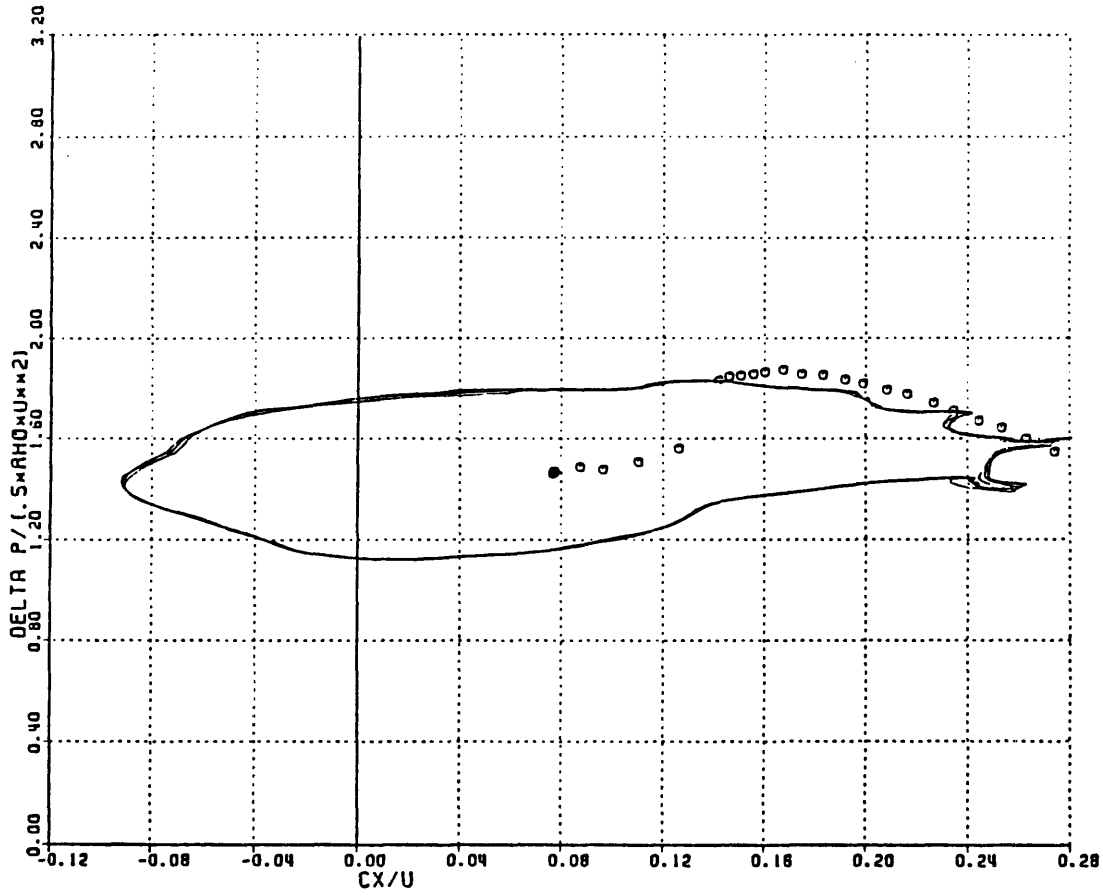

Figure 5.14 Deep Surge Cycles with Control in ψ - ϕ Plane
Mean Operating Point Shown Solid

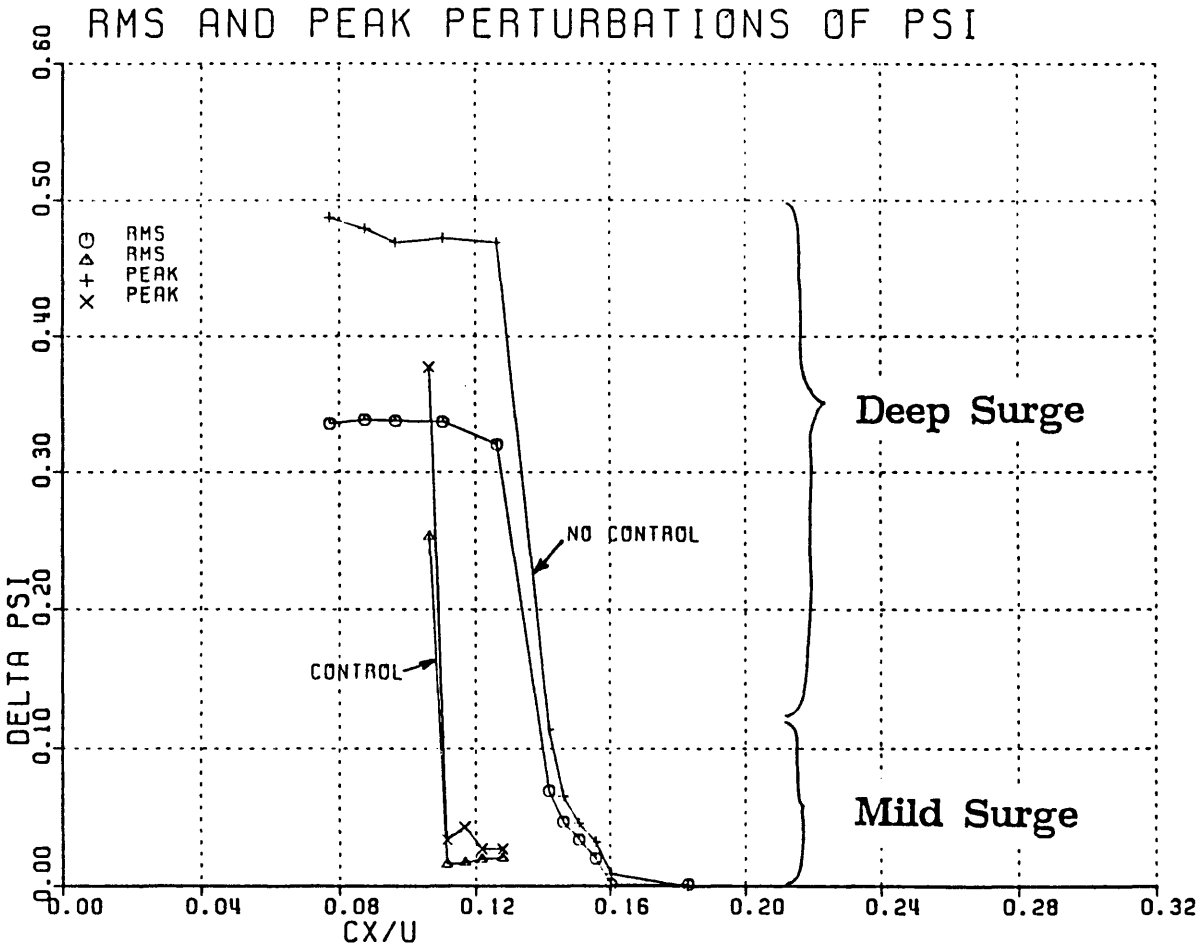

Figure 5.15 RMS and Peak Amplitudes of ψ With and Without Control

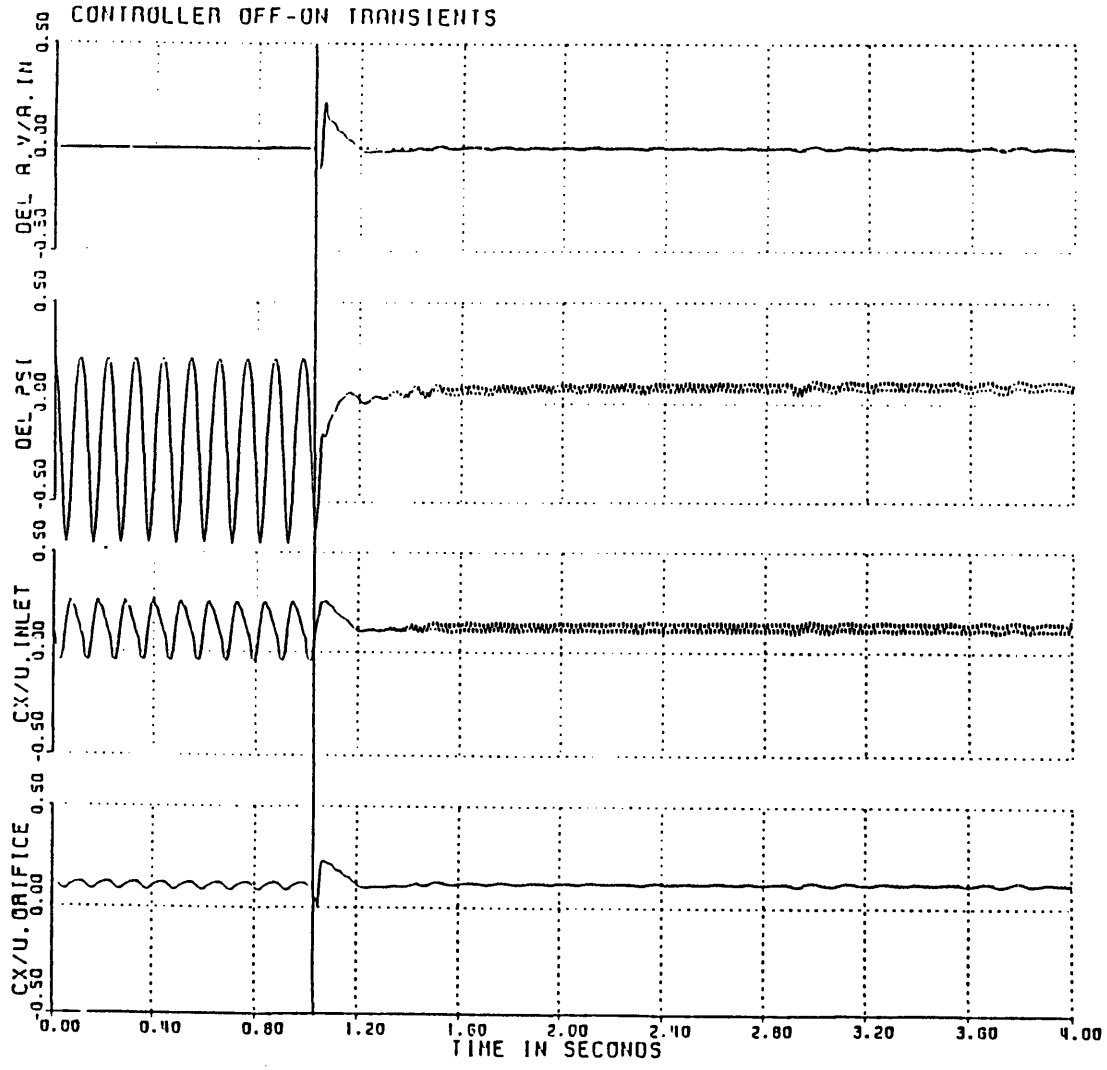

Figure 5.16(a) Nondimensional Perturbations During Controller Off-On Transient $\phi = .12$, $\psi = 1.87$, Gain = 10, Phase Approximately Zero Degrees

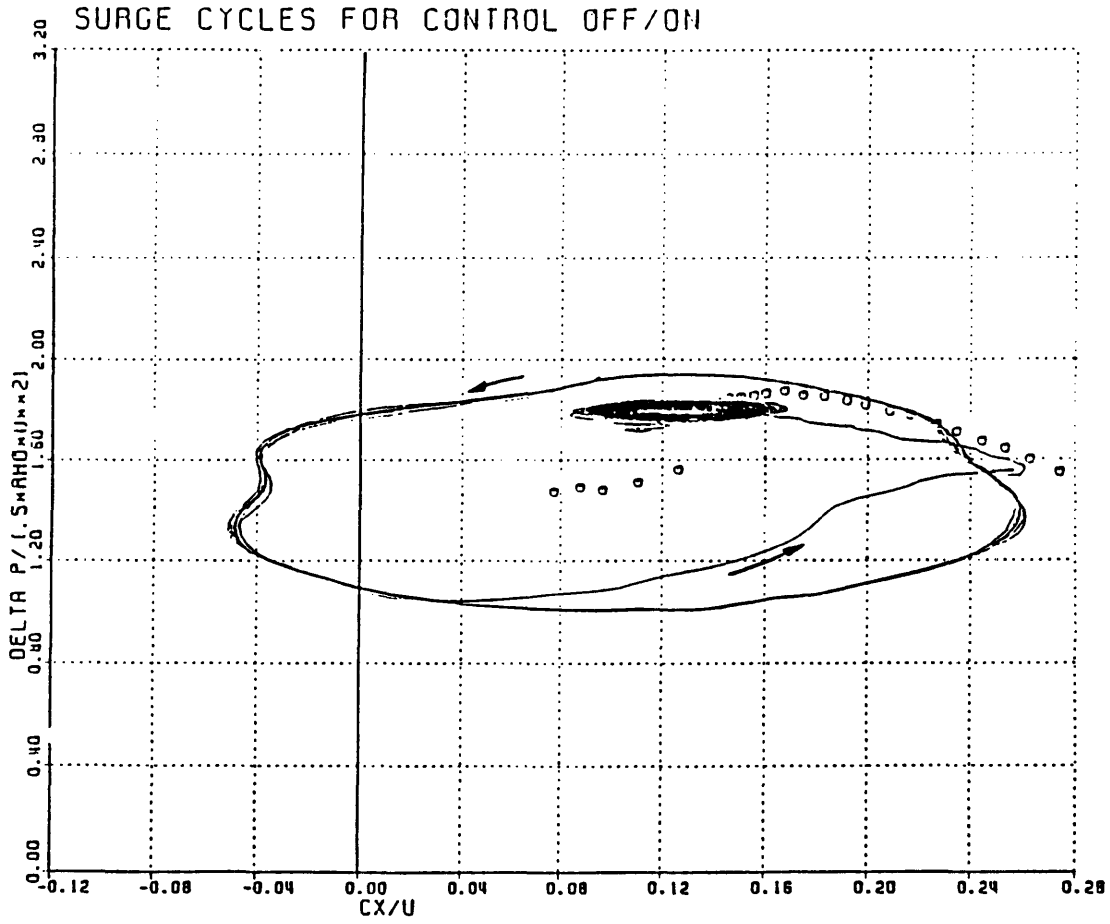

Figure 5.16(b) Instability Cycles in ψ - ϕ Plane During Controller Off-On Transient

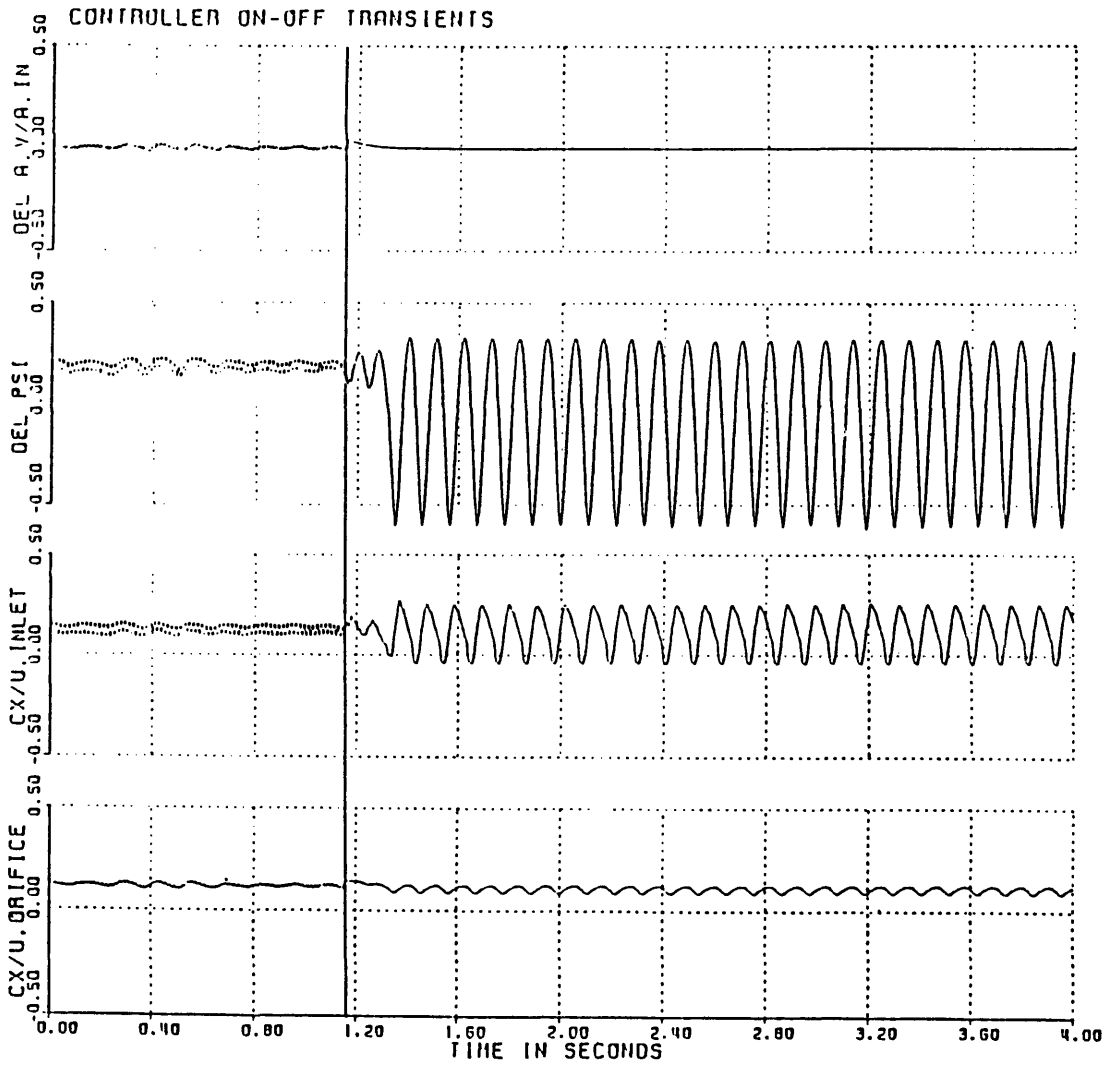

Figure 5.17 Nondimensional Perturbations During Controller On-Off Transient $\phi = .12$, $\psi = 1.62$, Gain = 10, Phase Approximately Zero Degrees

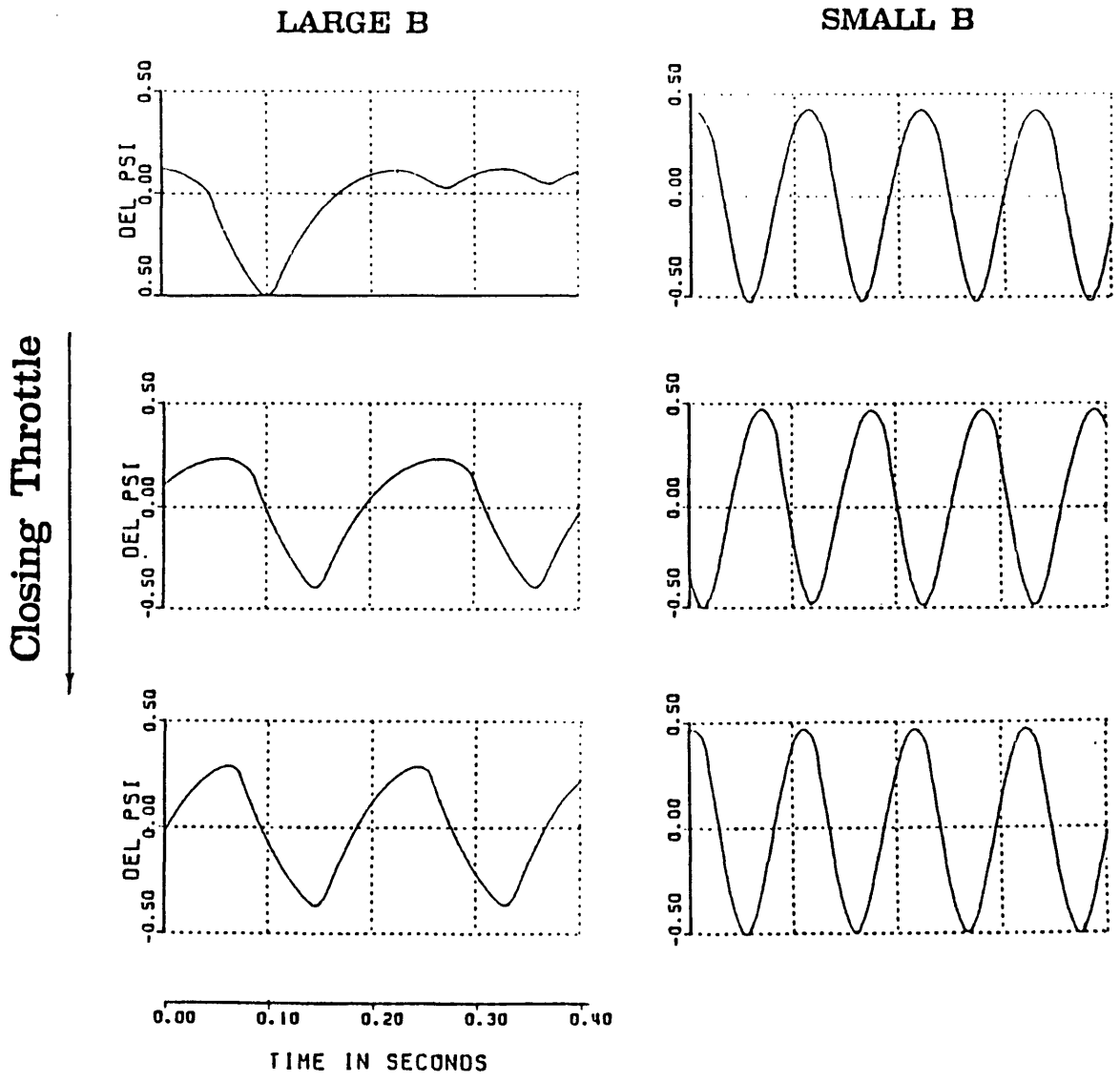

Figure 5.18 B Dependence of Surge Initiation in Terms of $\delta\psi$

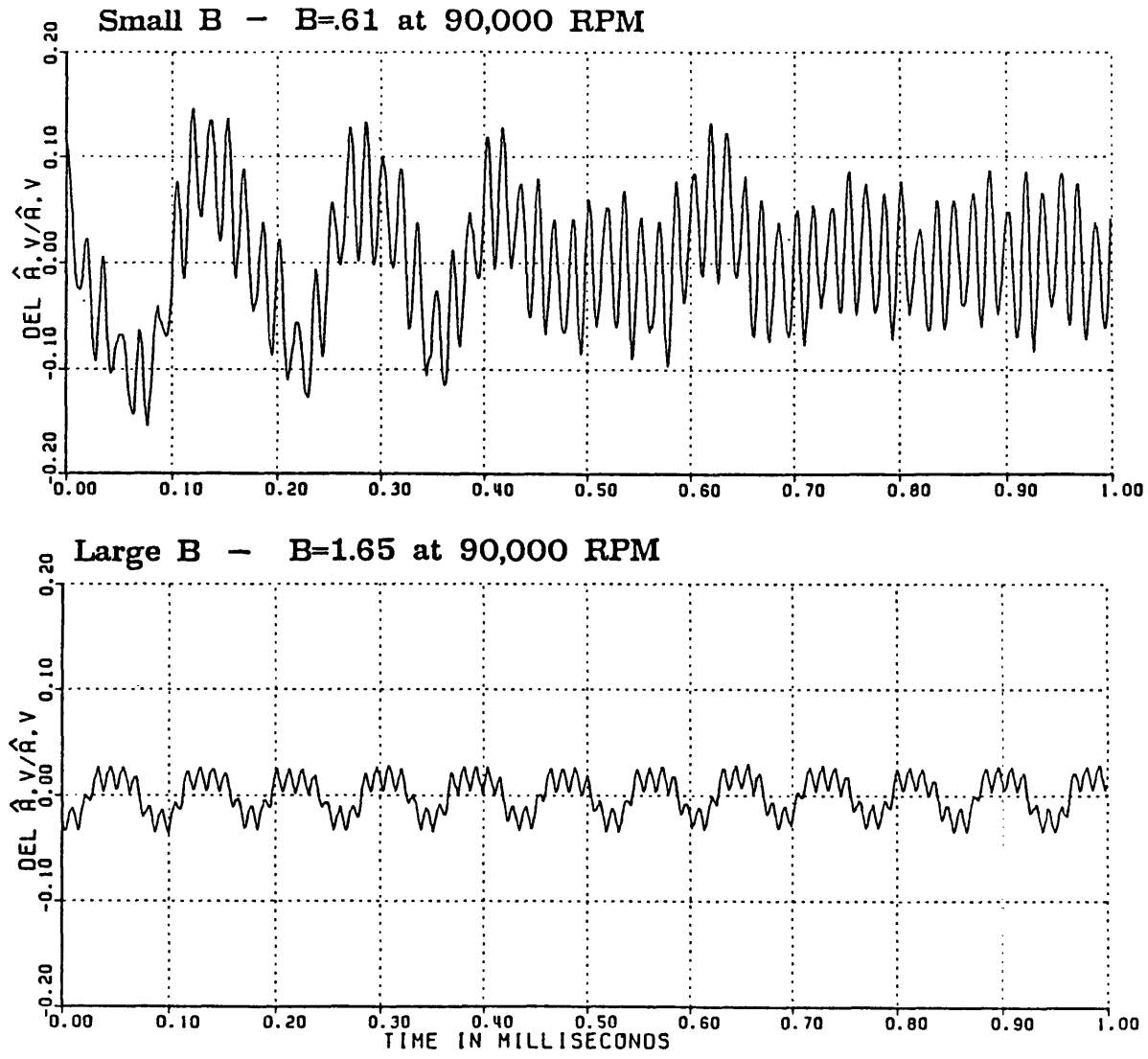

Figure 5.19 B Dependence of Controller Instability Frequency Controlled Operating Points for Case I (Small B) and Case II (Large B)

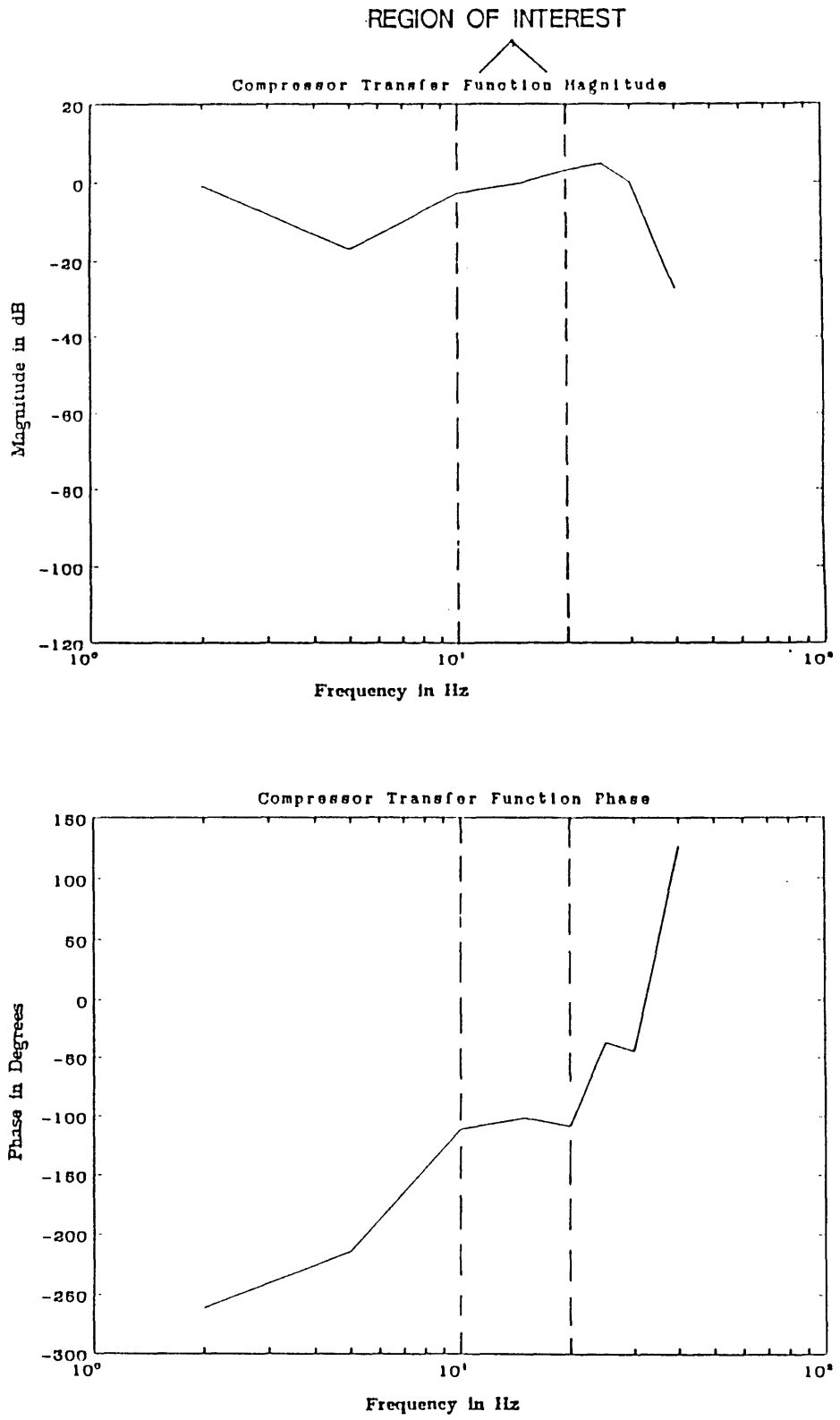

Figure 5.20 Measured Compressor Transfer Function
Input = Pressure Rise, Output = Mass Flow

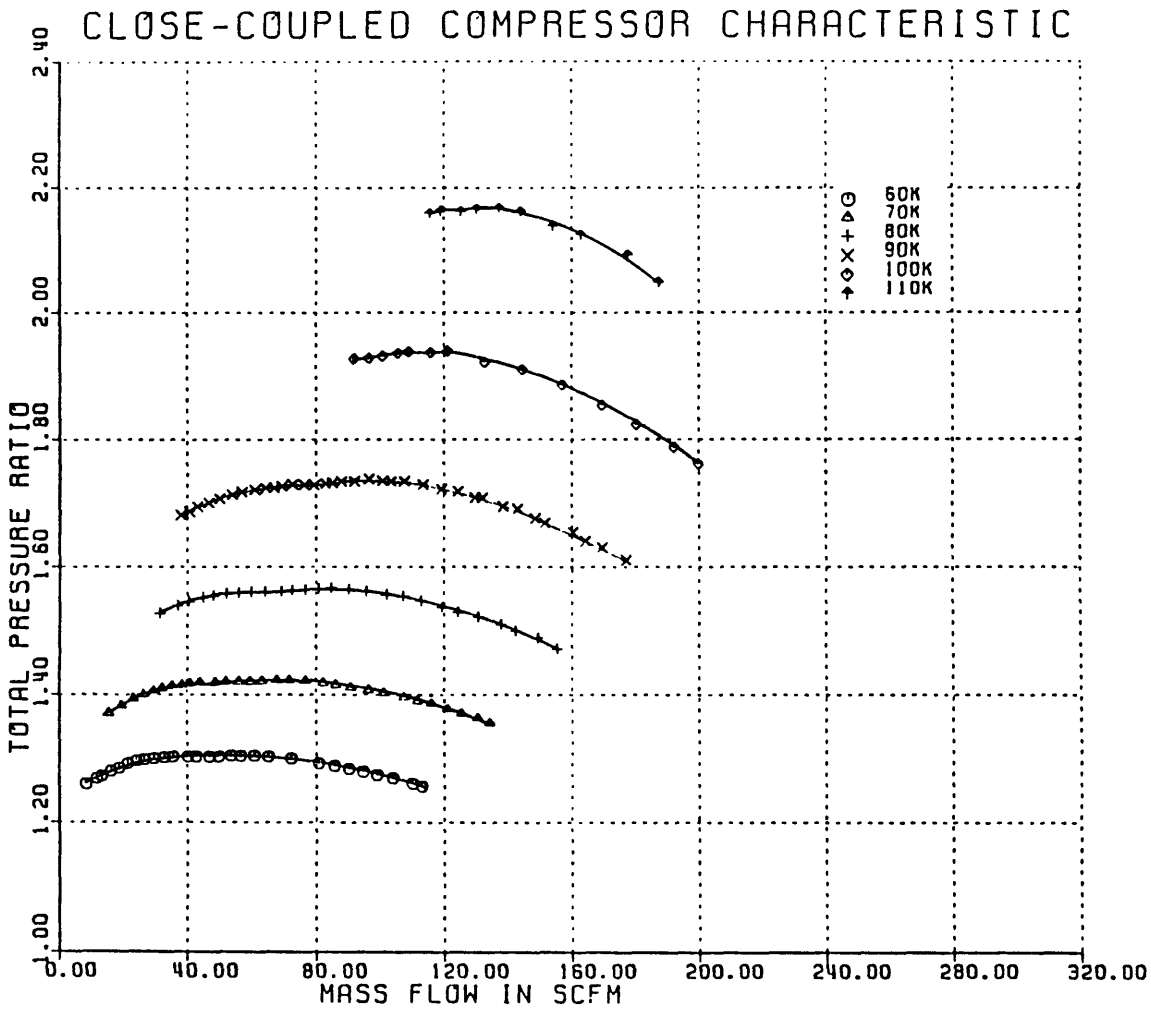

Figure 5.21(a) Measured Compressor Map in Close-Coupled Configuration, Pressure Ratio vs. SCFM

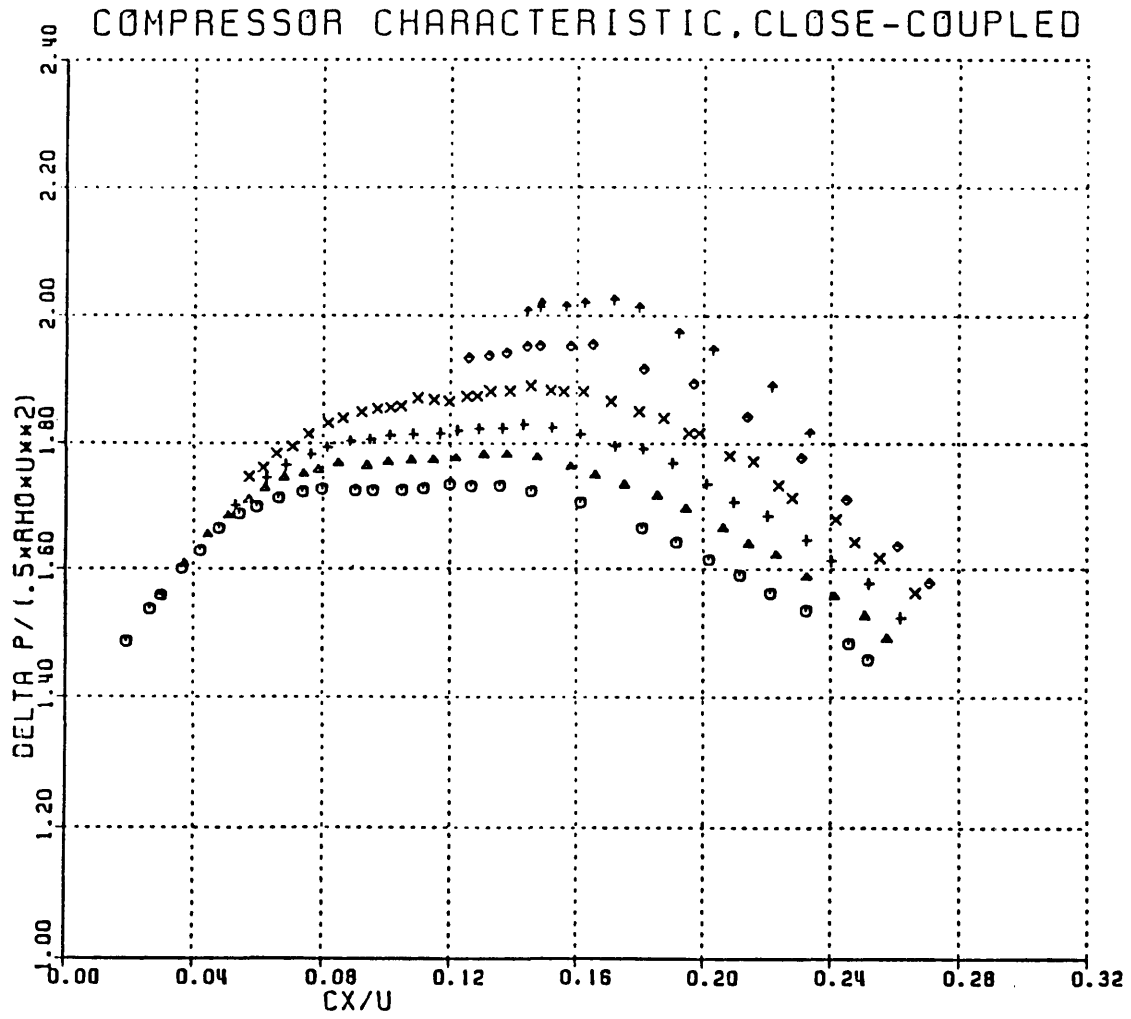

Figure 5.21(b) Measured Compressor Map in Close-Coupled Configuration, ψ vs. ϕ

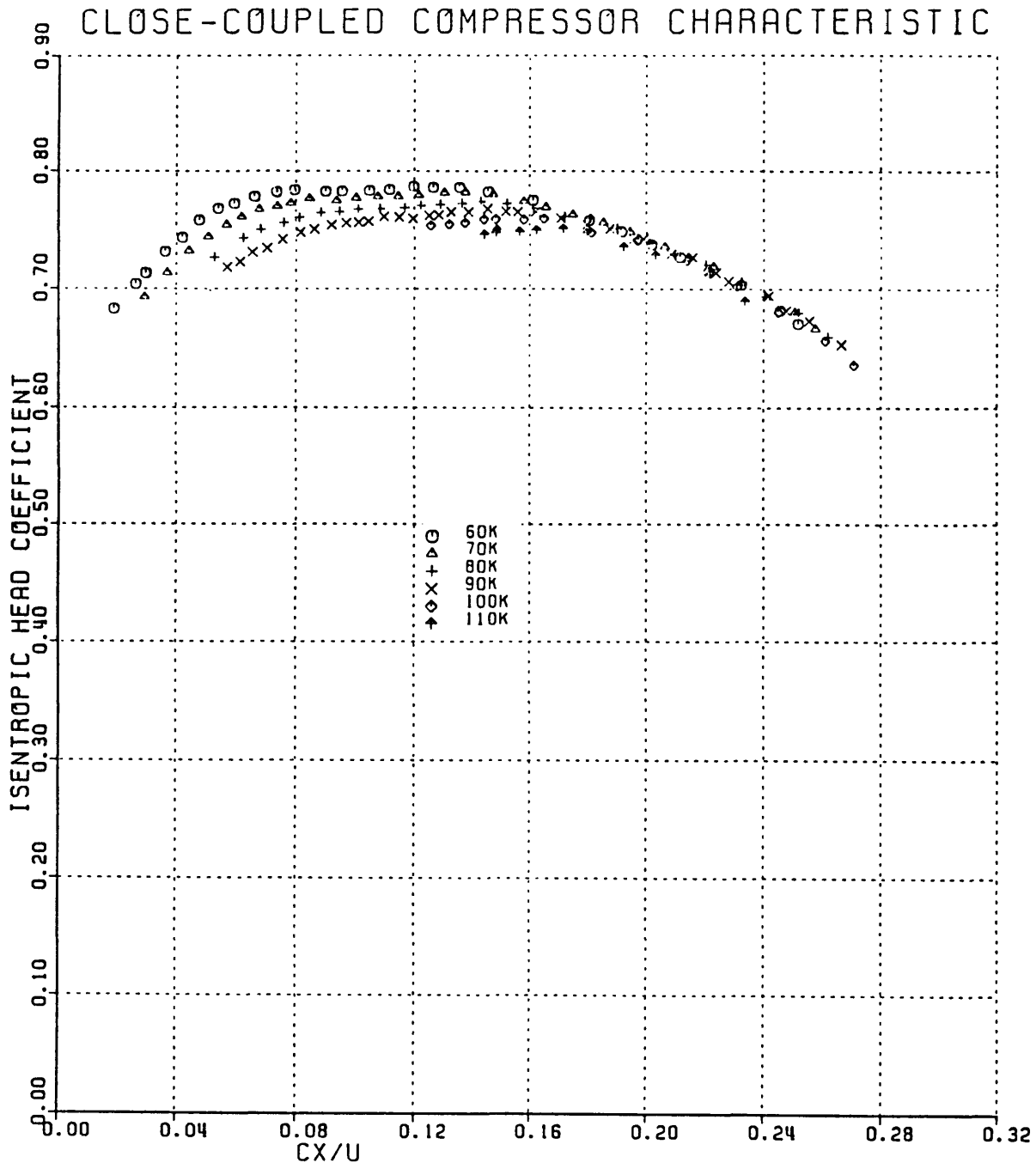

Figure 5.21(c) Measured Compressor Map in Close-Coupled Configuration, Isentropic Head Coefficient vs. ϕ

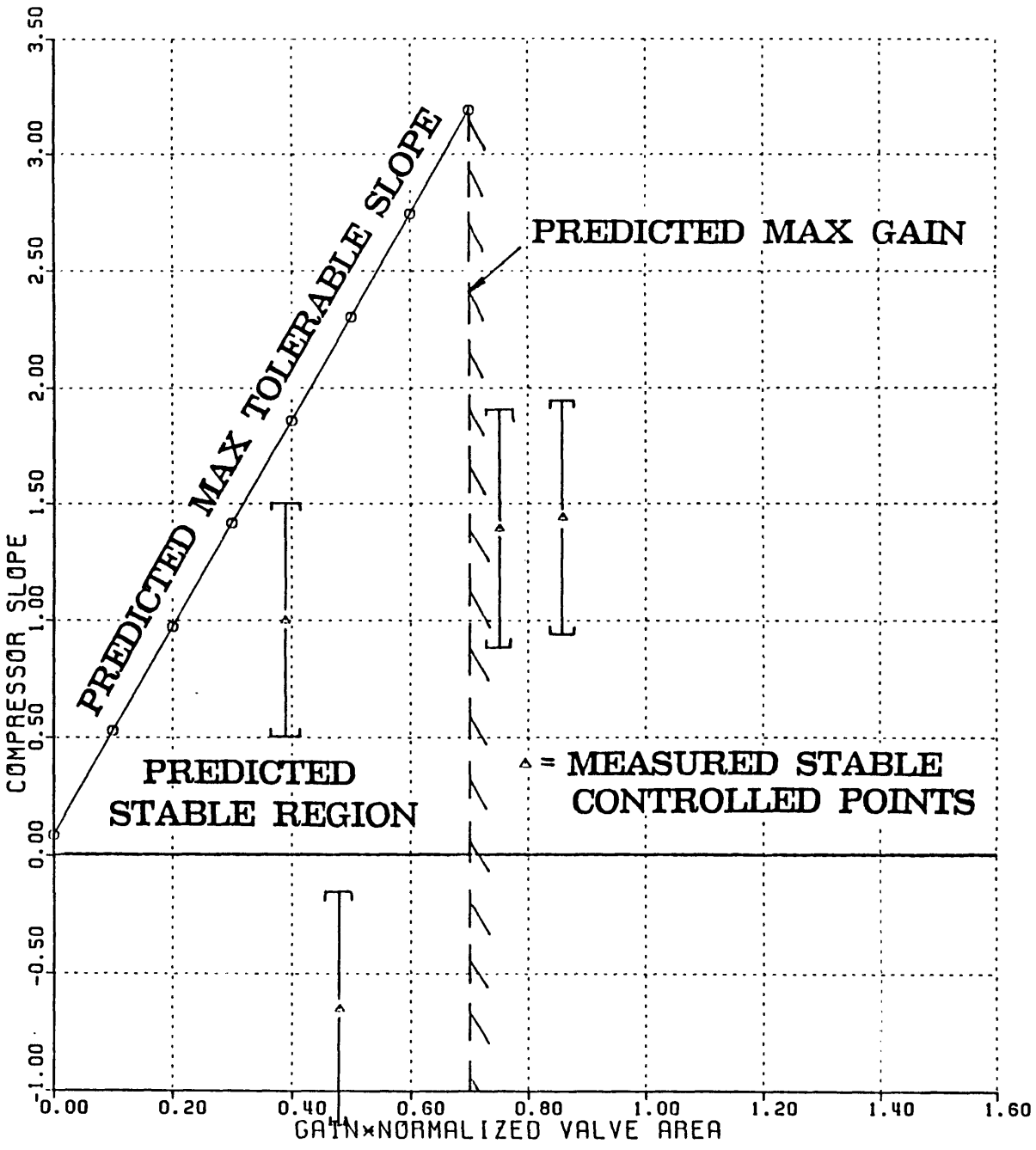

Figure 5.22 Comparison of Measured Controller Gain to Predicted Gain
B = .61, N_{corr} = 90,000 RPM, Gain = Magnitude of z_A

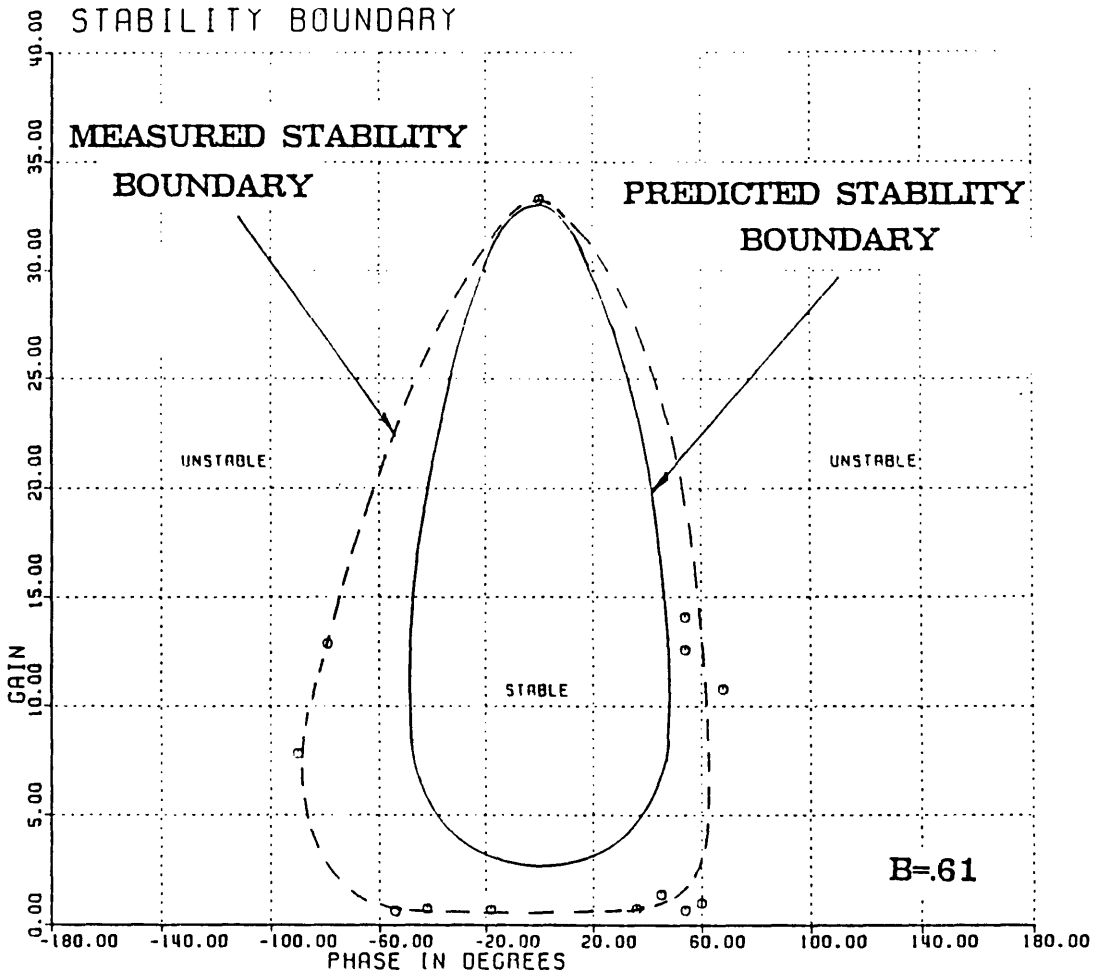

Figure 5.23 Comparison of Measured Stability Boundary to Predicted Stability Boundary
B = .61, N_{corr} = 90,000 RPM, ϕ = .12, ψ = 1.87, Gain = Magnitude of z_A
$\hat{T}_c$ for Theoretical Prediction Set to 1 to Match Measured Gain at Zero Phase

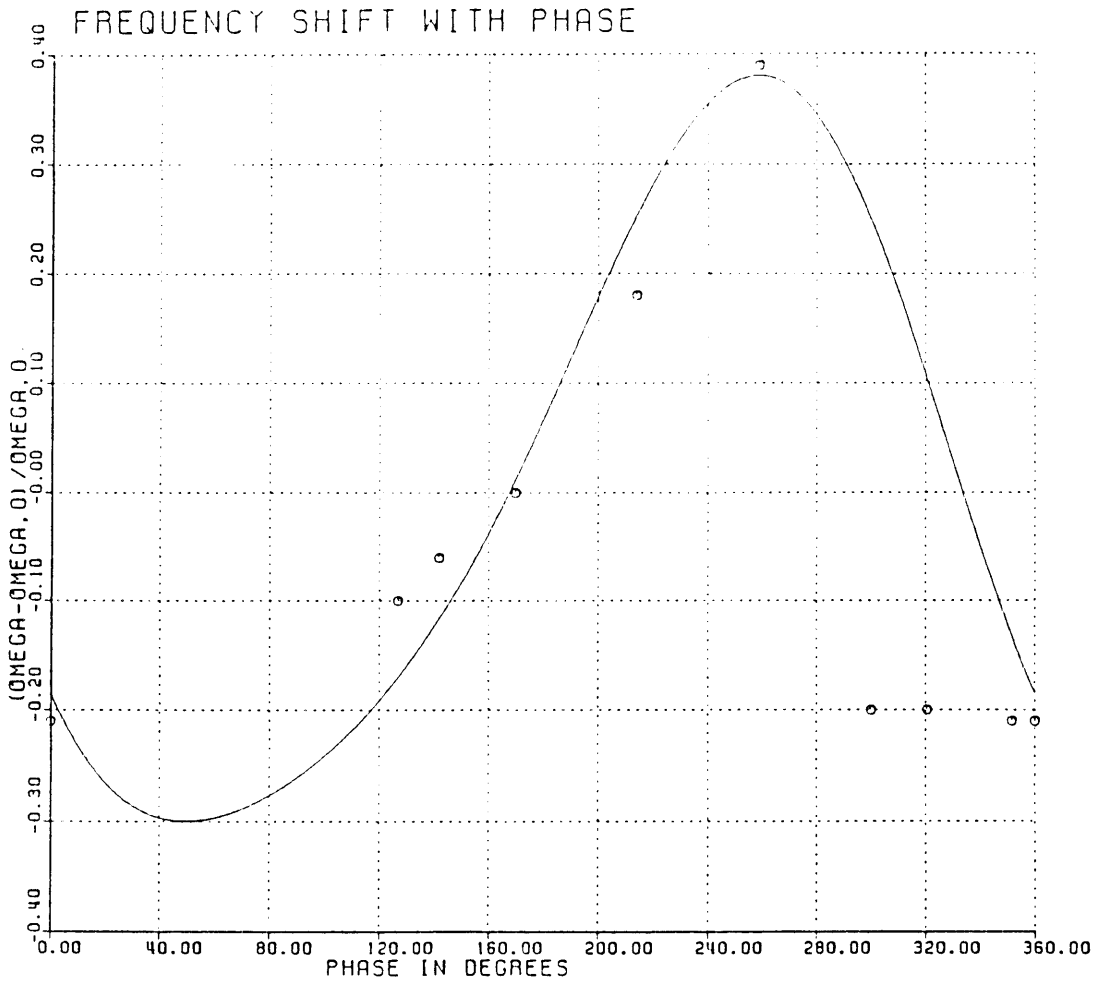

Figure 5.24 Comparison of Measured Resonant Frequency Variation with Controller Phase to Predicted Variation
B=.61, N_{corr} = 90,000 RPM, Cubic Characteristic Assumed for Theory

Appendix A

Derivation of the System Characteristic Equation

Consider the compression system shown below:

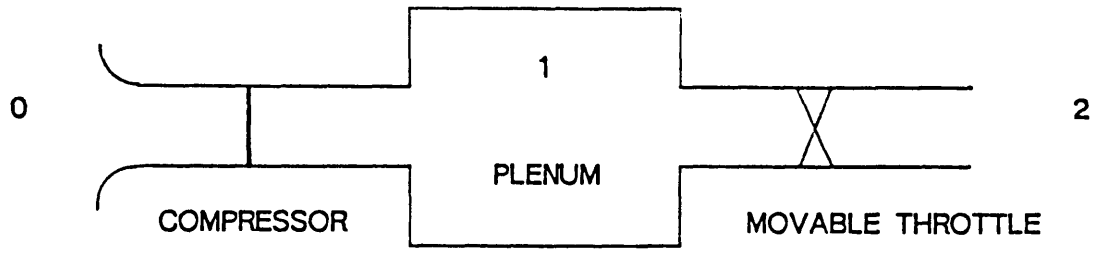

Assuming:

1) Quasi-steady compressor behavior
2) Uniform pressure throughout the plenum
3) Isentropic fluid behavior in the plenum
4) Incompressible flow in the ducts
5) Negligible throttle inertance
6) Quasi-steady flow through the throttle
7) Constant ambient conditions

the integral form of the momentum equation for the compressor duct, assuming one-dimensional flow, is:

$$P_0 - P_1 = \int_0^1 \rho \frac{\partial C_x}{\partial t} dx - \Delta P_{t,c} \qquad (A.1)$$

where: C_x = axial velocity through the compressor duct

$\Delta P_{t,c}$ = total pressure rise across the compressor

An equivalent compressor duct length is defined as:

$$L_c = A_{in} \int_0^1 \frac{dx}{A(x)} \tag{A.2}$$

where A(x) is the duct cross-sectional area and A_{in} is the throughflow area at the compressor inlet face. Substituting Eq. (A.2) into Eq. (A.1) gives:

$$P_0 - P_1 = \left(\frac{L_c}{A_{in}}\right) \rho \frac{\partial C_x}{\partial t} A(x) - \Delta P_{t,c} \tag{A.3}$$

Since:

$$\dot{m}_1 = \rho C_x A(x) \tag{A.4}$$

Eq. (A.3) is rewritten as:

$$P_0 - P_1 = \frac{L_c}{A_{in}} \frac{d\dot{m}_1}{dt} - \Delta P_{t,c} \tag{A.5}$$

In the exit duct, the inertance of the throttle is neglected, so that the momentum equation gives simply:

$$P_1 - P_2 = \Delta P_{t,v} \tag{A.6}$$

where $\Delta P_{t,v}$ is the total pressure drop across the valve. Mass conservation in the plenum requires:

$$\dot{m}_1 = \dot{m}_2 - V_p \frac{d\rho_1}{dt} \tag{A.7}$$

where V_p is the plenum volume. Assuming the fluid in the plenum behaves isentropically:

$$\frac{P_1}{\rho_1^{\gamma}} = \text{constant} \tag{A.8}$$

So:

$$\frac{d\rho_1}{dt} = \frac{d\rho_1}{dP_1}\frac{dP_1}{dt} \tag{A.9}$$

$$\frac{d\rho_1}{dt} = \frac{\rho_1}{\gamma P_1}\frac{dP_1}{dt} \tag{A.10}$$

Using the Perfect Gas Law:

$$\frac{d\rho_1}{dt} = \frac{1}{\gamma R T_1}\frac{dP_1}{dt} \tag{A.11}$$

With the definition of the speed of sound in the plenum:

$$a_1 = \sqrt{\gamma R T_1} \tag{A.12}$$

Eq. (A.11) becomes:

$$\frac{d\rho_1}{dt} = \frac{1}{a^2}\frac{dP_1}{dt} \tag{A.13}$$

Substituting Eq. (A.13) into Eq. (A.7) gives:

$$\dot{m}_1 = \dot{m}_2 + \frac{V_p}{a_1^2}\frac{dP_1}{dt} \tag{A.14}$$

Eqs. (A.5), (A.6), and (A.14) completely describe the fluid mechanics in the compression system. These equations are linearized for small perturbations around a mean operating point. The variables in the equations become:

$$\dot{m}_1 = \overline{\dot{m}_1} + \delta\dot{m}_1 \tag{A.15}$$

$$\dot{m}_2 = \overline{\dot{m}_2} + \delta\dot{m}_2 \tag{A.16}$$

$$P_1 = \overline{P_1} + \delta P_1 \tag{A.17}$$

$$\Delta P_{t,c} = \overline{\Delta P_{t,c}} + \frac{d\overline{\Delta P_{t,c}}}{d\dot{m}_1}\,\delta\dot{m}_1 \tag{A.18}$$

$$\Delta P_{t,v} = \overline{\Delta P_{t,v}} + \frac{\partial\overline{\Delta P_{t,v}}}{\partial\dot{m}_2}\,\delta\dot{m}_2 + \frac{\partial\overline{\Delta P_{t,v}}}{\partial A_v}\,\delta A_v \tag{A.19}$$

where overbars designate mean flow properties. A_v is the throttle valve area. Assuming the inlet and exit are both at ambient conditions, $P_0 = P_2 =$ constant. The total pressure slopes are written more compactly as:

$$T_c = \frac{d\overline{\Delta P_{t,c}}}{d\dot{m}_1} \tag{A.20}$$

$$T_v = \frac{\partial\overline{\Delta P_{t,v}}}{\partial\dot{m}_2} \tag{A.21}$$

$$C_v = \frac{\partial\overline{\Delta P_{t,v}}}{\partial A_v} \tag{A.22}$$

Substituting Eqs. (A.15) to (A.17) and (A.20) to (A.22) into Eqs. (A.5),(A.6), and (A.14), the mean values are subtracted and the equations combined to form two coupled perturbation equations:

$$\frac{L_c}{A_{in}} \frac{d\delta\dot{m}_1}{dt} = T_c \delta\dot{m}_1 - \delta P_1 \tag{A.23}$$

$$\frac{V_p}{a_1^2} \frac{d\delta P_1}{dt} = \delta\dot{m}_1 - \frac{1}{T_v} \delta P_1 + \frac{C_v}{T_v} \delta A_v \tag{A.24}$$

The variables in Eqs. (A.23) and (A.24) are nondimensionalized by:

$$\delta\psi = \frac{\delta P_1}{\frac{1}{2}\rho_0 U^2} \tag{A.25}$$

$$\delta\phi = \frac{\delta\dot{m}_1}{\rho_0 U A_{in}} \tag{A.26}$$

$$\hat{t} = \omega t \tag{A.27}$$

$$\hat{A}_v = \frac{A_v}{A_{in}} \tag{A.28}$$

$$\hat{T}_c = T_c\left(\frac{2A_{in}}{U}\right) \tag{A.29}$$

$$\hat{T}_v = T_v\left(\frac{2A_{in}}{U}\right) \tag{A.30}$$

$$\hat{C}_v = C_v\left(\frac{2A_{in}}{\rho_0 U^2}\right) \tag{A.31}$$

With the definition of the Helmholtz frequency, ω:

$$\omega = a_1\sqrt{\frac{A_{in}}{V_p L_c}} \tag{A.32}$$

and defining a stability parameter, B, as:

$$B = \frac{U}{2\omega L_c} = \frac{U}{2a_1}\sqrt{\frac{V_p}{L_c A_{in}}} \tag{A.33}$$

Eqs. (A.23) and (A.24) become:

$$\frac{d\delta\phi}{d\hat{t}} = \frac{\hat{T}_c B}{2}\delta\phi - \frac{B}{2}\delta\psi \tag{A.34}$$

$$\frac{d\delta\psi}{d\hat{t}} = \frac{1}{2B}\delta\phi - \frac{1}{2B\,\hat{T}_v}\delta\psi + \frac{\hat{C}_v}{2B\,\hat{T}_v}\delta\hat{A}_v \tag{A.35}$$

The control law is selected as simple proportional feedback:

$$\frac{\delta\hat{A}_v}{\hat{A}_v} = z_A\,\delta\psi \tag{A.36}$$

where the constant z_A is complex. Inserting Eq. (A.36) into Eq. (A.35), the two nondimensional perturbation equations for the controlled system are:

$$\frac{d\delta\phi}{d\hat{t}} = \frac{\hat{T}_c B}{2}\,\delta\phi - \frac{B}{2}\,\delta\psi \tag{A.37}$$

$$\frac{d\delta\psi}{d\hat{t}} = \frac{1}{2B}\,\delta\phi - \frac{1}{2B}\left(\frac{1 - \hat{C}_v \hat{A}_v z_A}{\hat{T}_v}\right)\delta\psi \tag{A.38}$$

Eqs. (A.37) and (A.38) are represented in matrix form as:

$$\begin{bmatrix} \delta\dot{\phi} \\ \delta\dot{\psi} \end{bmatrix} = \begin{bmatrix} \frac{\hat{T}_c B}{2} & \frac{-B}{2} \\ \frac{1}{2B} & \frac{-1}{2B}\left(\frac{1 - \hat{C}_v \hat{A}_v z_A}{\hat{T}_v}\right) \end{bmatrix} \begin{bmatrix} \delta\phi \\ \delta\psi \end{bmatrix} \tag{A.39}$$

where [A] is the system matrix. Setting the determinant of [A-sI] equal to zero produces the characteristic equation for the controlled compression system:

$$s^2 - \left[\frac{\hat{T}_c B}{2} - \frac{1}{2B}\left(\frac{1 - \hat{C}_v \hat{A}_v z_A}{\hat{T}_v}\right)\right] s - \frac{\hat{T}_c}{4}\left(\frac{1 - \hat{C}_v \hat{A}_v z_A}{\hat{T}_v}\right) + 1 = 0 \tag{A.40}$$

Appendix B

Circuit Diagrams for Controller Components

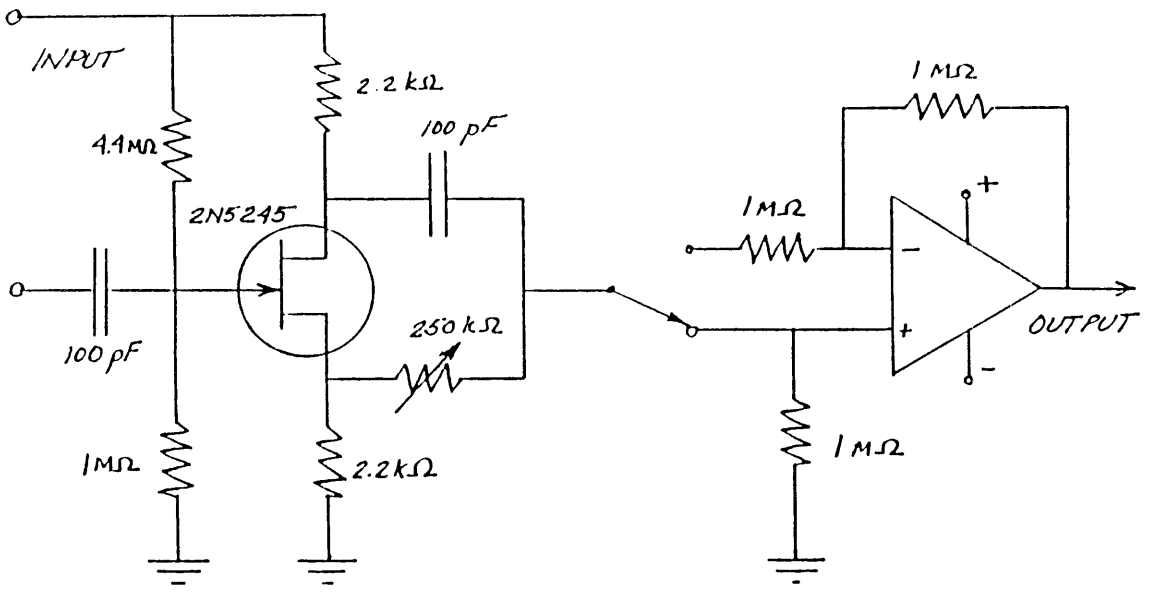

Figure B.2 Pre-Amplifier Circuit [13]

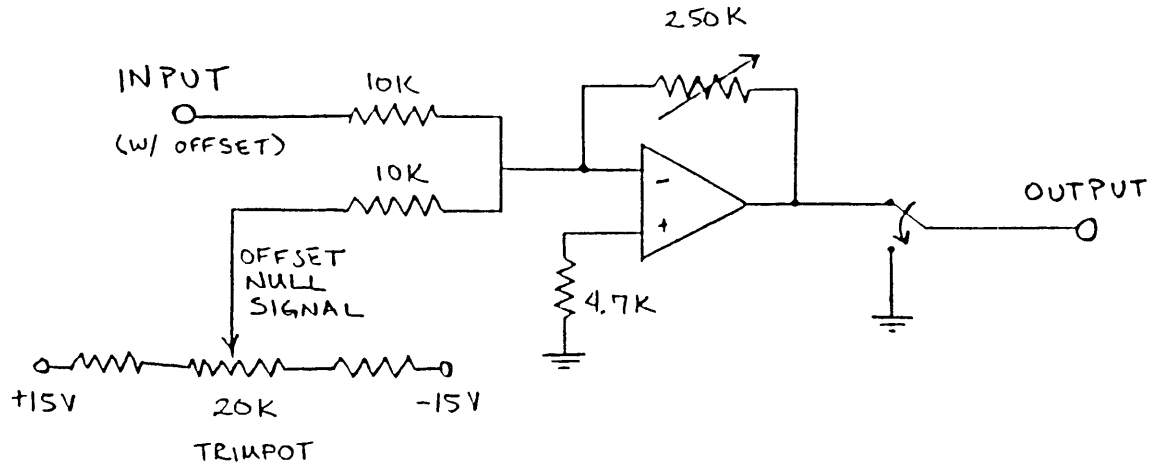

Figure B.1 Phase Shifter Circuit [8]

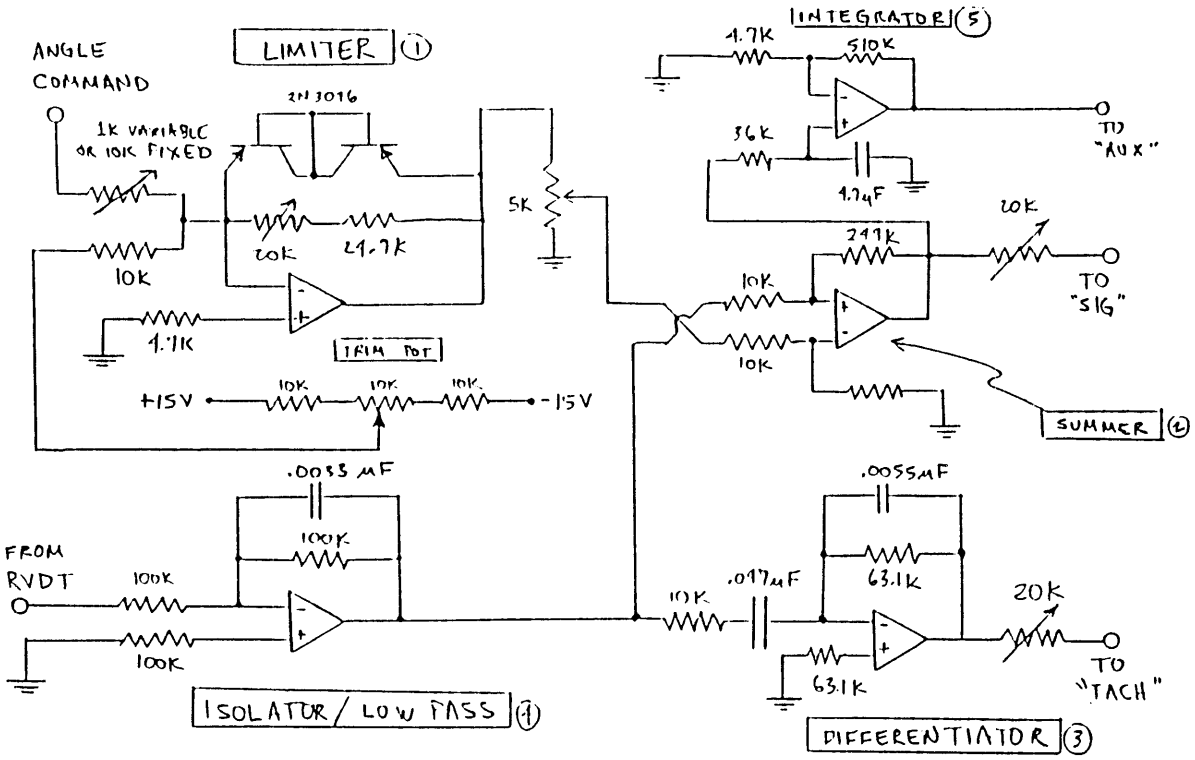

Figure B.3 Motor Controller Circuit [13]

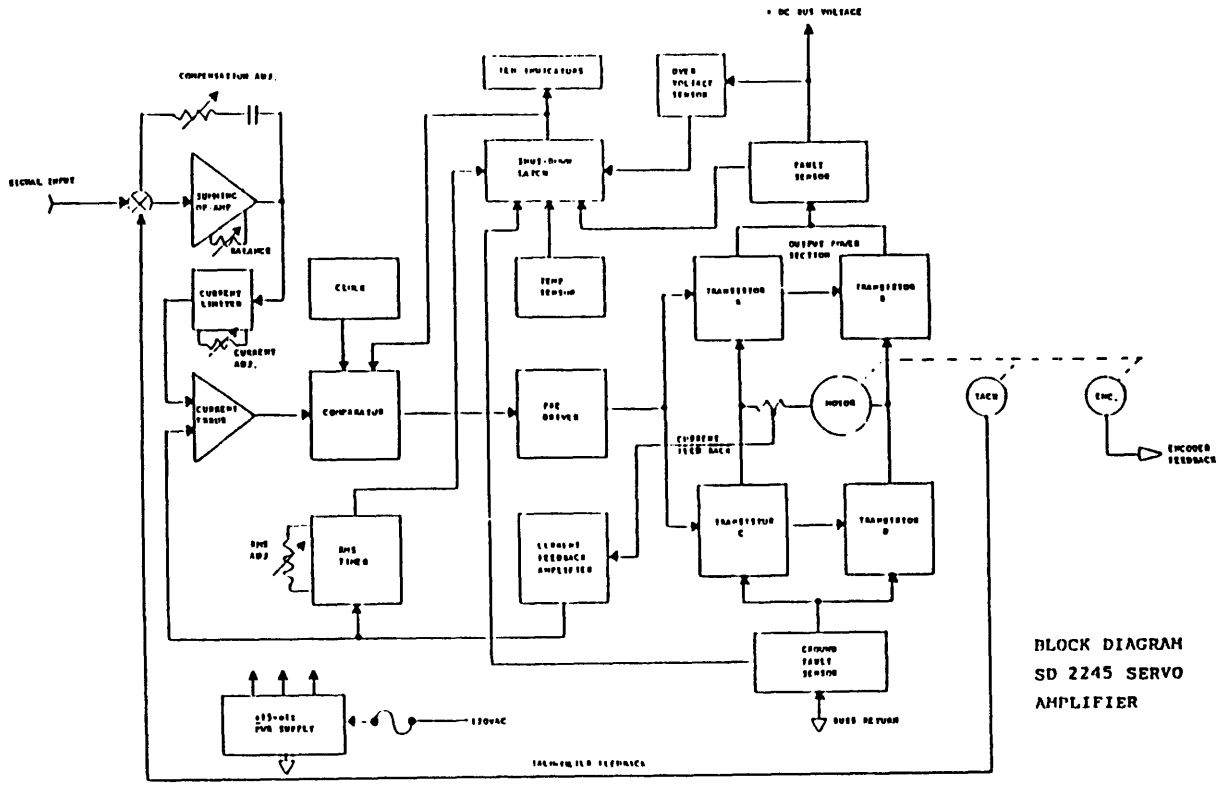

Figure B.4 Amplifier Circuit Functional Diagram, Servodynamics Corporation

Appendix C

Derivation of Compressor Duct Effective Length

The equivalent compressor duct length, L_c, has been defined as:

$$L_c = A_{in} \int_0^1 \frac{dx}{A(x)} \tag{C.1}$$

where A_{in} is the annular impeller area and A(x) is the duct cross-sectional area. The duct comprises three parts:

1) Inlet Duct
2) Compressor
3) Compressor Exit Duct

1) The inlet duct inner diameter is 5.2 cm (2.0 inches). The length of the inlet was varied for different parametric studies. The length of the short inlet pipe is 22.6 cm (8.9 inches), while the long inlet pipe is 2.05 m (81 inches). Neglecting the curvature of the bellmouth as relatively small, the contribution to the effective length from the inlet becomes:

$$\left(\frac{L_c}{A_{in}}\right)_{inlet} = \frac{\text{inlet pipe length}}{\text{inlet pipe cross-sectional area}} \tag{C.2}$$

Values for the two inlet lengths are:

$$\left(\frac{L_c}{A_{in}}\right)_{short\ inlet} = \frac{.226\ m}{2.11 \times 10^{-3}\ m^2} = 107.2\ m^{-1}$$

$$\left(\frac{L_c}{A_{in}}\right)_{long\ inlet} = \frac{2.054\ m}{2.11 \times 10^{-3}\ m^2} = 973.2\ m^{-1}$$

2) The derivation of the effective length through the compressor is given by [21] for a geometrically similar turbocharger, with all dimensions given in mm:

Compressor This can be subdivided into three sections:

(a) Diffusing passage before scroll

(b) Scroll

(c) Diffusing passage after scroll

(a) Diffusing passage before scroll

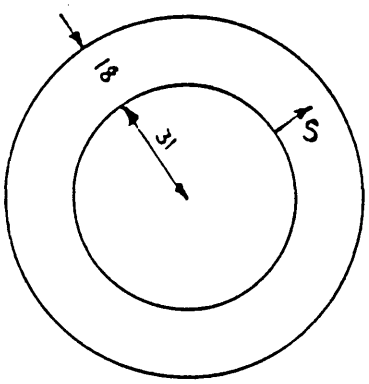

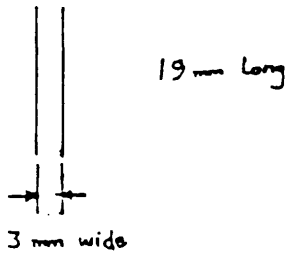

$$A = 2\pi \times 3 \times (31 + s)$$

$$\frac{L}{A} = \int_0^{18} \frac{ds}{6\pi\,(31 + s)} \qquad \text{(C.3)}$$

$$\left(\frac{L}{A}\right)_{2a} = (1/6\pi)\ln(49/31) = \underline{0.024}$$

(b) Scroll

Assume uniform addition of fluid with angle around scroll so that mass flow Q at angle θ is given by $Q = \frac{\theta}{\theta_T} Q_T$

where the subscript T denotes total values.

Depending on the assumptions made it is possible to demonstrate that either of the following definitions of L/A is plausible:

$$\frac{L}{A} = \int \left(\frac{\theta}{\theta_T}\right)^2 \frac{ds}{A} \qquad \text{(C.4)}$$

or

$$\frac{L}{A} = \int \left(\frac{\theta}{\theta_T}\right) \frac{ds}{A} \qquad \text{(C.5)}$$

Neither is more 'correct' than the other as there is no absolute answer, so it was decided to calculate the value both ways and use the mean of these. Note the existence of a region of radial flow near the inner radius mixing with the flow which is in a direction mainly along the passage.

(i) Assuming $\frac{L}{A} = \int \left(\frac{\theta}{\theta_T}\right)^2 \frac{ds}{A}$

Mean radius is constant at 51mm

$\therefore ds = 51\, d\theta$

Width of the passage is given by

$D = 13 + \frac{\theta}{\theta_T} (32 - 13)$

Hence $\frac{L}{A} = c \int_0^{\theta_T} \frac{\theta^2 \cdot d\theta}{(K + \theta)^2}$ (C.6)

where $c = 4 \times 51/(\pi \times 19^2)$

$\theta_T = 312 \times \pi/180$

and $K = 13\ \theta_T/19$

giving, after some manipulation:

$$\frac{L}{A} = \theta_T - 2K \ln\left[\frac{K + \theta_T}{K}\right] + \left[\frac{K\theta_T}{K + \theta_T}\right] \qquad \text{(C.7)}$$

Thus $\left(\frac{L}{A}\right) = 0.170$

(ii) Assuming $\frac{L}{A} = \int\left(\frac{\theta}{\theta_T}\right)\frac{ds}{A}$

gives $\frac{L}{A} = c\theta_T \int_0^{\theta_T} \frac{\theta d\theta}{(K + \theta)^2}$ (C.8)

$$= c\theta_T \left\{\ln\frac{K + \theta_T}{K} + \frac{K}{K + \theta_T} - 1\right\} \qquad \text{(C.9)}$$

the constants c, K, θ_T are as in (i) giving $\frac{L}{A} = 0.301$

The mean of these two values for the scroll is

$$\left(\frac{L}{A}\right)_{2b} = \underline{0.235}$$

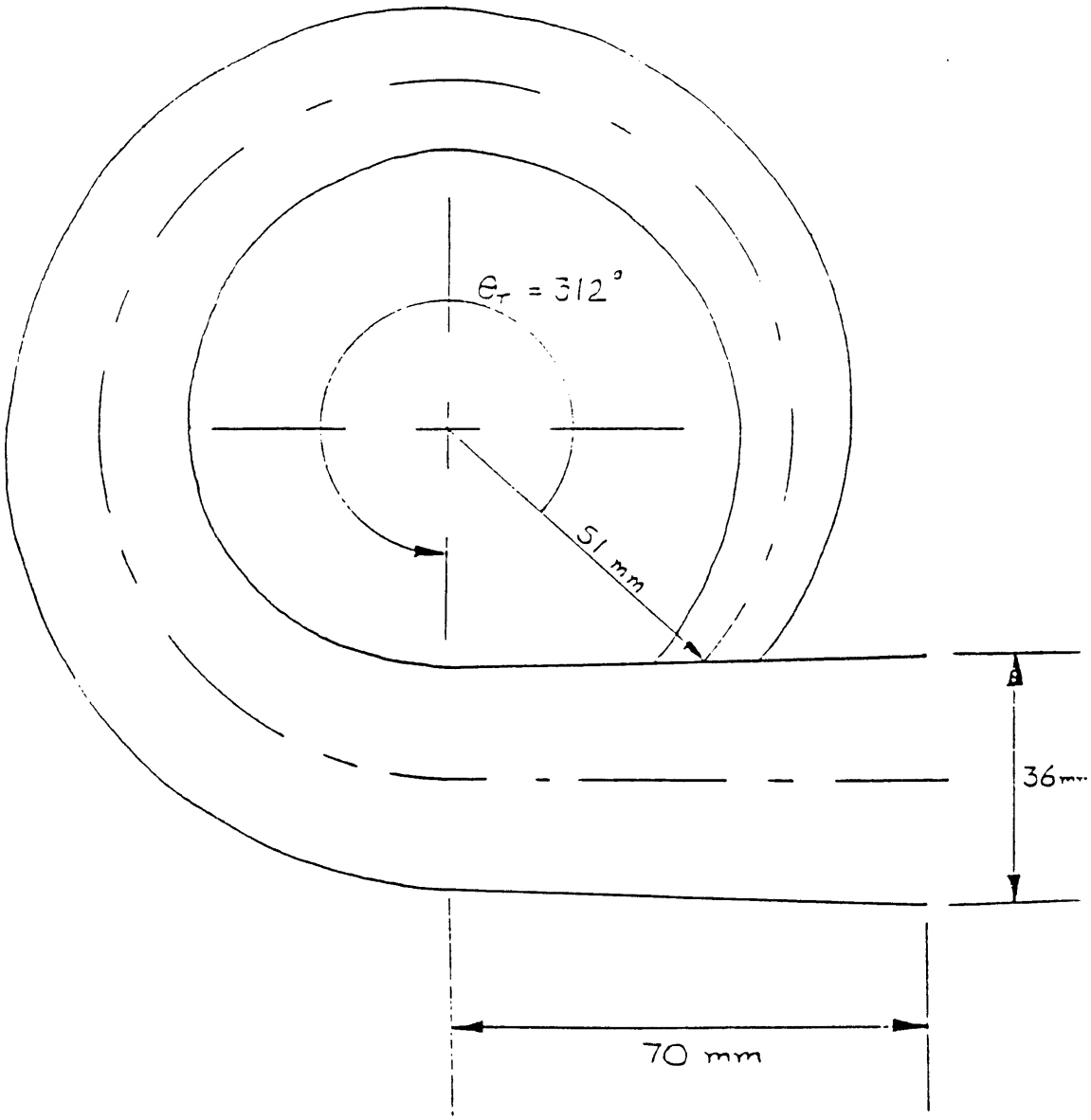

Figure C.1 Compressor Scroll Geometry

(c) Diffusing passage after scroll

(Onto which the outlet pipe fits)

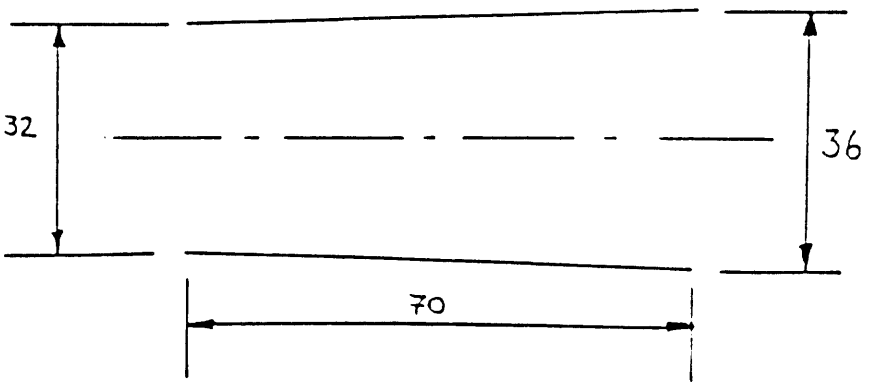

For this $D = 32 + (36 - 32)\frac{s}{70} = 32 + \frac{2s}{35}$

$$\Rightarrow \frac{L}{A} = \int_0^{70} \frac{4\,ds}{\pi(32 + 2s/35)^2} \qquad \text{(C.10)}$$

$$= -35^2/\pi \left[\frac{1}{560 + s} \right]_0^{70}$$

$$\left(\frac{L}{A} \right)_{2c} = \underline{0.077}$$

So the total contribution for the compressor is

$$\left(\frac{L}{A} \right)_2 = 0.024 + 0.235 + 0.077 = \underline{0.336}$$

Thus the total contribution of the compressor is:

$$\left(\frac{L_c}{A_{in}}\right)_{compressor} = 336\ m^{-1}$$

3) The exit duct is composed of a) a coupling between the compressor and the plenum, and b) a pipe extending into the plenum.

a)

$$\left(\frac{L_c}{A_{in}}\right)_{coupling} = \frac{\text{coupling length}}{\text{coupling cross-sectional area}} \qquad (C.11)$$

$$\left(\frac{L_c}{A_{in}}\right)_{coupling} = \frac{2.54\times10^{-2}\ m}{1.83\times10^{-3}\ m^2} = 13.9\ m^{-1}$$

b)

$$\left(\frac{L_c}{A_{in}}\right)_{exit\ pipe} = \frac{\text{exit pipe length}}{\text{exit pipe cross-sectional area}} \qquad (C.12)$$

$$\left(\frac{L_c}{A_{in}}\right)_{exit\ pipe} = \frac{.319\ m}{1.31\times10^{-3}\ m^2} = 243.5\ m^{-1}$$

Thus the total contribution for the exit duct is:

$$\left(\frac{L_c}{A_{in}}\right)_{exit} = \left(\frac{L_c}{A_{in}}\right)_{coupling} + \left(\frac{L_c}{A_{in}}\right)_{exit\ pipe} = 257.4\ m^{-1} \qquad (C.13)$$

The value for the effective length through the entire compressor duct is found from:

$$\frac{L_c}{A_{in}} = \left(\frac{L_c}{A_{in}}\right)_{inlet} + \left(\frac{L_c}{A_{in}}\right)_{compressor} + \left(\frac{L_c}{A_{in}}\right)_{exit} \qquad (C.14)$$

For the short inlet:

$$\frac{L_c}{A_{in}} = 700.6\ m^{-1}$$

With $A_{in} = 1.25 \times 10^{-3}\ m^2$, the effective compressor length is:

$$L_{c,\ short} = .88\ m$$

For the long inlet:

$$\frac{L_c}{A_{in}} = 1567\ m^{-1}$$

So that:

$$L_{c,\ long} = 1.96\ m$$

Appendix D

Uncertainty Analysis for Instantaneous Mass Flow

The uncertainty in taking a discrete approximation to the pressure derivative is not easily calculated, especially since the pressure trace is smoothed before differentiation. For qualitative comparison, though, a sine wave was fit to the plots of ψ vs.time to calculate conservatively what the surge cycles would be assuming purely sinusoidal pressure perturbations. In deep surge, the sine wave fit to the data at point E was:

$$\psi = 1.475 + .482\sin(58.8\ (t+.041))$$

In mild surge at point C, the curve fit was:

$$\psi = 1.83 + .1\sin(80.42\ (t+.025))$$

Figures (D.1) and (D.2) show the instantaneous mass flow calculated both from the actual data and from the sine fit. In mild surge the agreement is quite good, since the actual data is nearly sinusoidal. In deep surge, the mass flow from sine fit differs from that for the actual data by about 10% of the total flow excursion. The difference may be attributed to local deviations in the actual pressure rise from a pure sinusoid. The sine fit, therefore, is overly conservative and the uncertainty is believed to be an order of magnitude lower than the plot shows, or 1%.

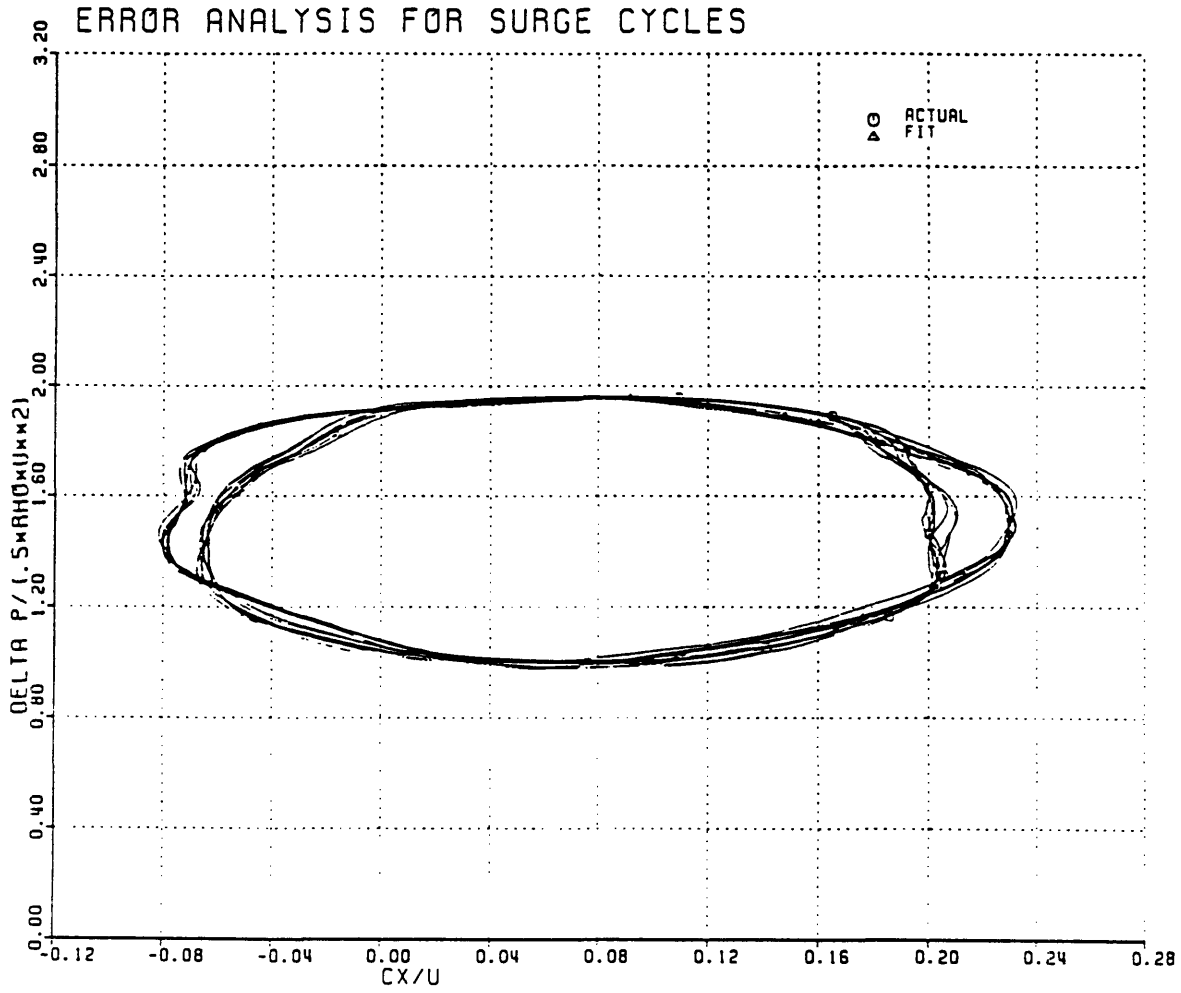

Figure D.1 Comparison of Surge Cycles with Actual Smoothed Data to Sine Fit Deep Surge

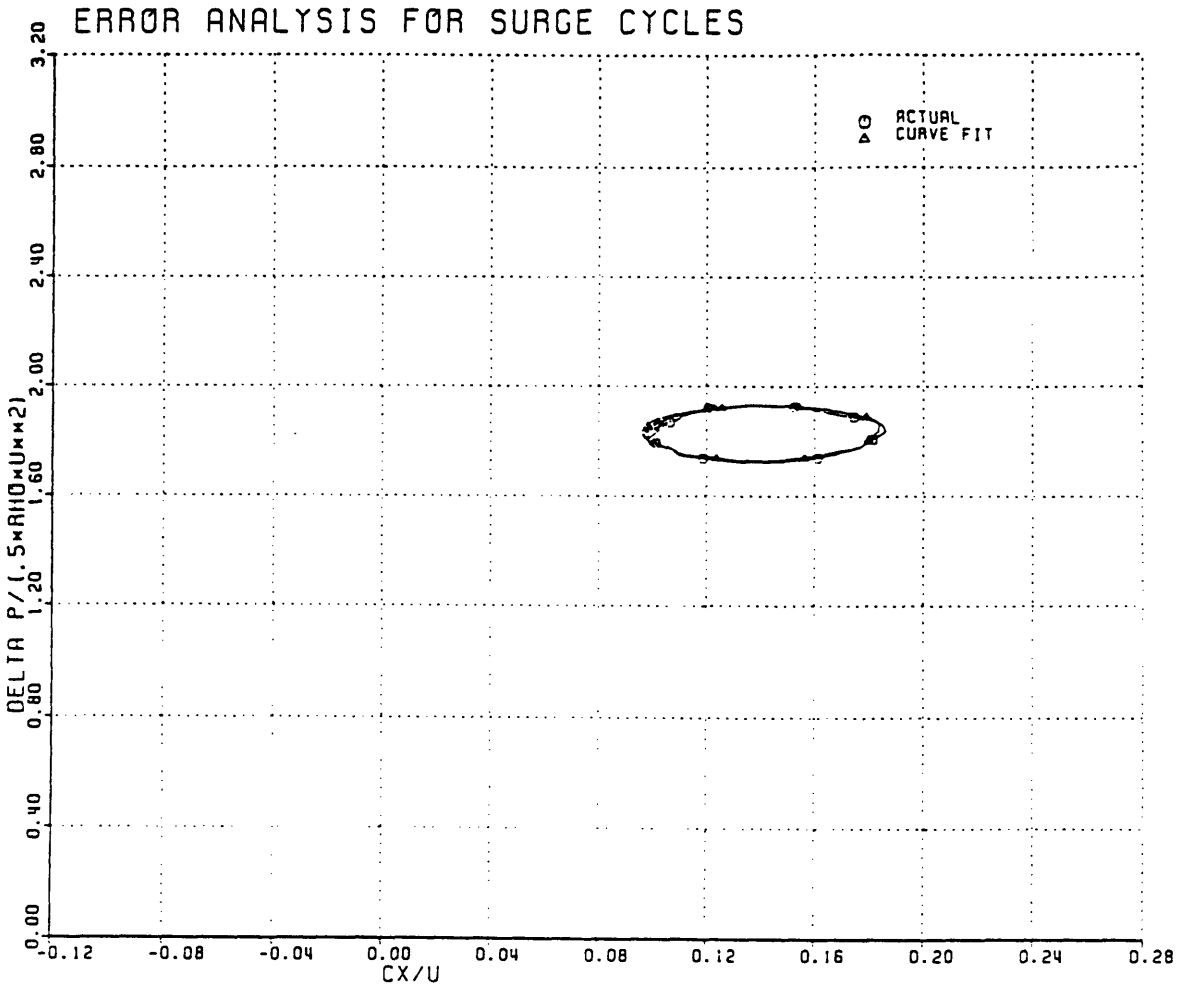

Figure D.2 Comparison of Surge Cycles with Actual Smoothed Data to Sine Fit Mild Surge